AD_____
(Leave blank)

Award Number:
W81XWH-06-1-0389

TITLE:
Contrast Enhancement for Thermal Acoustic Breast Cancer Imaging via Resonant Stimulation

PRINCIPAL INVESTIGATOR:
Jian Li, Ph.D.

CONTRACTING ORGANIZATION:
University of Florida
Gainesville, FL 32603

REPORT DATE:
March 2010

TYPE OF REPORT:
Final

PREPARED FOR: U.S. Army Medical Research and Materiel Command
Fort Detrick, Maryland 21702-5012

DISTRIBUTION STATEMENT: (Check one)

√ Approved for public release; distribution unlimited

□ Distribution limited to U.S. Government agencies only; report contains proprietary information

The views, opinions and/or findings contained in this report are those of the author(s) and should not be construed as an official Department of the Army position, policy or decision unless so designated by other documentation.

REPORT DOCUMENTATION PAGE

Form Approved
OMB No. 0704-0188

Public reporting burden for this collection of information is estimated to average 1 hour per response, including the time for reviewing instructions, searching existing data sources, gathering and maintaining the data needed, and completing and reviewing this collection of information. Send comments regarding this burden estimate or any other aspect of this collection of information, including suggestions for reducing this burden to Department of Defense, Washington Headquarters Services, Directorate for Information Operations and Reports (0704-0188), 1215 Jefferson Davis Highway, Suite 1204, Arlington, VA 22202-4302. Respondents should be aware that notwithstanding any other provision of law, no person shall be subject to any penalty for failing to comply with a collection of information if it does not display a currently valid OMB control number. **PLEASE DO NOT RETURN YOUR FORM TO THE ABOVE ADDRESS.**

1. REPORT DATE *(DD-MM-YYYY)*	**2. REPORT TYPE**	**3. DATES COVERED** *(From - To)*
26-03-2010	Final	27/02/2006 – 26/02/2010

4. TITLE AND SUBTITLE

Contrast Enhancement for Thermal Acoustic Breast Cancer Imaging via Resonant Stimulation

5a. CONTRACT NUMBER

5b. GRANT NUMBER
W81XWH-06-1-0389

5c. PROGRAM ELEMENT NUMBER

6. AUTHOR(S)
Jian Li

Email: li@dsp.ufl.edu

5d. PROJECT NUMBER

5e. TASK NUMBER

5f. WORK UNIT NUMBER

7. PERFORMING ORGANIZATION NAME(S) AND ADDRESS(ES)

University of Florida
Gainesville, FL 32603

8. PERFORMING ORGANIZATION REPORT NUMBER

9. SPONSORING / MONITORING AGENCY NAME(S) AND ADDRESS(ES)
USA MED RESEARCH ACQ ACTIVITY
820 CHANDLER ST
FORT DETRICK MD 21702-5014

10. SPONSOR/MONITOR'S ACRONYM(S)

11. SPONSOR/MONITOR'S REPORT NUMBER(S)

12. DISTRIBUTION / AVAILABILITY STATEMENT

Distribution Unlimited

13. SUPPLEMENTARY NOTES

14. ABSTRACT
This research focuses on developing enhanced contrast thermal acoustic imaging (TAI) technology for the detection of breast cancer by combining amplitude-modulated (AM) electromagnetic (EM) field excitation, resonant acoustic scattering, and advanced signal processing techniques. EM-induced TAI combines the merits of both EM stimulation and ultrasound imaging, while overcoming their respective limitations. While EM-induced TAI possesses great promise, the thermal acoustic signals tend to be weak. However, when the tumor is excited into resonance via EM stimulation, the effective acoustic scattering cross-section may increase by a factor in excess of 100 based on predictions for microsphere-based ultrasound contrast agents. Such an increase would truly be revolutionary, making the EM-induced TAI technology a very promising candidate for routine breast cancer screening. The image formation methods in the existing TAI systems are data-independent and have poor resolution and high sidelobe problems. We devise adaptive image formation algorithms to achieve high resolution and excellent interference and noise suppression capability.

15. SUBJECT TERMS
Thermal Acoustic Imaging (TAI), Resonance, Electromagnetic, Adaptive Imaging

16. SECURITY CLASSIFICATION OF:			**17. LIMITATION OF ABSTRACT**	**18. NUMBER OF PAGES**	**19a. NAME OF RESPONSIBLE PERSON**
a. REPORT	**b. ABSTRACT**	**c. THIS PAGE**			Jian Li
			SAR	69	**19b. TELEPHONE NUMBER** *(include area code)* 352-392-2642

Table of Contents

I. Introduction

This research focuses on developing enhanced contrast thermal acoustic imaging (TAI) technology for the detection of breast cancer by combining amplitude-modulated (AM) electromagnetic (EM) field excitation, resonant acoustic scattering, and advanced signal processing techniques. EM-induced TAI combines the merits of both EM stimulation and ultrasound imaging, while overcoming their respective limitations. EM imaging provides excellent contrast between cancerous and normal breast tissue, but the long wavelengths provide poor spatial resolution. Conventional ultrasound imaging possesses very fine millimeter-range spatial resolution but poor soft tissue contrast. While EM-induced TAI possesses great promise, the thermal acoustic signals tend to be weak. However, when the tumor is excited into resonance via EM stimulation, the effective acoustic scattering cross-section may increase by a factor in excess of 100 based on predictions for microsphere-based ultrasound contrast agents. Such an increase would truly be revolutionary, making the EM-induced TAI technology a very promising candidate for routine breast cancer screening. To induce the resonant response from the tumor, we consider various approaches including, for example, AM continuous wave (CW) EM stimulation, where the modulation frequency range contains the predicted resonant frequencies for a distribution of tumor sizes and contrast ratios. The carrier frequency of the EM stimulation can be fixed and chosen for the best penetration and heat absorption. The image formation methods in the existing TAI systems are predominantly data-independent delay-and-sum (with or without weighting) type of approaches. These approaches tend to have poor resolution (relative to the best possible resolution a transducer array can offer) and high sidelobe problems, especially when the transducer array is not composed of uniformly and linearly spaced transducers, which is the case for the existing TAI systems. We devise adaptive image formation algorithms to achieve high resolution and excellent interference and noise suppression capability.

II. Body

II.1 Theory

Previous work in the area of thermo-acoustic imaging all utilized high peak power, short pulse excitation [1-4]. In essence these approaches are time domain based, and capture the electro-acoustic impulse response of the phantom system to short, intense EM illumination with a prescribed (high) energy density. They generally require a prohibitively expensive power amplifier along with broadband microwave components and a high-speed data acquisition system. The present study approaches the problem from the frequency domain, and seeks the same information as the time-domain approaches but with using lower power, narrow band excitation to obtain the steady-state response. It is anticipated that due to the thermo-acoustic resonance of phantom, similar imaging information can be obtained but with a significant reduction in excitation power.

The theoretical analysis that forms the foundation for Thermo-Acoustic Imaging (TAI) is based on Diebold's theory published in 1988 [5]. There he provides the theoretical analysis for pressure wave generation by exciting droplets with a modulated laser pulse. Using Diebold's approach, it can be shown that the steady-state pressure response of the phantom to an AM EM wave will be of the form:

$$p_f = \frac{j\beta\sigma E^2 c_s a}{C_p \hat{r}} \left(\frac{\left(\sin q - q\cos q\right)\frac{1}{q^2}}{\left(1-\frac{\rho_s}{\rho_f}\right)\frac{\sin q}{q} - \cos q + j\frac{\rho_s c_s}{\rho_f c_f}\sin q} \right) e^{-jq\hat{r}} \qquad (1)$$

Where the phantom has the properties:

β = thermal expansion coefficient [1/K]

σ = electrical conductivity [S/m]

C_p = specific heat [J/kg* K]

E = electric field intensity inside the phantom (assumed to be uniform over the volume of the phantom) [V/m]

c_s = speed of sound in phantom [m/s]

c_f = speed of sound in surrounding material [m/s]

ρ_s = density of phantom [kg/m^3]

ρ_f = density of surrounding materials $[kg/m^3]$

a = radius of phantom [m]

Additionally the terms q, $\hat{\tau}$, and $\hat{r}$ are the normalized modulation frequency, normalized retarded time, and normalized position of transducer, respectively, and are defined as:

$$\hat{t} = \frac{c_s}{a} t \qquad \text{dimensionless time}$$

$$\hat{\tau} = \frac{c_s}{a}\left[t - \frac{(r-a)}{c_f} \right] \qquad \text{retarded time}$$

$$q = \frac{\omega a}{c_s} = k_s a \qquad \text{wave vector}$$

$$\hat{r} = \frac{r}{a} \qquad \text{distance from sphere center}$$

From this analysis, we can conclude that the frequency domain response characteristics of the phantom pressure signal are determined primarily by the density ratio and sound speed ratio between phantom and surrounding materials. The amplitude of pressure response primarily relies on the material property of phantom (thermal expansion coefficient, conductivity, specific heat), electric field intensity imposed on phantom, and relative position of transducer.

This analysis constitutes the foundation of our numerical simulation. Until very recently we have not had a high degree of confidence in two critical parameters, namely the density of phantom and the electric field intensity distribution which can be obtained from EM field measurements in the tank. For other material constants, specifically β, σ, C_p, and c_s, we have relied on intelligent estimates and are currently in the process of designing experiments to accurately measure and confirm the values used. Figure 1 shows the expected phantom pressure response as a function of modulation frequency based on the assumed material constants.

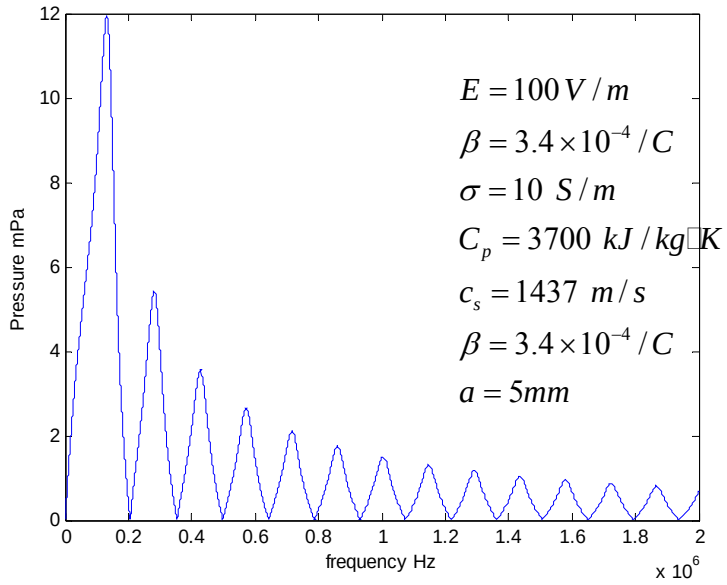

Figure 1: Phantom pressure response as a function of modulation frequency.

Note that the lar gest r esonant pea ks o ccur at frequencies which are outside the bandwidth of the transducer used (center frequency 1MHz, frequency band 0.6 MHz, Panametrics NDT , Model: V303). Hence, in addition to better determ ining the material properties of the phantom , a smaller phantom with hi gher resonant frequencies is currently being designed and fabricated.

Although Diebold's analysis was carried out in frequency dom ain, the experim ents were com pleted using very short laser pul ses that are well-approxim ated as a Dirac delta function. Consequently the sinusoidal steady-state analysis approach followed in the present research ef fort para lleled th e D iebold solu tion. There is, how ever, a significant difference in the two approaches. It was pointed out by Lihong V. Wang in 2000 [6] that if the therm al confinement condition does not apply, the heat conduction effects should be taken into consideration in calculating the pre ssure wave generated by electrom agnetic illum ination. In our case, a Continuous W ave (CW) m odulated microwave source was used to heat the pha ntom and was applied over a m uch longer time scale as com pared with im pulsive excitation. Conseque ntly heat conduction effects must necessarily be included in the analysis.

A sim ple num erical simulation demonstrat es the ef fects due to heat conduction between phantom and the surround ing water. Consider the simple m odel illustrated in Figure 2.

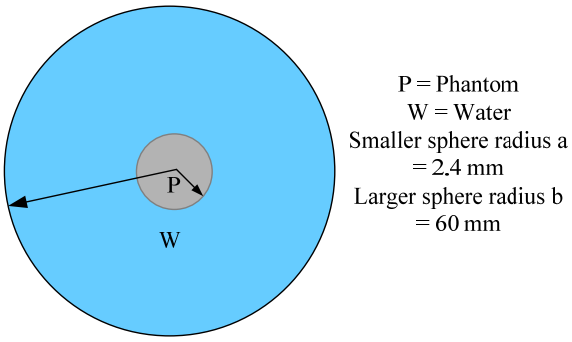

Figure 2: Model of the phantom and the surrounding water.

The phantom volume is heated by heating function $G(t, r)$, which is uniform over the volume of the phantom and results from the electromagnetic illumination. The boundary condition between phantom and water is that the temperature and heat flux in phantom and the water be continuous at the phantom-water interface. The water volume is assumed to be very large hence the outside boundary of water (the water-air interface) is assumed to be perfectly insulated. The governing equations are:

$$
\begin{aligned}
&\alpha_P \frac{1}{r^2}\frac{\partial}{\partial r}\left(r^2 \frac{\partial T_P(r,t)}{\partial r}\right) + \frac{\alpha_P}{k_P} g_P(r,t) = \frac{\partial T_P(r,t)}{\partial t} \qquad 0 < r < a \\
&\alpha_W \frac{1}{r^2}\frac{\partial}{\partial r}\left(r^2 \frac{\partial T_W(r,t)}{\partial r}\right) = \frac{\partial T_W(r,t)}{\partial t} \qquad a < r < b \\
&T_P(0,t) = \textit{finite} \\
&T_P(a,t) = T_W(a,t) \\
&k_P \frac{\partial T_P(r,t)}{\partial r}\Big|_{r=a} = k_W \frac{\partial T_W(r,t)}{\partial r}\Big|_{r=a} \\
&k_W \frac{\partial T_W(r,t)}{\partial r}\Big|_{r=b} = 0
\end{aligned}
\qquad (2)
$$

In Equation (2), α_P, k_P are thermal characteristics of phantom, α_W, k_W are thermal characteristics of water, T_P is temperature distribution in phantom, T_W is temperature distribution in water, and $g_P(r,t)$ is the heating function resulting from the electromagnetic illumination. In order to solve these equations, the appropriate Green's function has been found and utilized. The solution is in the form of series expansion and is given by (note that 500 terms are used in the expansion):

$$T_P(r,t)=\frac{\alpha_P}{k_P}\int_{\tau=0}^{t}d\tau[\int_{r'=0}^{a}(r')^2 G_{PP}(r,t\mid r',\tau)A(1+\cos 2\omega_m\tau)dr']$$
$$=\sum_{n=1}^{500}\left\{A\left[\frac{1}{\beta_n{}^2}(1-\exp(-\beta_n{}^2 t))+\frac{1}{\beta_n{}^4+4\omega_m{}^2}(\beta_n{}^2\cos 2\omega_m t+2\omega_m\sin 2\omega_m t-\beta_n{}^2\exp(-\beta_n{}^2 t))\right]\times\right. \tag{3}$$
$$\left.\frac{1}{N_n}\frac{1}{\sqrt{r}}J_{1/2}(\frac{\beta_n}{\sqrt{\alpha_P}}r)\frac{\sqrt{\alpha_P}}{\beta_n}a^{3/2}J_{3/2}(\frac{\beta_n}{\sqrt{\alpha_P}}a)\right\}$$

$$T_W(r,t)=\frac{\alpha_P}{k_P}\int_{\tau=0}^{t}d\tau[\int_{r'=0}^{a}(r')^2 G_{WP}(r,t\mid r',\tau)A(1+\cos 2\omega_m\tau)dr']$$
$$=\frac{\alpha_P}{k_P}\sum_{n=1}^{500}\left\{A\left[\frac{1}{\beta_n{}^2}(1-\exp(-\beta_n{}^2 t))+\frac{1}{\beta_n{}^4+4\omega_m{}^2}(\beta_n{}^2\cos 2\omega_m t+2\omega_m\sin 2\omega_m t-\beta_n{}^2\exp(-\beta_n{}^2 t))\right]\times\right. \tag{4}$$
$$\left.\frac{1}{N_n}\frac{k_P}{\alpha_P}\frac{1}{\sqrt{r}}\left(A_n J_{1/2}(\frac{\beta_n}{\sqrt{\alpha_W}}r')+B_n Y_{1/2}(\frac{\beta_n}{\sqrt{\alpha_W}}r')\right)\frac{\sqrt{\alpha_P}}{\beta_n}a^{3/2}J_{3/2}(\frac{\beta_n}{\sqrt{\alpha_P}}a)\right\}$$

Since the tem perature distribution in the phantom and water is known, the temperature distribution can be determ ined and is shown in Figure 3. In Figure 3 the solid line represents the radial temperature distribution from the center of the phantom to its boundary (5 mm), while the dashed li ne represents the te mperature distribution when only the phantom being heated and not the surrounding water . The dif ferent colors illustrate how the temperature distribution evolves as a f unction of time. From Figure 3 it is seen th at the tem perature in the phantom is being reduced at the boundary due to heat conduction to surrounding water. This effect acts as a negative factor for steady-state electromagnetic illumination.

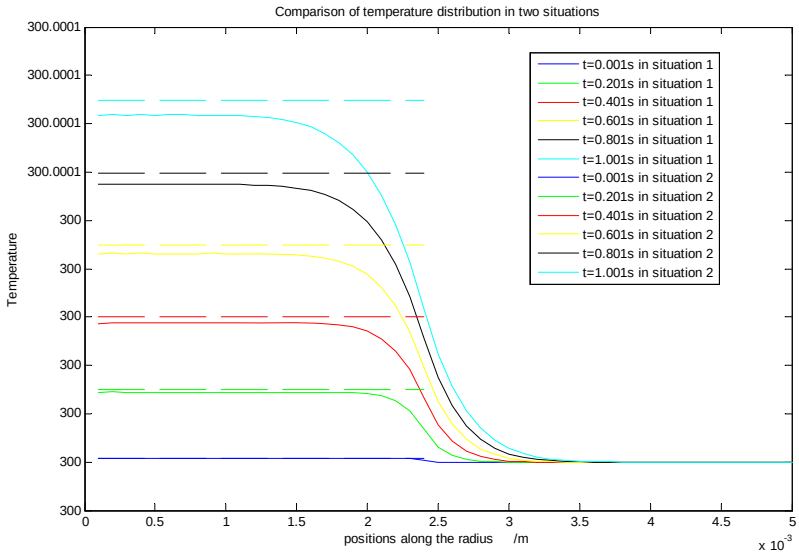

Figure 3: Temperature distribution.

Generally speaking, the temperature in phantom will present a linear increasing trend, together with a sm all sinusoidal oscilla tion upon it, caused by th e modulating signal.

The governing equation describing the acoustic pressure wave is the wave equation, which can be expressed as:

$$\nabla^2 p_s - \frac{1}{c_s^2}\frac{\partial^2 p_s}{\partial t^2} = \frac{-\beta}{C_p}\frac{\partial H}{\partial t} \tag{5}$$

In (5), p_s is the sound pressure, c_s is the sound speed, β is the thermal expansion coefficient, C_p is the heat capacity, and H is the heating function of the phantom. In solving this equation, the heat conduction issue discussed above should be taken into consideration, namely that the heating function should be expressed as:

$$H(r,t) = A(1+\cos\omega t) - H'(r,t) \tag{6}$$

The first item on the right side of Equation (6) represents the electromagnetic heating, while the second item represents the heat conduction into water. Including the thermal conduction considerations discussed Equation (7) must satisfy:

$$H(r,t) = \rho C_p \frac{\partial T(r,t)}{\partial t} \tag{7a}$$

and hence

$$\frac{\partial H(r,t)}{\partial t} = \rho C_p \frac{\partial^2 T(r,t)}{\partial t^2} \tag{7b}$$

At this point, it is assumed that the temperature distribution is a linear function of time with a small superimposed sinusoidal oscillation. This may be expressed as:

$$T(r,t) = A(r)t + \Delta T(\omega)\cos(\omega t) \tag{8a}$$

giving

$$\frac{\partial H(r,t)}{\partial t} = \rho C_p \Delta T(\omega)\omega^2 \cos(\omega t) \tag{8b}$$

Applying the Diebold solution one obtains:

$$\frac{\partial H(r,t)}{\partial t} = \alpha I_0 \omega e^{-j\omega t} \Rightarrow \alpha I_0 = \rho C_p \Delta T(\omega)\omega \tag{9}$$

Equation (9) can now be substituted into the Diebold solution resulting in the acoustic pressure wave expressed as the result of the sinusoidally increasing temperature

component, namely,

$$p_f = \frac{j\omega\beta c_s \rho_s a \Delta T(\omega)}{\hat{r}} \left(\frac{(\sin q - q\cos q)\frac{1}{q^2}}{\left(1 - \frac{\rho_s}{\rho_f}\right)\frac{\sin q}{q} - \cos q + j\frac{\rho_s c_s}{\rho_f c_f}\sin q} \right) e^{-jq\hat{r}} \qquad (10)$$

The temperature increase ΔT can be estimated from the heat conduction analysis above.

It is difficult to analytically decouple the pressure wave generation excited by the CW excitation and heat conduction effects. It is apparent from the above analysis that for the case of CW excitation, the heat conduction effects will greatly attenuate the electromagnetic illumination. The only way to mitigate this attenuation is to use significantly larger CW excitation. Short of doing this, the signal is generally too weak to be detected.

II.2 Phantom Development

(a) Phantom Modeling

A tissue phantom for thermal acoustic imaging should match the living tissue's electrical as well as acoustic properties. The preliminary phantom development is focused on matching dielectric properties, specifically permittivity and conductivity. According to Duck [7], the relative permittivity of malignant breast tissue at a range encompassing 434 MHz ranges between 36-56, and the conductivity ranges between 0.35-0.8 S/m. The phantom was made from TX-151 powder (from Oil Research Center), tap water, cane sugar and potassium chloride, according to methods developed at The McKnight Brain Institute at the University of Florida by Beck [8]. The dielectric properties are controlled by varying the concentration of the cane sugar and potassium chloride. An HP85070B coaxial probe and HP8752C network analyzer measured the dielectric properties. A preliminary sample was created using the experience of the staff of the McKnight Brain Institute in creating brain tissue models that have dielectric properties similar to that of malignant tissue. An iterative process of measuring the dielectric constants and manipulating the cane sugar and potassium chloride concentration was conducted until a suitable phantom was created. The tissue phantom created is used in the excitation system. A diagram of the experiment is shown in Figure 4. The cylinder height is 10.3 inches and the inner diameter is 7.25 inches. The transducer used in the experiment is a 0.5 inch diameter piezoelectric immersion transducer from Olympus NDT (model V303). It has a center frequency of 0.91 MHz and 60.275%, -6 dB bandwidth. At 1 MHz, the

half angle beam width is approxim ately 3.5°. R eciprocity calibra tions w ill be performed in de-ionized water . The wa veguide used is from Penn Engineering Components (model WR 187) with a frequency range of 3.95-5.85 GHz.

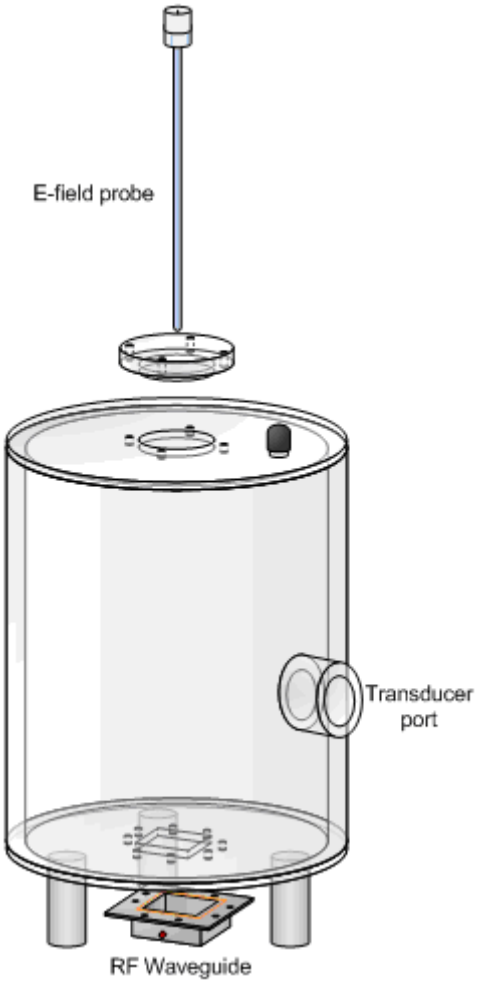

Figure 4: Phantom experimental setup.

(b) Initial Phantom Resonance Experiments

Experimentation designed to verify acous tic resonance of the tum or phantom by electromagnetic excitation, w ith the experi ment setup show n schem atically in Figure 1, consists of an electrom agnetic wavegui de, two ultrasonic transducers (one for transmission ant the other for sensing), a nd a Plexiglas cy linder that contain s the de-ionized water and tumor pha ntom. The cylinder height is 10.3 inches and the inner diameter is 7.25 inches. The tran sducer used in the experim ent is a 0.5 inch diam eter piezoelectric immersion transducer from Olympus NDT (model V303). It has a center frequency of 0.91 MHz and 60.275%, -6 dB bandwidth. At 1 MHz, the half angle beam width is approxim ately 3.5°. Reci procity calibrations are perform ed in de-ionized water. The waveguide used is from Penn Engineering Com ponents (model WR 187) with a frequency range of 3.95- 5.85 GHz. In the experim ents, a 1 cm

diameter sample of the phantom is suspended in the center of the cylinder, submerged in de-ion ized w ater, and aligned w ith the ultra sonic tr ansducers. The transm itting transducer is m ounted to the side of the cylinder with the trans ducer face exposed to the de-ionized water. The rece iving transducer is similarly aligned and its axis m akes a 180-degree with respect to the first transducer. The electrom agnetic waveguide provides excitation from the bottom of the cy linder. Electric field probes are ins erted through a port in the top of the cylinder and are used to measure total f ield intensity along the cylinder axis. Two probes are need ed: one to m easure the radial field intensity an d another to determ ine the axia l field strength. The ra dial field probe is shown in Figure 8. The goal of the prelim inary setup is to achieve a uniform field within a 3 cm radius around the phantom . The frequency of the 434 MHz radio frequency signal can be am plitude modulated over a range on the order of 400 kHz to 4 MHz, which is th e expected ran ge the resonant frequency of the phantom . The acoustic signal from the phantom is m easured by the ultrasonic transducer and is recorded by the NI data acquisition system.

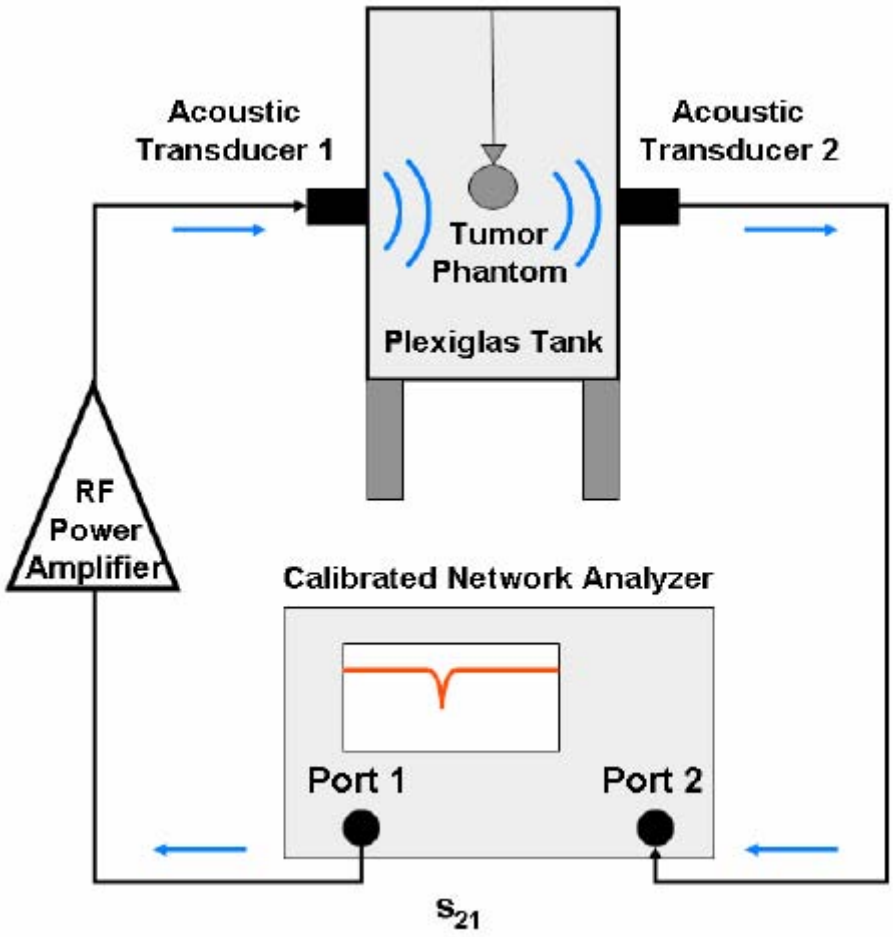

Figure5: Test setup for determining the resonant frequency of the tumor phantom.

Initially, the tum or's resonant frequenc y is established acoustically. Referring to Figure 5, a swept sinusoidal signal generated emanating from Port 1 of an RF network

analyzer acts as a source which drives one acoustic tran sducer while the secon d acoustic transducer, used to receive the acoustic signal, drives port 2. W ith the tumor absent from the wate r-filled tank, the receiv ed signa l c onsists of the acoustic frequency characteristics of the tank itself, and this frequency response is used as a reference to calibrate the network analyzer. The sam e sweep is then perform ed with the tumor phantom present and the response no w contains the resonant characteristics of the phantom . A typical frequency respons e is shown in Figure 6 where it is seen that the resonant frequency occurs between around 1 MHz.

For TAI sys tems the acoustic pres sure wave is generated as the tumor is heated via application of EM energy. Having establishe d the resonant frequency of the phantom using the a coustic tech nique descr ibed, a sig nal w ith th is f requency am plitude modulated at 434 MHz EM carrier signal is then used to drive the waveguide located at the botto m of the tank via an RF power am plifier. The acoustic transducer is the n used to sense the acoustic pressure wave generated by the TAI process.

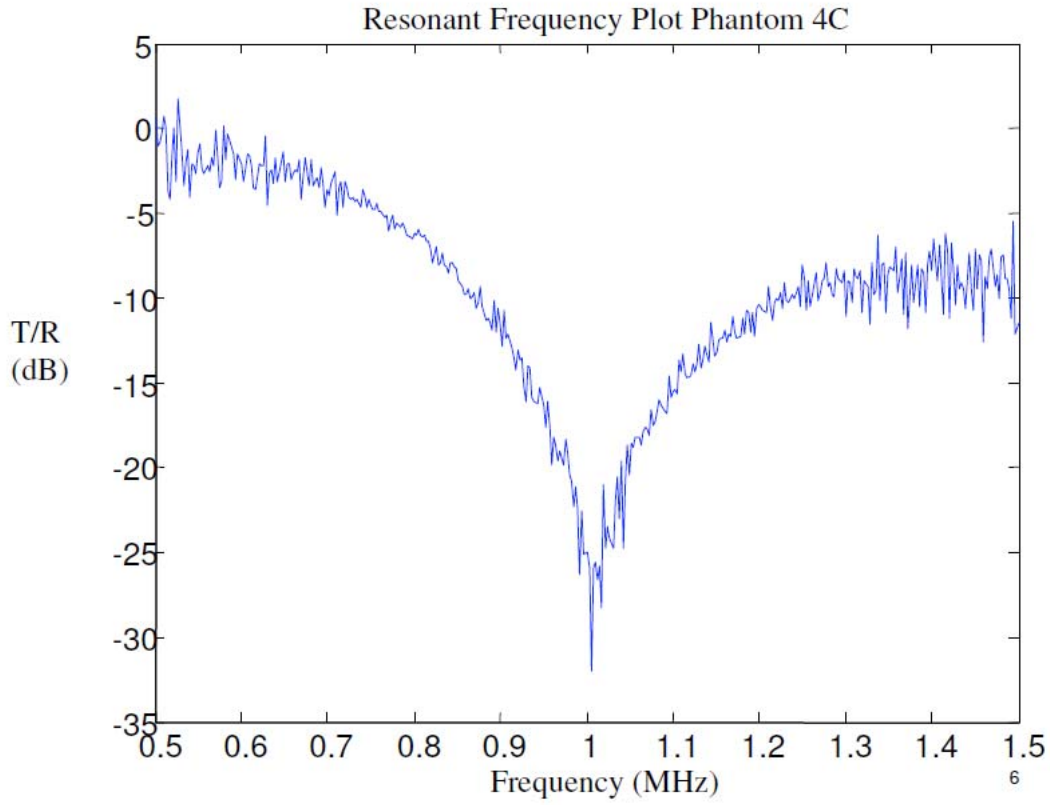

Figure 6: A typical frequency response of acoustic resonance.

(c) Phantom Aging Characteristics

While carry ing out these m easurements, it becam e apparent the large num ber of variables in volved in c haracterizing the resonance of the phantom , one being the

effect of aging of the phantom over time. Subsequently, some time was focused to characterize the phantom aging. One of the aspects explored was the variation of the resonant frequency over time. Figure 7 shows results based on the experimental setup described in the previous section and shown in Figure 5. While the sample size consists of only 3 phantoms, the general trend seems to be that the resonant frequency initially increases before it decreases over time. More specimens need to be studied to confirm this trend. In Figure 7, phantom c exhibited no apparent resonance in week one. This was attributed to phantom placement in the cylinder. The setup was consequently altered in a way that would insure repeatable phantom placement. Phantom aging is important to quantify in order to minimize experimental error over time. Other properties are currently being examined including density and speed of sound.

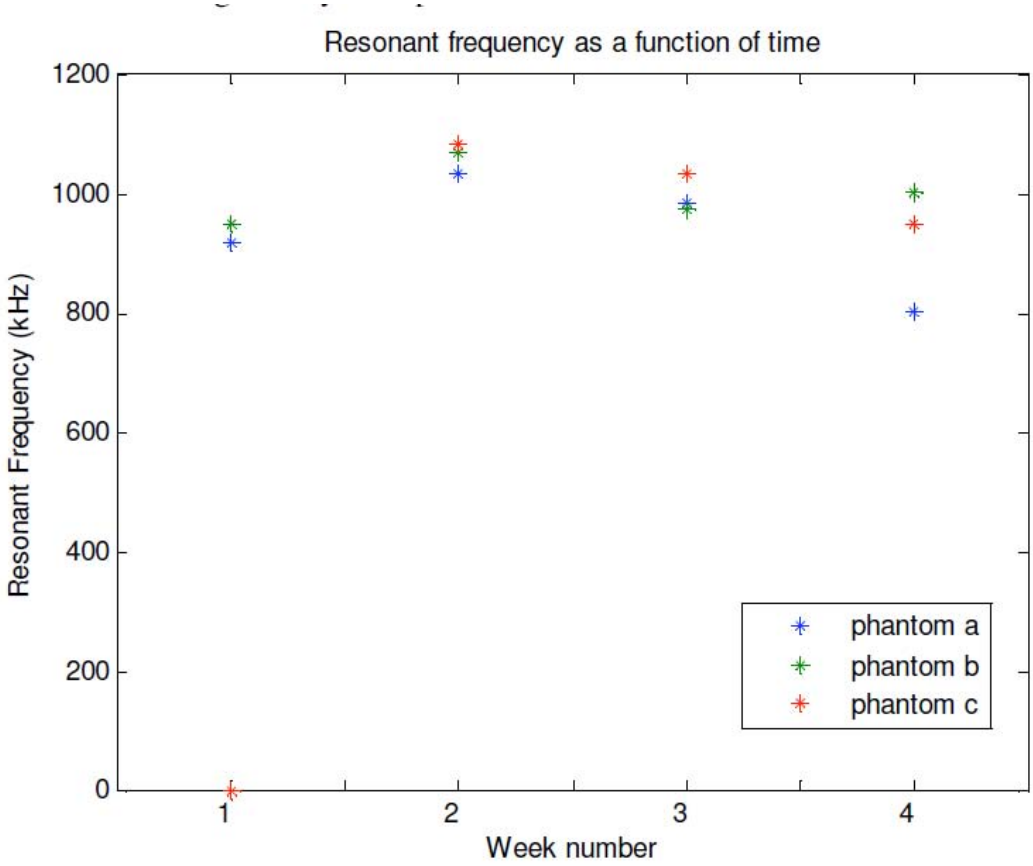

Figure 7: Resonant frequency of phantom over time. Note no resonance was found for phantom c in the first week.

(d) Electric Field Measurements

Accurate modeling of both the acoustical and electrical behavior of the system forms an essential component of this research effort. Of special concern is the ability to model electrical-to-acoustical transduction aspect of this system. The acoustic

pressure wave to be measured is generated when the modulated electrical signal heats the phantom causing it to mechanically undulate. This heating occurs as a result of the electric field intensity in the location of the conducting phantom . As a consequence not only must the electrical fields present in this system be accurately modeled, but these fields must also be verified so that the proper heating parameters may be used as input to the acoustic model. Initially an off-the-shelf, low-profile, high-resolution probe that measures the electric potential (Carsten Associates Model E-601) was used. Once the potential is known a differencing procedure can be used to determine the field. It was found, however, that this method proved inadequate for the present system. In particular, the common mode signal measured far outweighed the difference signal and an accurate estimate of the electric field could not be determined. Further, the metal shaft of the probe, though small in diameter, was distorting the field in the tank. To remedy these, two custom probes, one used to measure the axial field, another used to measure the radial field were designed. Since the new probes measure the electric field directly no differencing is required. Furthermore the new probes are design with a shaft that is impedance-matched to the impedance of de-ionized water thus making the probe transparent except of course (unavoidably) for the immediate region being measured. To date the radial field probe has been obtained and is shown in Figure 8. Shown also in Figure 8 is a Transverse Electro-Magnetic (TEM) test cell used for probe calibration. One end of the TEM cell is excited with a 434 MHz signal while the other end is terminated in a 50-ohm load. Since the dimensions of the cell are precisely known, the electric field in the cell's center is also known. This center portion of the TEM cell is filled with de-ionized water in which the probe is inserted, and the resulting voltage is measured using a 50-ohm oscilloscope. Once the axial filed probe is completed, an accurate field map of the tank along the axis where the phantom will be placed will be obtained. Once again this data will be used to verify the electromagnetic model and link the electrical and acoustic models.

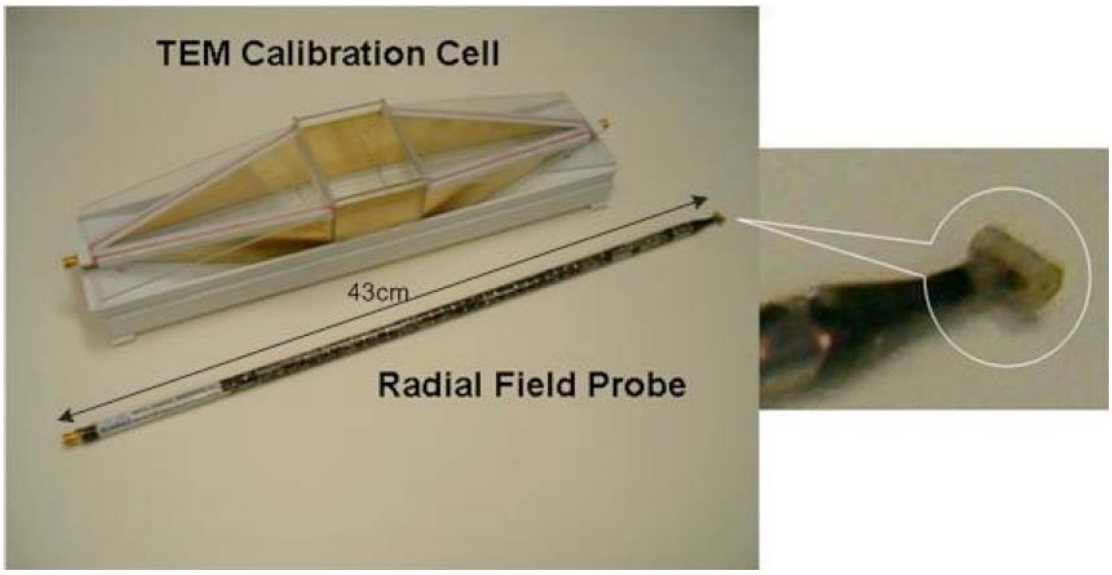

Figure 8: Radial field probe and probe calibration cell.

(e) Electrical-to-Acoustical Transduction

To date two problems have been encountered with regard to accurately measuring the RTAI effect and are currently being remedied. The first regards drift of the acousticacoustic resonance measurements. Since the acoustic transducers possess narrow beamwidths, accurate placement of the phantom is required for a stable resonance. Secondly the acoustic resonance varies with the temperature of the water. Initially the acoustic and electrical portions of the experimental procedure where performed consecutively. It has been determined that monitoring the acoustic resonance while the electrical measurements are taken is essential. Furthermore, to date the electrical (RF) power level has been kept low with a total drive power of less than four watts. This requires that the measurement bandwidth be kept small so as to not allow excessive noise in the measurements. A new RF power amplifier capable of producing a drive power of up to 100-watts has been obtained. This, along with accurate placement of the phantom's location will allow for a robust, stable measurement of the RTAI effect.

II.3 Electromagnetic Stimulation

(a) Tumor Phantom

For TAI systems the acoustic pressure wave is generated as the tumor is heated via application of EM energy. For a proof-of-concept level demonstration of the TAI process, the EM excitation is accomplished with the experimental setup shown in Figure 9. A Plexiglas tank in the shape of a right circular cylinder (length = 10.29 in., radius = 4 in) is filled with de-ionized water with relative permittivity $\varepsilon/\varepsilon_o = 81$, and conductivity $\sigma \approx 0$. The quality of the reconstructed image is directly related to the uniformity of the EM excitation in the cavity. For the cavity dimensions used here, the EM field will be the sum of several cavity modes, and a uniform EM field can only be approximated with multiple exciters. For the present case, a single source is used to excite the cavity so a uniform field is not expected. The RF excitation is achieved using a coax-to-waveguide adapter (WR-187) which has an operating frequency range of 3.95 – 9.85 GHz. Though the frequency of the exciting signal is 434 MHz, a value typical for medical imaging systems, to minimize mismatch between the waveguide exit aperture and the water-filled tank, the waveguide itself is water-filled, thus reducing the wavelength in the waveguide to 3.0 in., and thus operating the exciting waveguide within its recommended range.

The tumor is simulated by means of a membrane filled with a gel that provides the desired permittivity and conductivity. This tumor will be suspended from the top of the cavity along the axis of the cylinder at a location of a local maximum of electric

field. The location of the maximum electric field is determined by using a low-profile, high-resolution E-field probe (C arstens Associates Model E-601). The probe impedance is 50 Ω and the relative s ignal intensity is m easured with an RF spectru m analyzer. The probe tip is tr anslated along the ax is of the cylinder and the location(s) of the maximum field is determined. The tumor is then placed at this location with the E-field probe removed.

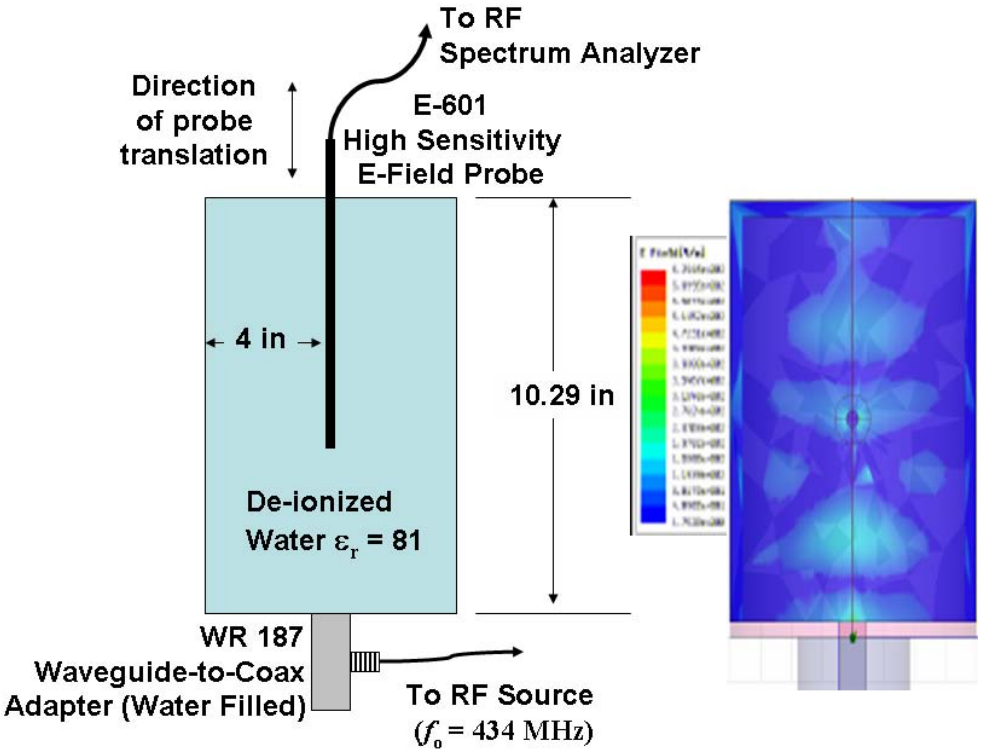

Figure 9: Schematic representation of the experimental setup used to excite and measure the cavity's axial electric field. Also shown is the electric field obtained under assumed operating conditions using a FDTD simulation.

The constru ction of th e tes t se t-up as desc ribed is com plete. Th e R F signal is generated with a signal s ynthesizer am plified with a power am plifier capable of providing an output power on the order of 10 watts. The acoustic signal generated by the tumor expansion will be de tected with a pressure sensor(s) as described elsewhere in this report.

Anticipated ele ctromagnetic perf ormance has been m odeled by m eans of a Finite Difference T ime Do main (FDTD) si mulation program . Si nce the size of the cavity used along with the fac t that it is filled with a h igh permittivity material suggests that several cavity m odes w ill exist, w ith the total f ield equaling the sum of these m odal fields. Electromagnetic modeling along with due consideration of the cavity's acoustic properties provided the guidelines used to d etermine th e cavity d imensions. For example, the specific cylinder leng th and di ameter was selected in part by ensu ring that, via num erical sim ulations, the electric field was not at a spatial null along the cylinder axis and that at least one electr ic field peak occurred along this axis. For

simulation purposes, the high dielectric permittivity – air interface was modeled by a perfect magnetic conductor (PMC) at all cavity boundaries. The relative amplitude of the electric field is shown along side the cavity's schematic representation in Figure 9.

(b) Hemispherical breast model

Use of the RTAI concept as a real imaging application requires extending the approach to a three-dimensional system. As the experimental portion of present phase of the research effort continues so does the modeling for the next phase of the effort which involves three-dimensional modeling, simulation, and measurements.

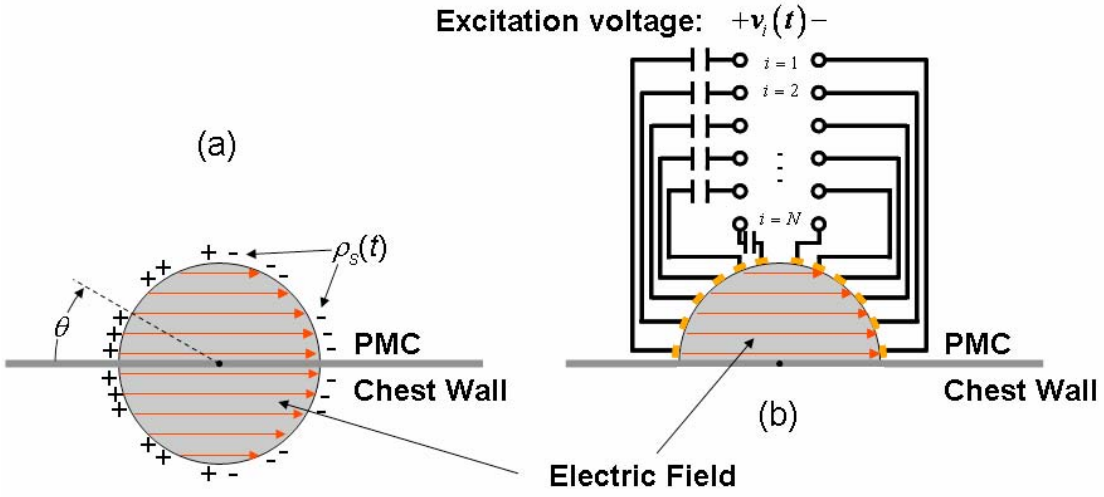

Figure 10: Motivation for achieving a uniform field within a hemispherical region using small, capacitively coupled patches.

Figure 10 illustrates conceptually how the required uniform electric field for a realistic breast phantom can be achieved in a simple and practical manner. Consider the situation shown in Figure 10(a) which illustrates a dielectric sphere of arbitrary permittivity in free space. It is well known in electromagnetic theory that a sinusoidally distributed surface charge distribution, $\rho_s = \rho_0 \cos\theta$, with ρ_0 as a constant, placed on the surface of the sphere results in a perfectly uniform electric field inside the dielectric sphere as shown. By invoking the theory of images a Perfect Magnetic Conductor (PMC), which represents a good model for the chest wall, can be placed as shown without altering the electric field in the sphere. In this way a uniform electric field in a hemispherical region that models the human breast can be obtained. Obtaining such a surface charge distribution is, in general not possible, though it can be approximated in a pointwise fashion as illustrated in Figure 10(b). There it is seen that small (subresonant) patches can be placed on the breast so as to approximate a uniform electric field inside the breast. These (metal) patches would be coated with a non-conducting material and hence modeled as capacitively coupled as shown. The

concept is akin to the approach used to obtain a uniform, circularly polarized transverse magnetic field from discrete wire cage structure in Magnetic Resonance Imaging (MRI) applications. Though the perfectly uniform field would be obtained only for the case of an electrostatic charge distribution, it is not unreasonable to expect a quasi-static solution which reasonably approximates the ideal, static situation under appropriate conditions, and this is currently being explored. To illustrate the basic idea, Figure 11 shows a pointwise electrostatic approximation to the continuous case using 31 point charges uniformly distributed over the breast phantom surface as indicated in Figure 11(b). The magnitudes of the point charges are chosen so that they equal the value of the continuous charge distribution at that point. This would serve, for example, as a good initial guess for a numerical optimization procedure which would give the optimum charge distribution that provide the most uniform electric field magnitude in the breast. Figure 11(c) shows the (unoptimized) electrostatic field intensity over several planes in the region to be imaged. It is seen that even for this simple case that the field intensity varies by less than 1 dB in the central region to be imaged. This approach is currently being developed analytically as well as being modeled using two commercially available software packages.

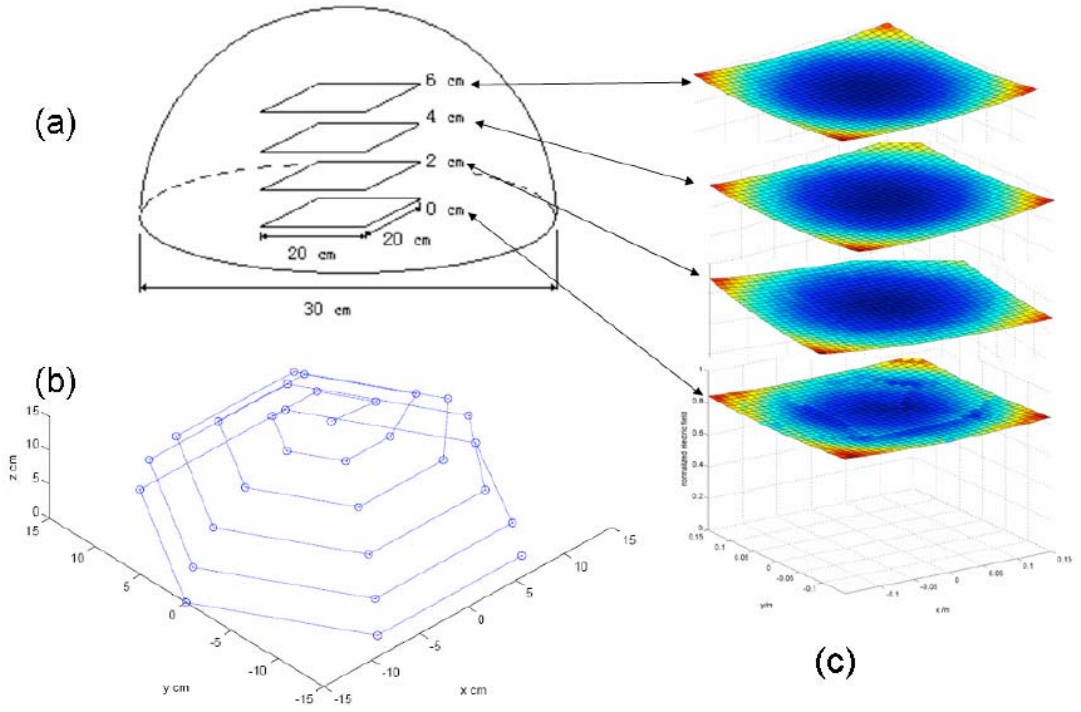

Figure 11: Simulated uniform electric field (quasi TEM) for a hemispherical shell excited by small patches.

II.4 Experiment

(a) Experimental Setup

Several attempts were made to increase the electromagnetic field in the phantom to a level sufficient to measure the resulting acoustic signal. The acoustic transducer was placed as close to the phantom as possible. The specific acoustic transducer used was a hydrophone, since these are characterized as having a high sensitivity over a broad acoustic frequency band. The experimental setup is illustrated in Figure 12. The exciting RF waveguide aperture is extended to the center of the tank so as to increase electromagnetic field intensity in the vicinity of the phantom.

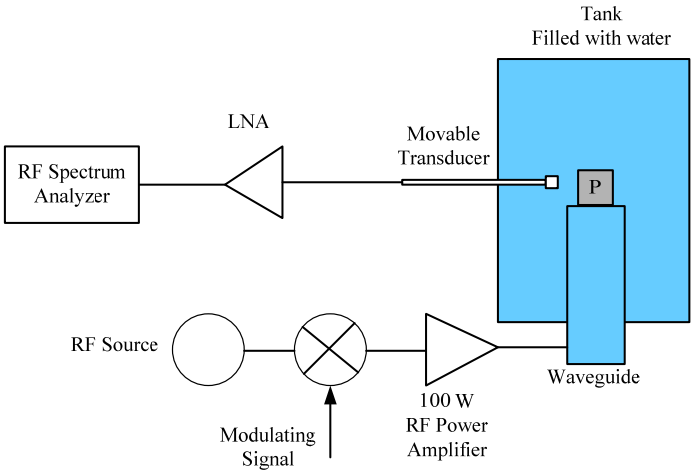

Figure 12: Experimental setup.

Much time has been invested into the construction of appropriate phantoms. The current generation of phantoms is being constructed in cooperation with the Department of Biomedical Engineering at the University of Florida. Earlier version of the phantoms were made from a mixture of a saline solution with a gelling agent, and needed to be held in a latex container so as to maintain the desired shape. Surface tension effects will inhibit the phantom from freely oscillating to some degree. The newer generation of phantoms is made in a manner that provides a self-supporting structure and can be placed directly in the water bath.

A typical baseband signal as viewed on a spectrum analyzer is shown in Figure 13. The anticipated amplitude of the acoustic pressure wave that would be generated with the present experimental setup is quite small, and RF interference effects, generated by amplifier nonlinearities, coupled directly though waveguide and tank onto the metal housing of the transducer. This is evidenced by the fact that these same peaks exist even in the absence of the phantom inside the tank. Multiple peaks are the result of the higher order harmonics of RF input signal. It has been experimentally verified that the closer the transducer is placed to the phantom, and hence to the exciting waveguide, the stronger interference signal that is picked up.

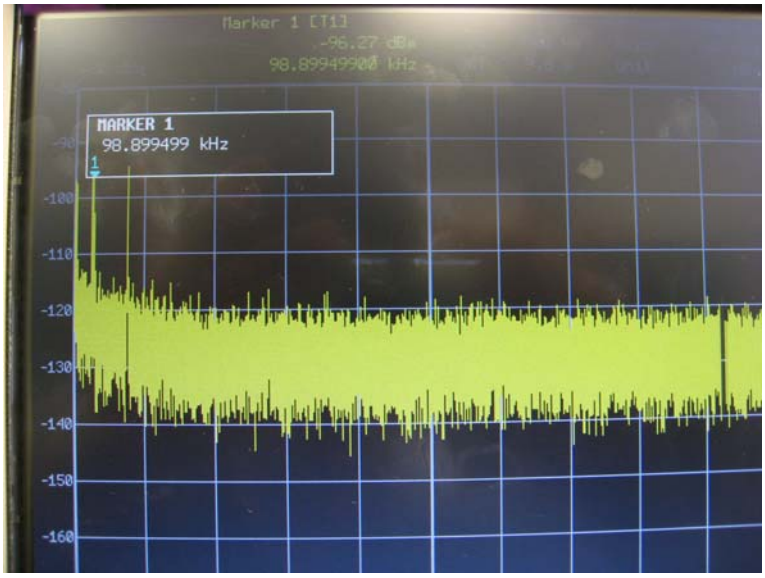

Figure 13: Typical baseband signal.

Based on these observations, a low pass filter was added after the transducer to reduce the high frequency interference. The tank assembly was also placed inside a Faraday shield to further reduce interference with the measurement equipment. The original ultrasonic transducer (V303, Panametrics NDT) was replaced with a hydrophone (TC 4035, Reson) which has a broad bandwidth (from 10 kHz to 800 kHz) and a flat frequency response. The modified experimental setup is shown in Figure 14.

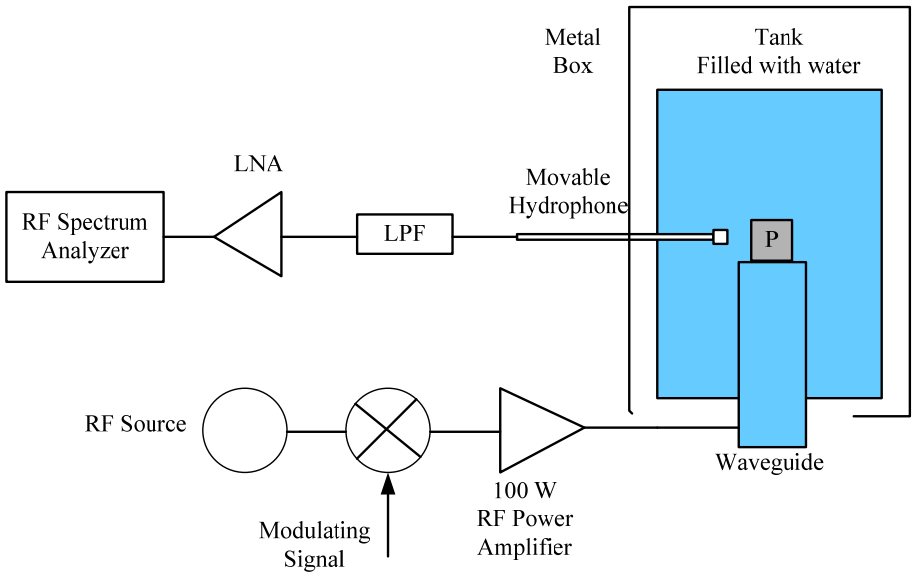

Figure 14: Modified experiment setup.

These modifications resulted in a substantial reduction in the aforementioned interference signals. Measurement of a thermo-acoustic signal with a dynamic range sufficient for high-fidelity imaging was still problematic. The low RF power level used for the RF excitation serves as the primary reason for difficulties encountered with signal measurement. Power levels used in these experiments are nearly two

orders of m agnitude lower than that of other researchers [2, 9-1 1]. The heat conduction into the water bath, as previously discussed, also served to m ask the thermo-acoustic s ignal. A coustic dissipa tion m echanisms add f urther dif ficulties, making it harder to isolate th e acoustic pressure w ave generated by the phantom from other effects.

(b) Experimental Results and Analysis

The first step in m easuring any thermoacous tic resonance is the determ ination of the noise floor of the overall m easuring system, including the equivalent noise pressure present at the transdu cer. Experim ental de termination of the tran sducer sens itivity [12], in conjunction with the noise floor of the overall m easurement system gives the equivalent noise pressure as a function of frequency shown in Figure 15. It is observed that the equivalent noise pressure is greater th an the estim ated acoustic pressure signal obtained from simulations . M itigation of this problem requires a lowering of the overall noise floor and/or increase in RF power level.

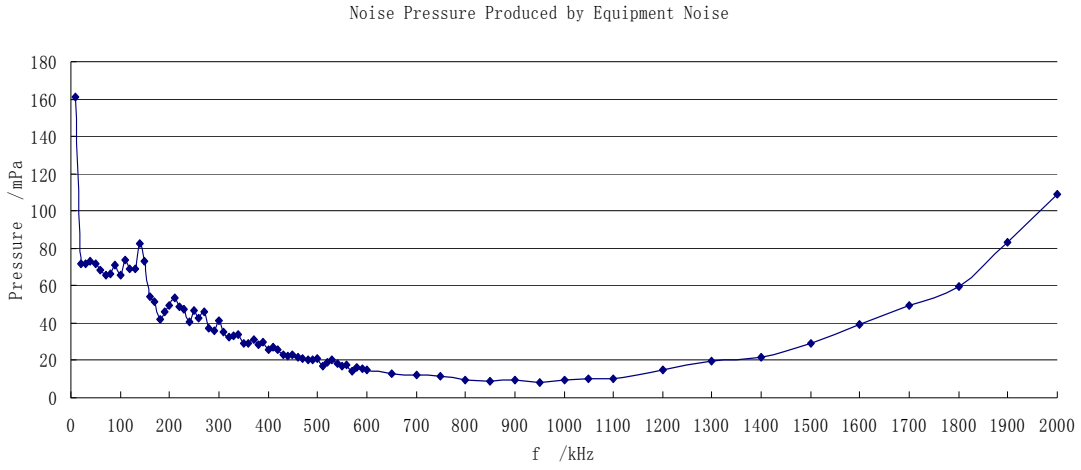

Figure 15: Equivalent noise pressure of overall measurement system.

It can be sated with a high degree of confidence that the single most significant factor resulting in the dif ficulty to d etect a thermo-acoustic s ignal is in sufficient R F excitation (power). Other researchers have succeeded in obtaining an acoustic signa l used a puls ed microwave source with peak power ranging from 10 kW to 20 kW [2, 9-11]. Therefore, in order to obtain the therm o-acoustic signal n ecessary for generating im ages, a high power pulsed microwave source has been obtained. Presently a pulsed source capable of s upplying 0.75 m icrosecond pulses at a pulse repetition rate of 1 100 Hz and a peak power up to 12 0 kW is cu rrently b eing integrated into the ex perimental set up. (Radio-Resea rch Instrum ent Co, P/N 12-1-21MOD). This new experim ental setup is shown in F igure 16. Parts acquisition and construction of this system is currently underway.

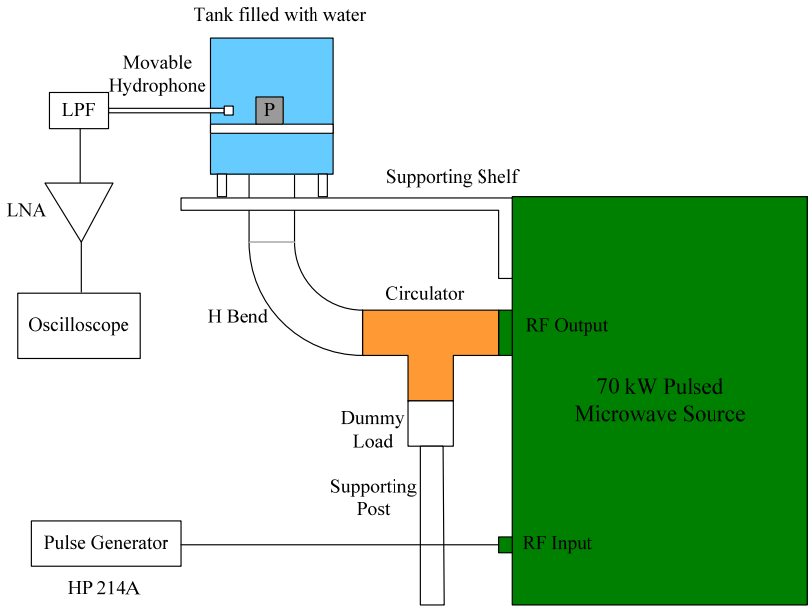

Figure 16: New experiment setup.

With the use of a one m icrosecond pulse d m icrowave source with a peak power ranging from 20 kW to 120 kW , it is fully ex pected that the th ermo-acoustic signal should be found using an oscilloscope. Th ere are m any open research areas where improvement of the i maging system perfor mance can be realized, and th e use of the high-power pulsed source will now allow investigation on these areas. Firstly, the RF aperture must be engineered to generate an appropriately conditioned excitation signal in the ph antom. Secondly , w ith th e high pow er lev els n ow availab le, nonlin ear phenomenon can be explored. Since the input power can be high, the phantom itself may exhibit nonlinear ef fects which m ay be exploited. Thirdly, the data acquisition system using high speed ADC's and a FPGA development platform can be optimized for optimal signal integrity for imaging applications. One common solution would be to use of f-the-shelf di gitizer car ds to i mplement the DAQ sy stem, and t hese can get expensive since many channels are needed. However, one high speed ADC and FPGA development board c an be used to im plement a m ultiplexer-based d ata acqu isition system, greatly redu cing cost. Finally , the aco ustic transd ucers w ill ultim ately b e replaced with an array of MEMS sensors in an optical configuration.

II.5 Adaptive Image Formation Algorithms

Developing accurate and robust im age reconstruction methods is o ne of the key challenges encountered in T AI. Various im age r econstruction algorithms have been developed for T AI. By using Radon tran sformation on the T AI data function, reflectivity tom ography reconstruction al gorithms can be used for T AI im age reconstruction [13]. Exact in verse solutions have been found for dif ferent scanning geometries in both the frequency dom ain [14, 15] and the tim e domain [16, 17].

Approximate reconstruction algorithms, such as the time-domain Delay-and-Sum (DAS) beamforming method [18, 19] and the optimal statistical approach [20], have also been proposed. However, a common assumption of these existing methods is that the surrounding tissue is acoustically homogeneous. This approximation is inadequate in many medical imaging applications. According to previous studies, the sound speed in human female breast varies widely from 1430 m/s to 1570 m/s around the commonly assumed speed of 1510 m/s [21, 22]. The heterogeneous acoustic properties of biological tissues cause amplitude and phase distortions in the recorded acoustic signals, which can result in significant degradations in imaging quality.

Four robust and adaptive image formation algorithms, named as adaptive and robust methods of reconstruction (ARMOR), multifrequency adaptive and robust technique (MART), automatic multifrequency adaptive and robust technique (AMART), and iterative adaptive approach (IAA), have been developed and applied to the TAI system.

ARMOR is based on robust Capon beamforming (RCB) [23]. This technique can be used to mitigate the amplitude and phase distortion problems in TAI by allowing certain uncertainties. Specifically, in the first step of ARMOR, RCB is used for waveform estimation by treating the amplitude distortion with an uncertainty parameter. In the second step of ARMOR, a simple yet effective peak searching method is used for phase distortion correction. Compared with other energy- or amplitude-based response intensity estimation methods, peak searching can be used to improve image quality with little additional computational costs. Moreover, since the acoustic pulse is usually bipolar: a positive peak, corresponding to the compression pulse, and a negative peak, corresponding to the rarefaction pulse, we can further enhance the image contrast in TAI by using the peak-to-peak difference as the response intensity for a focal point.

Instead of a single frequency source a multiple frequency source is employed in MART. MART can offer higher signal-to-ratio (SNR) and higher imaging contrast than its single frequency counterpart, which we refer to as the single-frequency adaptive and robust technique (SART), since much more information about the human breast can be harvested from the multiple frequencies. Furthermore, the interference due to inhomogeneous breast tissue can be suppressed more effectively since more information about the breast tissue can be used by the RCB algorithm. MART is a three-stage time-domain signal processing algorithm. In Stage I, RCB is used to estimate the thermal acoustic responses from the focal points within the breast for each stimulating frequency. Then in Stage II, a scalar acoustic waveform at each focal point is estimated based on the response estimates for all frequencies from Stage I. Finally, in Stage III, the positive peak and the negative peak of the estimated acoustic waveform at each grid location are determined, and the peak-to-peak difference is computed and referred to as the image intensity.

The above two algorithms, as well as most of the existing robust schemes, are user

parameter dependent and it may not be a simple task to determine the user parameters in practice. Therefore, user parameter-free robust adaptive approaches, including a shrinkage-based general linear combination (GLC) algorithm, are desirable [24, 25].

We have proposed an automatic (i.e., user parameter free) multifrequency adaptive and robust technique (AMART) based on GLC for TAI to achieve high resolution and good interference suppression capability. AMART is a three-stage imaging algorithm. Specifically, in the first stage of AMART, GLC is used to estimate the thermal acoustic responses from the grid points within the breast for each stimulating frequency. Based on these estimates, a scalar acoustic waveform at each grid point is estimated via GLC at the second stage. At the final stage, the energy of the estimated acoustic waveform at each grid point is computed and referred to as the image intensity.

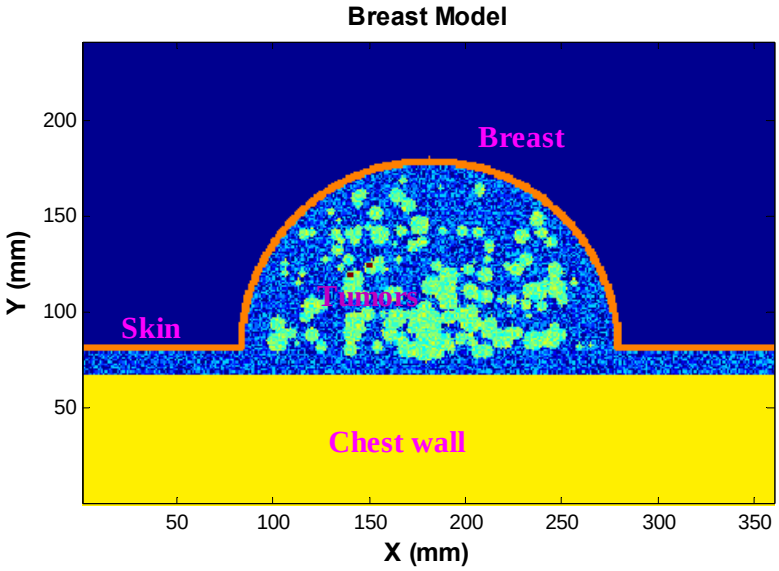

Figure 17: Breast model.

To validate the effectiveness of the proposed algorithms, we have developed a 2-D inhomogeneous breast model, as shown in Figure 17. This breast model includes skin, breast fatty tissues, glandular tissues, and the chest wall. Small tumors are set below the skin. The finite-difference time-domain (FDTD) method is used to simulate the electromagnetic field inside the breast tissues [26, 27]. The specific absorption rate (SAR) distribution is calculated based on the simulated electromagnetic field [28, 29]. Then FDTD is used again to simulate the propagation of the thermal acoustic waves [30, 31]. In the following example, the thermal acoustic signals are simulated based on the aforementioned 2-D model. Multiple stimulating frequencies from 200-800 MHz with frequency step 100 MHz are used for MART. Two small 1.5-mm-diameter tumors are set inside the breast model. Their locations are at (X=70 mm, Y=60 mm) and (X=75 mm, Y=62.5 mm). The distance between the two tumors is 4 mm. For

comparison purposes, the DAS method is applied to the same data set. The reconstructed images are shown in Figure 18. Figure 18(a) is the imaging result obtained by DAS. The DAS image contains much clutter and cannot show the tumors clearly. Figures 18(b) and 18(c) show the imaging results obtained by ARMOR and MART. The two tumors are seen clearly in the ARMOR and MART images, and the sizes and the locations of the two tumors are accurate. However, the performance of ARMOR is a little worse than that of MART because some clutter show up in the ARMOR images. Both ARMOR and MART need a user parameter, which is fixed at 0.3N, where N is the number of the receiver elements. Figure 18(d) is the imaging result obtained by the user parameter free algorithm, AMART. The image shows the sizes and locations of the two tumors accurately. The advantage of AMART, compared with ARMOR and MART, is that it is user parameter free and have easy to use.

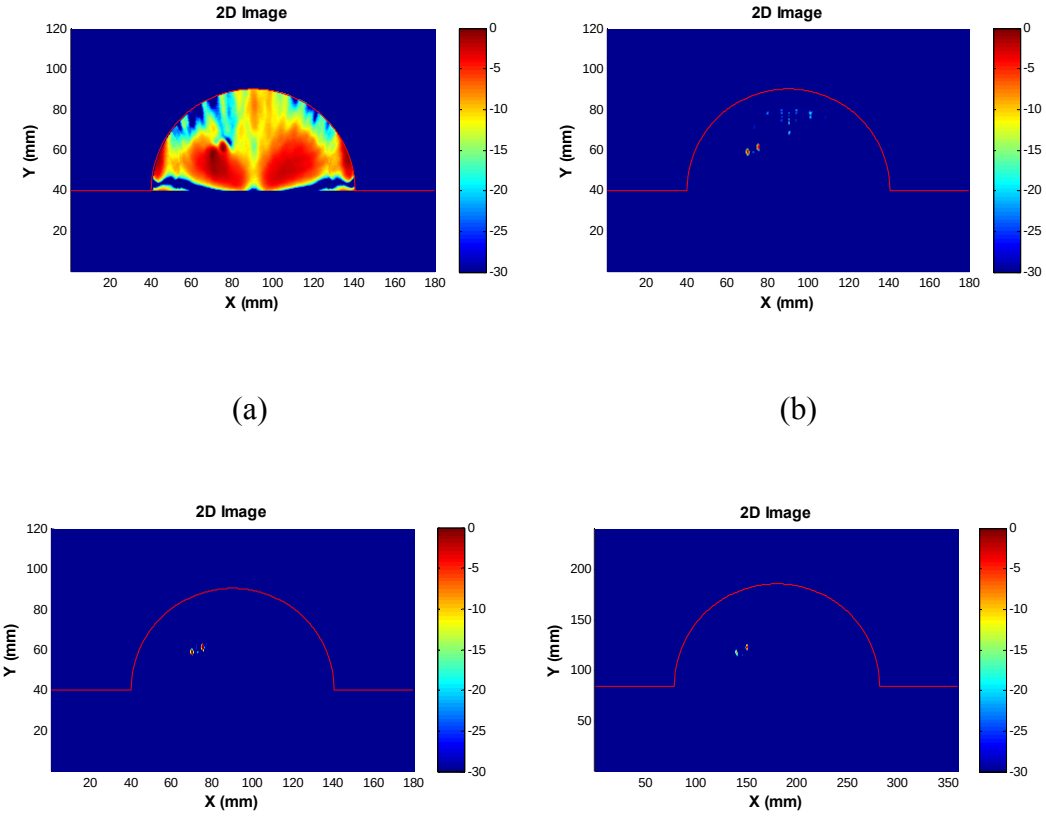

(a) (b)

(c) (d)

Figure 18: Reconstructed images. (a) DAS, (b) ARMOR, (c) MART, and (d) AMART.

Recently, a weighted least squares-based non-parametric and user parameter-free iterative adaptive approach (IAA) [32] was proposed in array processing and other sensing applications. IAA can work well with few snapshots (even one), uncorrelated, partially correlated, and coherent sources, and arbitrary array geometries. However, due to the properties of TAI, including wideband signals and near-field environment, we cannot apply IAA directly, since it is designed for narrowband signals originally.

We extend the IAA approach to the wideband scenario by applying Fourier transform to the time-domain array output to transform the wideband data into narrowband frequency bins. Then IAA can be applied to each frequency bin to estimate the signal spectral distribution and hence estimate the signal waveform and the backscattered energy. Figure 19 is the imaging result obtained by IAA. The breast model used for the simulation is the same as the one shown in Figure 17. The early time response from the skin is removed. To obtain the signals, we perform the simulation twice at each stimulating frequency, with and without the tumor, and record the acoustic data. The difference of the two received signals is referred to as the thermal acoustic response only from the tumor. The two tumors are clearly shown in the IAA image, and the sizes and the locations of the two tumors are accurate.

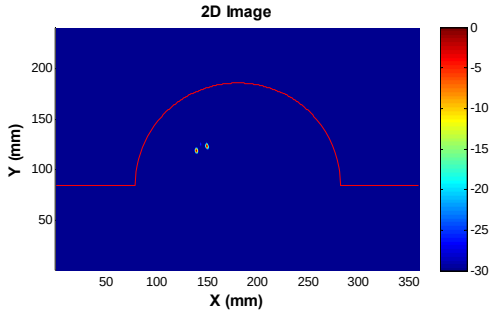

Figure 19: Reconstructed image of IAA.

III. Key Research Accomplishments

- Phantom was developed and properties as a function of aging were explored.
- Equipment needed for excitation and elect ric field m easurements were identified and purchased (please see Table 1 for details).

Vendor	Model number	Equipment purchased	Qt.
Panametrics	V303-SU Ultrasonic	Immersion Transducer	2
	BCU-74-6W	Cables. W aterproof &BNC to UHF . 6'. RG174/U	2
	BCU-58-10W	Cable. W aterproof &BNC to UHF . 10 '. RG58/U	1
	5662 Ultrasonic	Preamplifier	1
National Instruments	763000-01 Power	Cord	1
	778644-01	NI PXI-1045 Front Rack Moun t Kit for 19 " Rack	1
	778644-02	NI PXI-1045 Rear Rack Mount Kit f or 19" Rack	1
	778645-01	NI PXI-1045 18-Slot 3U PXI Chassi s with Universal AC Power Supply	1
	779505-03	NI PXI-PCI e8361, MXI-Express, 1 Port PCIe, 3 m Cable	1
	960597-18	PXI 18-Slot Factory I nstallation Servi ce and Extended Warranty	1
	778739-01	NI PXI-2529 High Density Multiconfi guration Matrix	1
	NI PXI-5122	Dual 100 MS/s, 14-Bit Digitizer w/ anti-alias filters & 8 MB/ch	16
	778840-01	NI TB-2634 Configures the NI PXI-2529 High Density Matrix	1
	779079-02	NI PXI-5671 RF Signal Generator	1
	Shippi	ng	1
TMR		Plexiglass Cylinder	1
Penn Engineering	1452-4A W	aveguide	1
	6352-5	Silicon Gasket (price included in waveguide)	
Bruce Carst en Assoc.	EG01-12" Probes		2
	EFP 200R	Calibrated radial probe	1
	EFP 200A	Calibrated axial probe	1
Mini-Circuits ZH	L-100W -52-S	Broadband Amplifier	1
Acopian W530M	T1 3	Power supply	1

Table 1. Equipment purchased.

- Experimental setup to detect the thermal acoustic waves from the simulated tumor was formulated.
- A 3-D electromagnetic stimulation system is being simulated and developed.
- Robust and adaptive im age for mation algorithms, including ARMOR, MAR T, AMART, and IAA, were developed.
- A 2-D inhomogeneous breast m odel, whic h inc ludes sk in, breast f atty tiss ues, glandular tissues, and the chest wall, wa s developed to validate the ef fectiveness of the signal processing algorithms.

IV. Reportable Outcomes

Y. Xie, B. Guo, J. Li, G . Ku, and L. V. Wang, “Adaptive and Robust Methods of Reconstruction (ARMOR) for Thermoacoustic Tomography,” IEEE Transactions on Biomedical Engineering, Vol. 55, No. 12, pp. 2741-2752, December 2008.

B. Guo, and J. Li " Waveform Diversity Based Ultrasound System for Hyperthermia Treatment of Breast Cancer ," IEEE Transaction on Biomedical Engineering, vol. 55, no. 2, pp. 822-826, February 2008.

B. Guo, J. Li, H. Zmuda, and M. Sheplak, “Multi-Frequency Microwave Induced Thermal Acoustic Imaging for Breast Cancer Detection,” IEEE Transactions on Biomedical Engineering, Vol. 54, No. 11, pp. 2000-2010, November 2007.

L. Du, J. Li, and P. Stoica, “User Parameter Free Approaches to Multistatic Adaptive Ultrasound Imaging,” The 2008 IEEE International Symposium on Biomedical Imaging, Paris, France, May 2008.

V. Personnel Receiving Pay

- Manuel Arreola
- Brandon Bertolucci
- Lou Cattafesta
- Rodney Dagulo
- Lin Du
- Xin Guan
- Bin Guo
- Arsen Ivanov
- Ruixin Jiang
- Jian Li
- Mark Sheplak
- Alina Soderholm
- Susan Trumpler
- John Vinod
- Yao Xie
- Ming Xue
- Xumin Zhu
- Yiping Zhu
- Henry Zmuda

VI. Conclusions

Numerical analysis about the electro-acoustic transduction of the phantom has been investigated, based on the Diebold's research [5], in order to get a more clear understanding about the entire picture. The major factors determining the frequency response of electro-acoustic transduction have been pointed out, and some material parameters are being measured based on specifically designed experiments.

The entire excitation and detection system has been set up, including modulated signal source, high power amplifier (100 W), low noise amplifier and data acquisition system. Relative programming has been completed and tested concerning the control of the entire system. The noise floor of the measurement system has been obtained and referred to the input of transducer, which provides the clear comparison between the signal level simulated and noise floor measured. Phantoms are being redesigned to gain more conductivity and higher resonant frequency. Other modifications of the system are being conducted in order to enlarge the signal level and hence, get higher SNR.

Four robust and adaptive image formation algorithms, ARMOR, MART, AMART, and IAA, have been developed for the TAI system. The excellent performance with high resolution and good interference suppression capability of these algorithms has been demonstrated based on a 2-D breast model. Moreover, the new AMART and IAA algorithms avoid the need to specify any user parameters and hence are easy to use in practice.

VI. References

[1] R. A. Kruger, *et. al.*, "Thermoacoustic CT with Radio Waves: A Medical Imaging Paradigm1," *Radiology,* 211, pp. 275–278, 1999.

[2] L. V. Wang, *et. al.*, "Microwave-induced acoustic imaging of biological tissues," *Review of Scientific Instruments*, vol. 70, no. 60, 1999.

[3] G. Ku and L. V. Wang, "Scanning thermoacoustic tomography in biological tissue," *Med. Phys.* 27 .5, May 2000.

[4] R. A. Kruger, *et. al.*, "Breast Cancer in Vivo: Contrast Enhancement with Thermoacoustic CT at 434 MHz -- Feasibility Study," *Radiology,* 216, pp. 279-283, 2000.

[5] G. J. Diebold and P. J. Westervelt, "The photoacoustic effect generated by a spherical droplet in a fluid," *J. Acoust. Soc. Am.* 84(6), December 1988.

[6] Geng Ku and Lihong V. Wang, "Scanning thermoacoustic tomography in biological tissue", *Med. Phys.* 27, 5, May 2000.

[7] F. A. Duck, *Physical properties of tissue : a comprehensive reference book* (San Diego, London), 1990

[8] B.L. Beck, Tissue-Equivalent Phantoms for High Frequencies. *Concepts in Magnetic Resonance Part B (Magnetic Resonance Engineering)*, vol. 20 B(1) 30-33, 2004

[9] Robert.A.Kruger, *et al*, "Thermoacoustic CT with RadioWaves: A Medical Imaging Paradigm", *Radiology*, 1999; 211:275–278.

[10] Lihong.V.Wang, *et al*, "Microwave-induced acoustic imaging of biological tissues", *REVIEW OF SCIENTIFIC INSTRUMENTS*, 1999.9, vol. 70, number 60.

[11] Robert.A.Kruger, *et al*, "Breast Cancer in Vivo: Contrast Enhancement with Thermoacoustic CT at 434 MHz-- Feasibility Study", *Radiology*, 2000; 216: 279-283.

[12] R. R. Dagulo, *Ultrasonic Transducer Calibration*. Thesis of Bachelor of Science in Aerospace Engineering, Fall 2008.

[13] M. A. Anastasio, J. Zhang, X. Pan, Y. Zou, G. Ku, and L. V. Wang, "Half-time image reconstruction in thermoacoustic tomography," *IEEE Trans. Med. Imag.*, vol. 24, pp. 199-210, Feb. 2005.

[14] Y. Xu, D. Feng, and L. V. Wang, "Exact frequency-domain reconstruction for thermoacoustic tomography: I. Planar geometry," *IEEE Trans. Med. Imag.*, vol. 21, pp. 823-828, 2002.

[15] Y. Xu, M. Xu, and L. V. Wang, "Exact frequency-domain reconstruction for thermoacoustic tomography: II. Cylindrical geometry," *IEEE Trans. Med. Imag.*, vol. 21, pp. 829-833, 2002.

[16] M. Xu and L. V. Wang, "Time-domain reconstruction for thermoacoustic tomog-raphy in a spherical geometry," *IEEE Trans. Med. Imag.*, vol. 21, pp. 814-822, Jul. 2002.

[17] M. Xu, Y. Xu, and L. V. Wang, "Time-domain reconstruction algorithms and numerical simulations for thermoacoustic tomography in various geometries," *IEEE Trans. Biomed. Eng.*, vol. 50, pp. 1086-1099, Sep. 2003.

[18] C. G. A. Hoelen and F. F. M. de Mul, "Image reconstruction for photoacoustic scanning of tissue structures," *Applied Optics*, vol. 39, no. 31, pp. 5872-5883, 2000.

[19] D. Feng, Y. Xu, G. Ku, and L. V. Wang, "Microwave-induced thermoacoustic tomography: Reconstruction by synthetic aperture," *Med. Phys.*, vol. 28, pp. 2427-2431, Dec. 2001.

[20] Y. V. Zhulina, "Optimal statistical approach to optoacoustic image reconstruction," *Applied Optics*, vol. 39, no. 32, pp. 5971-5977, 2000.

[21] G. Kossoff, E. K. Fry, and J. Jellins, "Average velocity of ultrasound in the human female breast," *J. Acoust. Soc. Am.*, vol. 53, no. 6, pp. 1730-1736, 1973.

[22] T. Szabo, *Diagnostic Ultrasound Imaging: Inside Out*. Academic Press, Sept. 2004.

[23] J. Li, P. Stoica, and Z. Wang, "On robust Capon beamforming and diagonal loading," *IEEE Transactions on Signal Processing*, vol. 51, pp. 1702-1715, July 2003.

[24] L. Du, T. Yardibi, J. Li, and P. Stoica, "Review of user parameter-free robust adaptive beamforming algorithms," *Digital Signal Processing – A Review Journal*, vol. 19, no. 4, pp. 567-582, July 2009.

[25] L. Du, J. Li, and P. Stoica, "Fully automatic computation of diagonal loading levels for robust adaptive beamforming," to appear in *IEEE Transactions on Aerospace and Electronic Systems*, April 2010.

[26] A. Taflove and S. C. Hagness, *Computational Electrodynamics: The Finite-Difference Time-Domain Method*. Boston, MA: Artech House, second edition, 2000.

[27] D. M. Sullivan, *Electromagnetic Simulation Using the FDTD Method*. New York, NY: IEEE Press, 2000.

[28] P. Bernardi, M. Cavagnaro, S. Pisa, and E. Piuzzi, "Specific absorption rate and temperature elevation in a subject exposed in the far-fileld of radio-frequency sources operating in the 10-900-MHz range," *IEEE Transactions on Biomedical Engineering*, vol. 50, pp. 295-304, March 2003.

[29] P. Bernardi, M. Cavagnaro, S. Pisa, and E. Piuzzi, "SAR distribution and temperature increase in an anatomical model of the human eye exposed to the field radiated by the user antenna in a wireless LAN," *IEEE Transactions on*

Microwave Theory and Techniques, vol. 46, pp. 2074-2082, December 1998.

[30] J. G. Maloney and K. E. Cummings, "Adaptation of FDTD techniques to acoustic modeling," *11th Annual Review of Progress in Applied Computational Electromagnetics, Monterey, CA*, vol. 2, pp. 724-731, 1995.

[31] X. Yuan, D. Borup, J. Wiskin, M. Berggren, and S. A. Johnson, "Simulation of acoustic wave propagation in dispersive media with relaxation losses by using FDTD method with PML absorbing boundary condition," *IEEE Transactions on Ultrasonics, Ferroelectrics, and Frequency Control*, vol. 46, pp. 14-23, January 1999.

[32] T. Yardibi, J. Li, P. Stoica, M. Xue, and A. B. Baggeroer, "Source Localization and Sensing: A Nonparametric Iterative Adaptive Approach Based on Weighted Least Squares," *IEEE Transactions on Aerospace and Electronic Systems*, to appear.

VII. Appendices

"Adaptive and Robust Methods of Rec onstruction (ARMOR) for Therm oacoustic Tomography"

"Waveform Diversity Based Ultrasound System for Hyperthermia Treatment of Breast Cancer"

"Multi-Frequency Microwave Indu ced Ther mal Acoustic Im aging for Breast Cancer Detection"

"User Parameter Free Approaches to Multistatic Adaptive Ultrasound Imaging"

Adaptive and Robust Methods of Reconstruction (ARMOR) for Thermoacoustic Tomography

Yao Xie*, *Student Member, IEEE*, Bin Guo, *Member, IEEE*, Jian Li, *Fellow, IEEE*, Geng Ku, and Lihong V. Wang, *Fellow, IEEE*

***Abstract*—In this paper, we present new adaptive and robust methods of reconstruction (ARMOR) for thermoacoustic tomography (TAT), and study their performances for breast cancer detection. TAT is an emerging medical imaging technique that combines the merits of high contrast due to electromagnetic or laser stimulation and high resolution offered by thermal acoustic imaging. The current image reconstruction methods used for TAT, such as the delay-and-sum (DAS) approach, are data-independent and suffer from low-resolution, high sidelobe levels, and poor interference rejection capabilities. The data-adaptive ARMOR can have much better resolution and much better interference rejection capabilities than their data-independent counterparts. By allowing certain uncertainties, ARMOR can be used to mitigate the amplitude and phase distortion problems encountered in TAT. The excellent performance of ARMOR is demonstrated using both simulated and experimentally measured data.**

***Index Terms*—Array signal processing, biomedical acoustic imaging, robustness.**

I. Introduction

THERMOACOUSTIC tomography (TAT), the earliest investigation of which dates back to the 1980s [1], has recently attracted much interest with its great promise in a wide span of biomedical applications (see, e.g., [2]–[4]). Its physical basis lies in the contrast of the radiation absorption rate among different biological tissues. Due to the thermoacoustic effect, when a short electromagnetic pulse (e.g., microwave or laser) is absorbed by the tissue, the heating results in expansion that generates acoustic signals. In TAT, an image of the tissue absorption properties is reconstructed from the recorded thermoacoustic signals. Such an image may reveal the physiological and pathological status of the tissue, which can be useful in many applications including breast cancer detection [5]. Compared with microwave imaging and ultrasound imaging, TAT combines their merits and possesses both fine imaging resolution and good spatial contrast properties [4].

Developing accurate and robust image reconstruction methods is one of the key challenges encountered in TAT. Various image reconstruction algorithms have been developed for TAT. By using Radon transformation on the TAT data function, reflectivity tomography reconstruction algorithms can be used for TAT image reconstruction [6]. Exact inverse solutions have been found for different scanning geometries in both the frequency domain [7], [8] and the time domain [9], [10]. Approximate reconstruction algorithms, such as the time-domain delay-and-sum (DAS) beamforming method [11], [12] and the optimal statistical approach [13], have also been proposed. However, a common assumption of these existing methods is that the surrounding tissue is acoustically homogeneous. This approximation is inadequate in many medical imaging applications. According to previous studies, the sound speed in human female breast varies widely from 1430 to 1570 m/s around the commonly assumed speed of 1510 m/s [14], [15]. The heterogeneous acoustic properties of biological tissues cause amplitude and phase distortions in the recorded acoustic signals, which can result in significant degradation in imaging quality [16].

In ultrasound tomography (UT), wavefront distortion due to heterogeneity of biological tissue has been studied extensively. Various wavefront correction methods have been proposed [17]. However, they are not highly effective at correcting severe amplitude distortions [18], and they usually involve complicated procedures. The problem in TAT is somewhat different from that in UT. In the breast UT, the amplitude distortion caused by refraction is more problematic than the phase distortion induced by acoustic speed variation. In TAT, however, even for the biological tissue, such as the breast tissue, with a relatively weak heterogeneity, phase distortion dominates amplitude distortion [16]. These unique features suggest that new adaptive and robust imaging techniques should be designed especially for TAT.

Time-domain approximate reconstruction algorithms, such as the DAS (weighted or unweighted) type of data-independent approaches have various applications in medical imaging. They need little prior information on the tissue for image reconstruction and can be fast and simple to implement to process the wideband acoustic signals. Although not based on the exact solution, they provide similar image qualities to those of the exact reconstruction algorithms. However, these data-independent methods tend to suffer from poor resolution and high-sidelobe-level problems. Data-adaptive approaches, such as the recently

Manuscript received May 8, 2007; revised October 22, 2007. First published February 25, 2008; current version published December 17, 2008. This work was supported in part by the National Institutes of Health (NIH) under Grant 1R41CA107903-1, in part by the U.S. Army Medical Command under Contract W81XWH-06-1-0389, and in part by the National Natural Science Foundation of China under Grant 60428101. *Asterisk indicates corresponding author*.

*Y. Xie was with the Department of Electrical and Computer Engineering, University of Florida, Gainesville, FL 32611-6130 USA. She is now with the Department of Electrical Engineering, Stanford University, Stanford, CA 94305 USA.

B. Guo was with the Department of Electrical and Computer Engineering, University of Florida, Gainesville, FL 32611 USA. He is now with the Department of Electrical and Computer Engineering, Duke University, Durham, NC 27708 USA.

J. Li is with the Department of Electrical and Computer Engineering, University of Florida, Gainesville, FL 32611 USA.

G. Ku and L. V. Wang are with the Department of Biomedical Engineering, School of Engineering and Applied Science, Washington University in St. Louis, St. Louis, MO 63130-4899 USA.

Color versions of one or more of the figures in this paper are available online at http://ieeexplore.ieee.org.

Digital Object Identifier 10.1109/TBME.2008.919112

0018-9294/$25.00 © 2008 IEEE

Authorized licensed use limited to: University of Florida. Downloaded on January 29, 2010 at 14:45 from IEEE Xplore. Restrictions apply.

introduced robust Capon beamforming (RCB) method [19], can have much better resolution and much better interference rejection capability than their data-independent counterparts.

We propose adaptive and robust methods of reconstruction (ARMOR) based on RCB for TAT. ARMOR can be used to mitigate the amplitude and phase distortion problems in TAT by allowing certain uncertainties. Specifically, in the first step of ARMOR, RCB is used for waveform estimation by treating the amplitude distortion with an uncertainty parameter. In the second step of ARMOR, a simple, yet effective, peak searching method is used for phase distortion correction. Compared with other energy- or amplitude-based response intensity estimation methods, peak searching can be used to improve image quality with little additional computational costs. Moreover, since the acoustic pulse is usually bipolar: a positive peak, corresponding to the compression pulse, and a negative peak, corresponding to the rarefaction pulse [11], we can further enhance the image contrast in TAT by using the peak-to-peak difference as the response intensity for a focal point. We will demonstrate the excellent performance of ARMOR by using both data simulated on a 2-D breast model and data experimentally measured from mastectomy specimens.

The remainder of this paper is organized as follows. In Section II, we formulate the problem of interest. Sections III–V describe the first, second, and third steps of ARMOR, respectively. Examples based on simulated and real-world experimental data are presented in Section VI. Finally, Section VII provides the conclusions.

II. Problem Formulation

Consider a TAT imaging system, as shown in Fig. 1(a). A stimulating electromagnetic (laser or microwave) pulse is absorbed by the biological tissue under testing, which causes a sudden heat change (of the order of 10^{-4} °C [20]). Due to the thermoacoustic effect, an acoustic pulse is generated that can be recorded by an ultrasonic transducer array. The transducer array may be a real aperture array or a synthetic aperture array formed by rotating a sensor around the tissue and recording the acoustic waves at different locations. We assume that the number of transducers in the array (or in the synthetic aperture array case, the number of transducer data acquisition locations) is M. Each transducer is assumed to be omnidirectional; mutual couplings among the transducers are not considered in our model as they can be tolerated by our robust algorithms to a certain extent. The recorded acoustic signals are sufficiently sampled and digitized and a typical recorded pulse is shown in Fig. 1(b) (based on the data measured on the breast specimen II described in Section VI).

The data model for the sampled and digitized acoustic signal recorded by the mth transducer is given by:

$$x_m(n) = s_m(n) + \tilde{e}_m(n), \quad m = 1, \ldots, M. \tag{1}$$

where n is the discrete time index, starting from t_0 after the excitation pulse. The scalar $s_m(n)$ denotes the signal component, which corresponds to the acoustic pulse generated at a focal point, and $\tilde{e}_m(n)$ is the residual term, which includes unmodeled noise and interference (caused by other sources within the tissue).

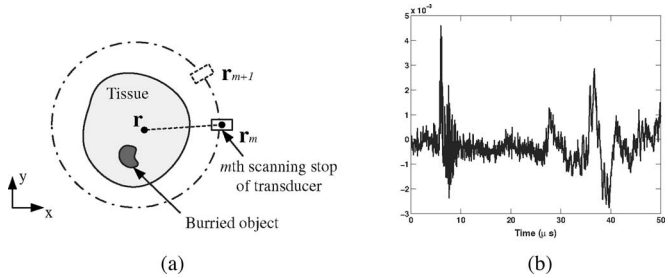

Fig. 1. (a) A schematic of a 2-D synthetic-aperture-based TAT scanning system. (b) A typical acoustic pulse recorded by a transducer (for data measured from breast specimen II).

The goal of ARMOR is to reconstruct an image of thermoacoustic response intensity $I(\mathbf{r})$, which is directly related to the absorption property of the tissue, from the recorded data set $\{x_m(n)\}$. Herein, the (2-D or 3-D) vector $\mathbf{r}$ denotes the focal point location coordinate. To form an image, we scan the focal point location $\mathbf{r}$ to cover the entire cross section of the tissue (the transducers can acquire signals at different heights; for each height, a 2-D cross-sectional image can be reconstructed and a 3-D image can be formed from the 2-D images). We allow certain uncertainties in ARMOR to deal with amplitude and phase distortions caused by the background heterogeneity.

The discrete arrival time of the pulse (for the mth transducer) can be determined approximately as

$$t_m(\mathbf{r}) = \left\lfloor -\frac{t_0}{\Delta t} + \frac{\|\mathbf{r} - \mathbf{r}_m\|}{\Delta t v_0} \right\rfloor. \tag{2}$$

We will omit the dependence of the arrival time $t_m(\mathbf{r})$ on $\mathbf{r}$ hereafter for notational simplicity. Here, Δt is the sampling interval, and the 3-D vector $\mathbf{r}_m$ denotes the location of the mth transducer. The sound speed v_0 is chosen to be the average sound speed of the biological tissue under interrogation. The notation $\|\mathbf{x}\|$ denotes the Euclidean norm of $\mathbf{x}$, and $\lfloor y \rfloor$ stands for rounding to the greatest integer less than y. The second term in (2) represents the time-of-flight between the focal point and the mth transducer.

The signal components $\{s_m(n)\}_{m=1}^M$ are approximately scaled and shifted versions of a nominal waveform $s(t)$ at the source

$$s_m(n) \approx \frac{\exp\left(-\alpha\|\mathbf{r} - \mathbf{r}_m\|\right)}{\|\mathbf{r} - \mathbf{r}_m\|} \cdot s(n - t_m) \tag{3}$$

where α is the attenuation coefficient in Nepers/m. In TAT, the major frequency components of the acoustic signals take a relatively narrow band, and are usually lower than those in UT [16]. Hence, we can approximate α as a frequency-independent constant.

We preprocess the data to time delay all the signals from the focal point $\mathbf{r}$ and compensate for the loss in amplitude due to propagation decay. Let $y_m(n)$ denote the signal after preprocessing to backpropagate the detected signal to the source

$$y_m(n) = \exp\left(\alpha\|\mathbf{r} - \mathbf{r}_m\|\right) \cdot \|\mathbf{r} - \mathbf{r}_m\| \cdot x_m(n + t_m). \tag{4}$$

Authorized licensed use limited to: University of Florida. Downloaded on January 29, 2010 at 14:45 from IEEE Xplore. Restrictions apply.

Then, the received vector data model can be written as

$$\mathbf{y}(n) = \mathbf{a}_0 s(n) + \mathbf{e}(n), \quad n = -N, \cdots, N \tag{5}$$

where $\mathbf{a}_0$ is the corresponding steering vector, which is approximately equal to $\bar{\mathbf{a}} = [1, \ldots, 1]^T$, $\mathbf{y}(n) = [y_1(n), \ldots, y_M(n)]^T$, $\mathbf{e}(n)$ represents the noise and interference term after preprocessing, and $(\cdot)^T$ denotes the transpose. Here, we define the time interval of interests for the signal $\mathbf{y}(t)$ to be from $-N$ to N, which means that we only take N samples before and after the approximate arrival time given in (2) for the focal point at $\mathbf{r}$. The value of N should be chosen large enough so that the interval from $-N$ to N covers the expected signal duration in the region of interest.

In reality, both the amplitude and the phase (or pulse arrival time) of the acoustic pulse will be distorted. A major cause for these distortions is the acoustically heterogeneous background. Amplitude distortion is mainly due to the interferences caused by multipath, which is inevitable in the heterogeneous medium: refraction occurs due to acoustic speed mismatch across the tissue interface; consequently, acoustic pulses arrived at the transducer will be via different routes and interfere with each other. On the other hand, phase distortion is mainly caused by the nonuniform sound speed. For example, in human female breast, the sound speed can vary from 1430 to 1570 m/s; therefore, the actual arrival time will fluctuate around the approximately calculated time given in (2). Moreover, an inaccurate estimate of t_0 (t_0 is aligned with the focal point's signal arrival time) and the transducer calibration error may also contribute to the phase distortion. Amplitude and phase distortion will blur the image, raise the image background noise level, lower the values of the object of interest, and, consequently, decrease the image contrast [16].

We mitigate the effects of these distortions by allowing $\mathbf{a}_0$ to belong to an uncertainty set centered at $\bar{\mathbf{a}}$ and by considering the signal arriving within the interval from $-N$ to N.

III. Step I of ARMOR: Waveform Estimation

The first step of ARMOR is to estimate the waveform of the acoustic pulse generated by the focal point at location $\mathbf{r}$, based on the data model in (5). It will appear that we have neglected the presence of phase distortion by using this data model in the first step. However, by allowing $\mathbf{a}_0$ to be uncertain, we can tolerate some phase distortions as well. This approximation causes little performance degradation to our robust algorithm.

Covariance-fitting-based RCB [21] is used to first estimate the steering vector $\mathbf{a}_0$, and use the estimated $\mathbf{a}_0$ to obtain an optimal beamformer weight vector for pulse waveform estimation. By assuming that the true steering vector lies in the vicinity of the nominal steering vector $\bar{\mathbf{a}}$, we consider the following optimization problem [19]

$$\max_{\sigma^2, \mathbf{a}_0} \sigma^2 \quad \text{subject to} \quad \hat{\mathbf{R}} - \sigma^2 \mathbf{a}_0 \mathbf{a}_0^T \succeq 0, \quad \|\mathbf{a}_0 - \bar{\mathbf{a}}\|^2 \leq \varepsilon, \tag{6}$$

where $\mathbf{A} \succeq 0$ means that the matrix $\mathbf{A}$ is positive semidefinite, σ^2 is the power of the signal of interest, and

$$\hat{\mathbf{R}} = \frac{1}{2N+1} \sum_{n=-N}^{N} \mathbf{y}(n) \mathbf{y}^T(n) \tag{7}$$

is the sample covariance matrix. The second constraint in (6) is a spherical uncertainty set; an elliptical uncertainty set can be used instead, if a tighter constraint is desirable [21].

The parameter ε in (6) determines the size of the uncertainty set and is a user parameter. To avoid the trivial solution of $\mathbf{a}_0 = 0$, we require that

$$\varepsilon < \|\bar{\mathbf{a}}\|^2. \tag{8}$$

It can be verified that the smaller the ε, the higher the resolution and the stronger the ability of RCB to suppress an interference that is close to the signal of interest, and that the larger the ε, the more robust RCB will be to tolerate distortions and small-sample-size problems caused by calculating $\hat{\mathbf{R}}$ in (7) from a finite number of data vectors or snapshots. When ε is close to M, RCB will perform like DAS. To attain high resolution and to effectively suppress interference, ε should be made as small as possible. On the other hand, the smaller the sample size N or the larger the distortions, the larger should ε be chosen [19]. Since the performance of RCB does not depend very critically on the choice of ε (as long as it is set to be a "reasonable value") [21], such qualitative guidelines are usually sufficient for making a choice of ε. We will investigate the effect of ε in Section VI. In our examples in Section VI, we choose certain reasonable initial values for ε, and then make some adjustments empirically based on image quality: making it smaller when the resulting images have low resolution, or making it larger when the image is distorted by interferences.

By using the Lagrange multiplier method, the solution to (6) is given by [19]

$$\hat{\mathbf{a}}_0 = \bar{\mathbf{a}} - [\mathbf{I} + \mu \hat{\mathbf{R}}]^{-1} \bar{\mathbf{a}} \tag{9}$$

where $\mathbf{I}$ is the identity matrix, and $\mu \geq 0$ is the corresponding Lagrange multiplier that can be solved from the following equation

$$\|(\mathbf{I} + \mu \hat{\mathbf{R}})^{-1} \bar{\mathbf{a}}\|^2 = \varepsilon. \tag{10}$$

Consider the eigendecomposition on the sample covariance matrix $\hat{\mathbf{R}}$

$$\hat{\mathbf{R}} = \mathbf{U} \boldsymbol{\Gamma} \mathbf{U}^T \tag{11}$$

where the columns of $\mathbf{U}$ are the eigenvectors of $\hat{\mathbf{R}}$ and the diagonal matrix $\boldsymbol{\Gamma}$ consists of the corresponding eigenvalues $\gamma_1 \geq \gamma_2 \geq \cdots \geq \gamma_M$. Let $\mathbf{b} = \mathbf{U}^T \bar{\mathbf{a}}$, where b_m denotes its mth element. Then, (10) can be rewritten as

$$\mathcal{L}(\mu) = \sum_{m=1}^{M} \frac{|b_m|^2}{(1 + \mu \gamma_m)^2} = \varepsilon. \tag{12}$$

Note that $\mathcal{L}(\mu)$ is a monotonically decreasing function of μ, with $\mathcal{L}(0) > \varepsilon$ by (8) and $\lim_{\mu \to \infty} \mathcal{L}(\mu) = 0 < \varepsilon$, which means that μ can be solved efficiently, say, by using the Newton's method

Authorized licensed use limited to: University of Florida. Downloaded on January 29, 2010 at 14:45 from IEEE Xplore. Restrictions apply.

(see [19] for more details). After obtaining the value of μ, the estimate $\hat{\mathbf{a}}_0$ of the actual steering vector $\mathbf{a}_0$ is determined by (9).

Observe that there is a "scaling ambiguity" in (6) by treating both the signal power σ^2 and the steering vector $\mathbf{a}_0$ as unknowns (see [19] and [21]). The ambiguity exists in the sense that $(\sigma^2, \mathbf{a}_0)$ and $(\sigma^2/c, c^{1/2}\mathbf{a}_0)$ (for any constant $c > 0$) yield the same term $\sigma^2\mathbf{a}_0\mathbf{a}_0^T$. To eliminate this ambiguity, we scale the solution $\hat{\mathbf{a}}_0$ to make its norm satisfy the following condition

$$\|\hat{\mathbf{a}}_0\|^2 = M. \tag{13}$$

(Note that $M = \|\bar{\mathbf{a}}\|^2$.)

To obtain an estimate for the signal waveform $s(n)$, we apply a weight vector to the preprocessed signals $\{\mathbf{y}(n)\}_{n=-N}^{N}$. The weight vector is determined by using the estimated steering vector $\hat{\mathbf{a}}_0$ in the weight vector expression of the standard Capon beamformer (see, e.g., [19] and [21])

$$\hat{\mathbf{w}}_{\mathrm{RCB}} = \frac{\|\hat{\mathbf{a}}_0\|}{M^{1/2}} \cdot \frac{\left[\hat{\mathbf{R}} + \frac{1}{\mu}\mathbf{I}\right]^{-1}\bar{\mathbf{a}}_0}{\bar{\mathbf{a}}_0^T\left[\hat{\mathbf{R}} + \frac{1}{\mu}\mathbf{I}\right]^{-1}\hat{\mathbf{R}}\left[\hat{\mathbf{R}} + \frac{1}{\mu}\mathbf{I}\right]^{-1}\bar{\mathbf{a}}_0}. \tag{14}$$

Note that (14) has a diagonal loading form, which allows the sample covariance matrix to be rank-deficient. The beamformer output can be written as

$$\hat{s}_{\mathrm{RCB}}(n) = \hat{\mathbf{w}}_{\mathrm{RCB}}^T\mathbf{y}(n), \quad n = -N, \ldots, N \tag{15}$$

which is the waveform estimate for the acoustic pulse generated at the focal point at location $\mathbf{r}$.

RCB can provide a much better waveform estimate than the conventional DAS but at a higher computational cost. For a single focal point, RCB requires $O(M^3)$ flops, which mainly come from the eigendecomposition of the sample covariance matrix $\hat{\mathbf{R}}$ [19]; DAS needs only $O(M)$ flops. DAS can be used as a fast image reconstruction method to provide initial imaging results.

The weight vector used by DAS for waveform estimation is

$$\hat{\mathbf{w}}_{\mathrm{DAS}} = \bar{\mathbf{a}} \tag{16}$$

and the estimated waveform is given by

$$\hat{s}_{\mathrm{DAS}}(n) = \hat{\mathbf{w}}_{\mathrm{DAS}}^T\mathbf{y}(n) = \sum_{m=1}^{M} y_m(n), \quad n = -N, \ldots, N. \tag{17}$$

IV. Step II of ARMOR: Peak Searching

Based on the estimated waveform obtained in Step I for the focal point at location $\mathbf{r}$, in Step II of ARMOR, we will search for the two peaks of the bipolar acoustic pulse generated by the focal point. In a homogeneous background, where phase distortion is absent, we can accurately calculate the arrival time of the acoustic pulse generated by the focal point at location $\mathbf{r}$ by using (2). However, this is never true in heterogeneous biological tissues. It was reported in [16] that when the heterogeneity is weak, such as in the breast tissue, amplitude distortion caused by multipath is not severe. We can assume that the original peak remains a peak in the waveform estimated from Step I of ARMOR.

The bipolar acoustic pulse has one peak positive and another negative. We determine the positive and negative peak values as follows:

$$P^+ = \max\left\{\max_{n\in[-\Delta,\Delta]}\hat{s}(n)0\right\}, \tag{18}$$

$$P^- = \min\left\{\min_{n\in[-\Delta,\Delta]}\hat{s}(n)0\right\}, \tag{19}$$

where the searching range $[-\Delta, \Delta] \in [-N, N]$ is around the calculated arrival time given by (2). Here Δ is a user parameter. Since the peak searching is independent of the particular waveform estimation methods, we use $\hat{s}(n)$ to denote the waveform estimated by either DAS or ARMOR.

The search range is determined by the difference between the true arrival time $\bar{t}_m$ and the calculated arrival time t_m, based on (2). This arrival time difference has been analyzed for breast tissue by taking into account its relatively weak heterogeneity acoustic property [16]. An expression for this difference is given in [16] by

$$\delta_m(\mathbf{r}') = \bar{t}_m - t_m \propto \frac{[v(\mathbf{r}') - v_0]}{v_0} \tag{20}$$

where $\mathbf{r}'$ is a point within the line connecting the focal point at location $\mathbf{r}$ and the mth transducer at location $\mathbf{r}_m$, and $v(\mathbf{r}')$ is the local sound speed. The higher order terms of $[v(\mathbf{r}') - v_0]/v_0$ in (20) have been ignored. It is reasonable to assume that $v(\mathbf{r}')$ is Gaussian-distributed with mean v_0 and variance σ_v^2. Consequently, the arrival time difference is also Gaussian-distributed with zero-mean and variance $\sigma_\delta^2 \propto \sigma_v^2/v_0^2$. If we choose $\Delta = \sigma_\delta$, and the duration of the acoustic pulse is τ, we can find the two peaks of the pulse within the interval $(-\sigma_\delta, \sigma_\delta + \tau)$ on the recorded signals with a high probability of 0.6826. This analysis is consistent with the experimental measurements in [22]. From our examples, we found that a symmetric range $[-\Delta, \Delta]$ around the estimated arrival time performs similarly to the asymmetric range $[-\Delta, \Delta + \tau]$, and we use the former since it is easy to handle in practice. Also, we can use similar techniques as those in [22] to estimate σ_δ to find a good searching range for Step II of ARMOR, and to estimate τ for the energy-type methods, as shown in our examples later.

There is a tradeoff in choosing the searching range. The larger the searching range, the higher the probability we can find the peaks of the acoustic pulse within the range. However, if the range is chosen too large, the interferences may cause false peaks, and as a consequence, we are more likely to find a false peak. In our examples in Section VI, we choose the best searching range empirically based on the estimated variance of the arrival time difference $\hat{\sigma}_\delta$.

V. Step III of ARMOR: Intensity Calculation

After estimating the waveform generated by the focal point at location $\mathbf{r}$, we need to obtain the response intensity based on the estimated waveform. For the same estimated waveform, different approaches can be used to evaluate the focal point response intensity. These approaches extract different information from

Authorized licensed use limited to: University of Florida. Downloaded on January 29, 2010 at 14:45 from IEEE Xplore. Restrictions apply.

the estimated waveform as the response intensity, and may be useful to physicians in different ways.

There are two major types of response intensity measurement approaches: amplitude-based and energy-based. The waveform peak values obtained in Step II of ARMOR can be used for both approaches.

Conventional DAS uses the amplitude-based measure for TAT imaging [11], [12], with the corresponding response intensity given by $\hat{s}(0)$, or equivalently

$$I_{\mathrm{C}} = \hat{s}(0) = \sum_{m=1}^{M} y_m(0) \tag{21}$$

where the subscript "$_{\mathrm{C}}$" stands for "Conventional."

The energy-based measure, such as the one used in [23], calculates the response intensity as follows

$$I_{\mathrm{E1}} = \hat{s}^2(0) = \left[\sum_{m=1}^{M} y_m(0)\right]^2 \tag{22}$$

where the subscript "$_{\mathrm{E1}}$" means "Energy-type 1."

The entire pulse energy has also been used as an intensity measure, such as in the monostatic and multistatic microwave imaging for breast cancer detection [24], [25], and the intensity is given by

$$I_{\mathrm{E2}} = \sum_{n=0}^{\tau} \hat{s}^2(n) = \sum_{n=0}^{\tau} \left[\sum_{m=1}^{M} y_m(n)\right]^2, \tag{23}$$

where the subscript "$_{\mathrm{E2}}$" stands for "Energy-type 2."

We can consider using the peak value as the response intensity measure due to the bipolar nature of the response at the focal point

$$I_{\mathrm{P}} = \begin{cases} P^+, & \text{if } |P^+| \geq |P^-| \\ P^-, & \text{otherwise} \end{cases} \tag{24}$$

where the subscript "$_{\mathrm{P}}$" stands for "Peak," with P^+ and P^- defined in (18) and (19), respectively. Herein, we keep the sign of the maximum amplitude since the sign of the peak may also contain some information about the focal point.

Peak searching maximizes the output signal-to-noise ratio. An intuitive explanation is that, given the fact that the acoustic pulse is bipolar [11], if we assume that the residual term $\mathbf{e}(t)$ is stationary, or its power is uniform over time, then the signal-to-noise ratio (SNR) is maximized at the (positive or negative) peak of the acoustic pulse. As a comparison, the conventional DAS (21) fixes the samples to be summed up at the calculated arrival time. Due to phase distortions, the waveform at the calculated time may be far from the peak value.

We can also employ peak-to-peak difference as the response intensity for the focal point at location $\mathbf{r}$

$$I_{\mathrm{PP}} = P^+ - P^- \geq 0 \tag{25}$$

where the subscript "$_{\mathrm{PP}}$" denotes the "peak-to-peak difference." Peak-to-peak difference has higher imaging contrast than peak value measure: the peak-to-peak difference of the bipolar pulse is approximately twice the absolute peak value, which means that the output signal power of the former is four times of the latter; yet, the noise power of the former may be only twice that of the latter. Therefore, the output SNR may be doubled by using the peak-to-peak difference rather than the peak value. Both peak-value and peak-to-peak difference measures belong to the amplitude-based measures.

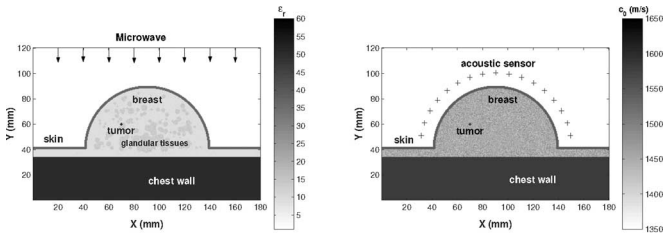

(a) (b)

Fig. 2. 2-D breast model in an x–y coordinate system, with a 2-mm-diameter tumor present. (a) Model for electromagnetic simulation. (b) Model for acoustic simulation.

VI. Numerical and Experimental Examples

We demonstrate the performance of ARMOR using both numerically simulated and experimentally measured TAT data. The ARMOR images are compared with the DAS images.

A. Numerical Examples

We consider a 2-D breast model, as shown in Fig. 2. The 2-D breast model includes 2-mm thick skin, chest wall, as well as randomly distributed fatty breast tissues and glandular tissues. The cross section of the breast model is a half-circle with a 10 cm diameter. In the first numerical example, a 2-mm-diameter tumor is located at 2.2 cm below the skin (at $x = 7.0$ cm, $y = 6.0$ cm). Fig. 2 shows the shape, dielectric properties, and sound speed variations of the breast model, as well as the tumor size and location for the first example. In the second numerical example, one large tumor (1 cm in diameter) is located at $x = 12$ cm, $y = 15$ cm. Other properties of the breast model for the second example are the same as those for the first example.

To reduce the reflections from the skin, the breast model is immersed in a lossless liquid with permittivity similar to that of the breast fatty tissue. Seventeen transducers (assumed omnidirectional) are located on a half-circle 10 mm away from the skin, with uniform spacing, to form a real aperture array.

The dielectric properties of the breast tissues are assumed to be Gaussian random variables with variations of $\pm 10\%$ around their nominal values. This variation represents the upper bound reported in the literature. The nominal values are chosen to be typical of those reported in the literature [5], [26], which is given in Table I [24]. The dielectric constants of glandular tissues are between $\epsilon_r = 11$ and $\epsilon_r = 15$. The dispersive properties of the fatty breast tissue and those of the tumor are also considered in the model. The randomly distributed breast fatty tissues and glandular tissues with variable dielectric properties are representative of the nonhomogeneity of the breast of an actual patient.

Authorized licensed use limited to: University of Florida. Downloaded on January 29, 2010 at 14:45 from IEEE Xplore. Restrictions apply.

TABLE I
ACRONYMS

ART	Adaptive and Robust Methods Of Reconstruction
DAS	Delay-And-Sum
FDTD	Finite Difference Time Domain
PML	Perfectly matched layer
RCB	Robust Capon Beamforming
SNR	Signal-to-Noise Ratio
SAR	Specific Absorption
TAT	Thermoacoustic Tompgraphy
UT	Ultra-sound Tomography
C	Conventional
E1	Energy-type 1
E2	Energy-type 2
P	Peak
PP	Peak-to-Peak difference

Following the report that the breast tissues have a weak acoustic heterogeneity [16], we model the sound speed within the breast as a Gaussian random variable with variation $\pm 5\%$ around the assumed average sound speed of 1500 m/s. Since the attenuation coefficient α in (3) is small for breast tissue (0.75 dB/(MHz·cm)) [15] and the acoustic signals are below 2 MHz, we neglect the exponential attenuation in acoustic wave propagation. Also, since the acoustic pressure field generated by the thermoacoustic effect is usually small [20], we do not consider the nonlinear acoustic effects. The probing microwave pulse used here is a modulated rectangular pulse with a modulating frequency of 800 MHz. The duration of the pulse is 1 μs. More details about the thermal acoustic simulations are given in the Appendix. In the following, all the images are displayed on a linear scale, and we will name the imaging methods by their waveform estimation method followed by the intensity calculation approach, such as "DAS-C."

Note that the skin also absorbs microwave energy and generates acoustic signals. The skin response is much stronger than that of the tumor, since the skin has a much larger area than the tumor and the skin is closer to the acoustic sensors. So, before applying the aforementioned preprocessing steps and ARMOR, we remove the strong skin response using techniques similar to those in [24]. A calibration signal is obtained as the average of the recorded signals containing similar skin response. Then, the calibration signal is subtracted out from all recorded signals to remove the skin response as much as possible.

The searching range is chosen by the guidelines presented in Section IV. To obtain a general profile of the arrival time difference caused by the phase distortion, we use a simple method similar to the one used in [27]. First, the cross-correlation functions for all the signals recorded by the two adjacent transducers are obtained. The peak value of the cross-correlation function is used to estimate the arrival time delay between the signals recorded by the adjacent transducers. Second, these arrival time delays are fitted using a fourth-order polynomial curve, which is dominated by the arrival time delays due to the path length differences in the absent of phase distortions. The fourth-order polynomial is used since the delay caused by the path length difference should vary smoothly [27]. Fig. 3(a) shows the estimated arrival time delay and the delay based on curve fitting.

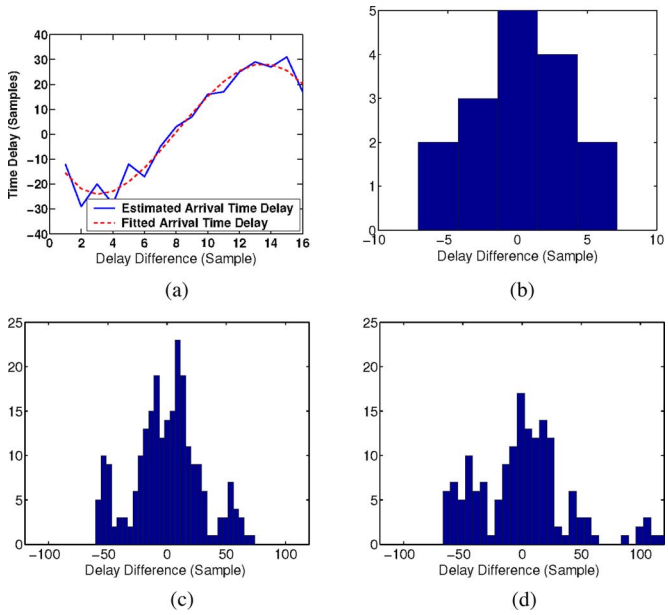

Fig. 3. (a) Comparison between the estimated and fitted arrival time delays, for the simulated breast model with one tumor (the curves for the two-tumor case are similar). Histograms of delay differences. (b) Simulated breast model with one tumor. (c) Breast specimen I. (d) Breast specimen II.

Third, the delay difference between the estimated arrival time delay and the fitted delay, or the fitting error, is treated as the arrival time distortion for the transducers. The standard deviation of the delay difference is used to estimate σ_δ. Although the accuracy of the cross-correlation method is limited due to false peaks and jitter problems, it is sufficient to obtain a qualitative profile for σ_δ.

Fig. 3 gives the histogram of the delay difference for all the cases that we considered herein. For the simulated example, the standard deviation of the delay difference is 4.5, which indicates a weak phase distortion in the breast model. We set an initial value for Δ, based on the estimated $\hat{\sigma}_\delta$, and adjust the length of the searching range to achieve the best imaging result.

To estimate the pulse duration $\hat{\tau}$ (used in DAS-E2 and RCB-E2), we select several typical signals (with clear peaks) and take the average of their pulse durations. In practice, the acoustic pulse duration is determined by the probing pulse duration, size and shape of the tumor, as well as the transducer response.

Fig. 4 shows the images for the simulated breast model with one 2-mm diameter tumor formed using ARMOR and DAS. The tumor response is weak for such a small tumor. In these images, we use $\varepsilon = 0.1M$ and the searching range $[-14, 14]$. Fig. 4(a) corresponds to DAS-C, where the tumor is buried by interference and noise. In Fig. 4(b), DAS-E1 fails to detect the tumor. In Fig. 4(c), for DAS-E2, a shadow of the tumor can be seen. In Fig. 4(d), for RCB-E2, most of the clutters are cleared up but a strong clutter shows up near the chest wall. Fig. 4(e)–4(h) shows the results of peak searching; none of them have false tumors, which may be attributed to proper corrections of phase aberrations. Images produced by ARMOR-P in Fig. 4(f)

Authorized licensed use limited to: University of Florida. Downloaded on January 29, 2010 at 14:45 from IEEE Xplore. Restrictions apply.

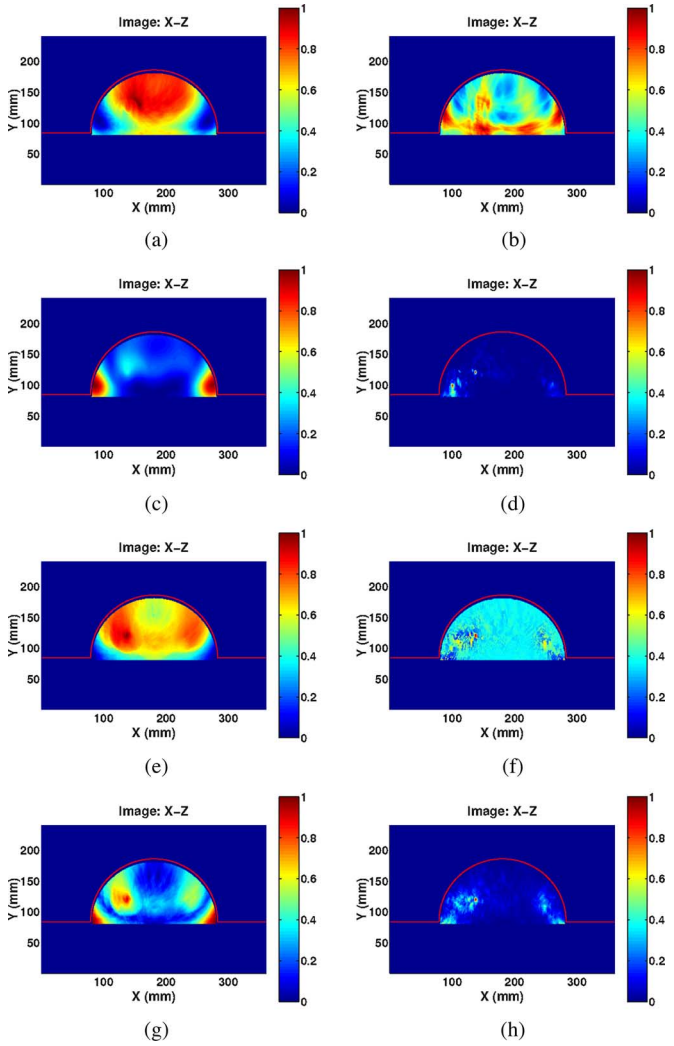

Fig. 4. Reconstructed images based on the 2-D simulated breast model with one 2-mm-diameter tumor. (a) DAS-C. (b) DAS-E1. (c) DAS-E2. (d) RCB-E2, with $\varepsilon = 0.1M$. (e) DAS-P. (f) ARMOR-P, with $\varepsilon = 0.1M$. (g) DAS-PP. (h) ARMOR-PP, with $\varepsilon = 0.1M$.

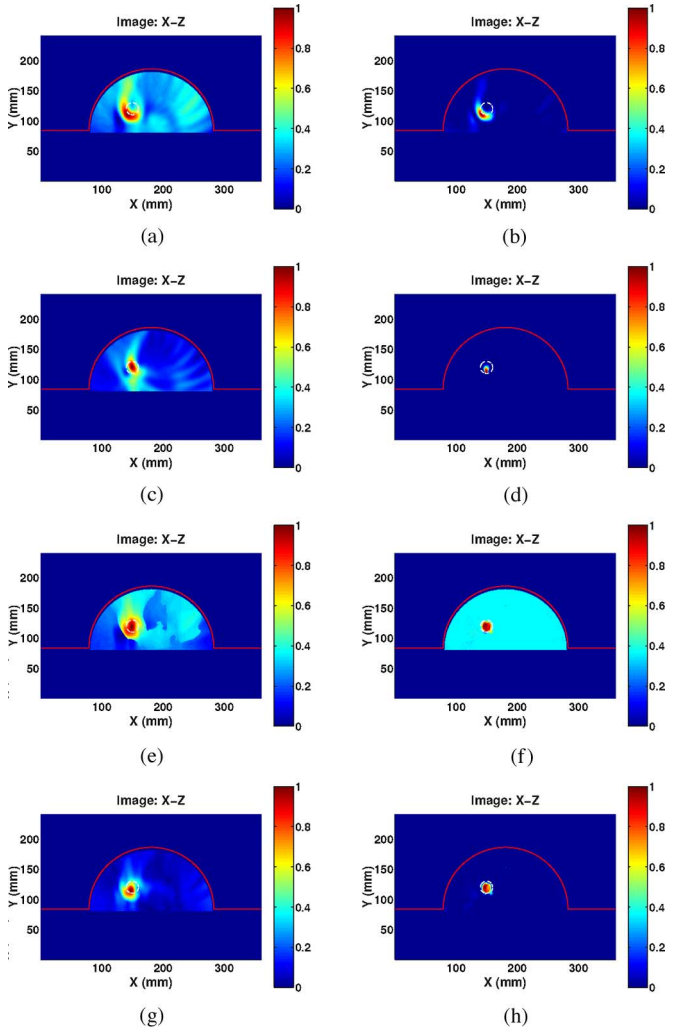

Fig. 5. Reconstructed images based on the 2-D simulated breast model with one large tumor (1 cm in diameter). The white circle in the image corresponds to the actual shape of the tumor. (a) DAS-C. (b) DAS-E1. (c) DAS-E2. (d) RCB-E2, with $\varepsilon = 0.1M$. (e) DAS-P. (f) ARMOR-P, with $\varepsilon = 0.1M$. (g) DAS-PP. (h) ARMOR-PP, with $\varepsilon = 0.1M$.

and by ARMOR-PP in Fig. 4(h) have lower sidelobe levels and higher resolutions, and the latter has a higher contrast than the former, due to the latter using the peak-to-peak difference as the intensity measure.

Fig. 5 shows the imaging results for the one large tumor (1 cm diameter) case. Here, we set $\varepsilon = 0.1M$ and the searching range $[-20, 20]$. (Note that different tumor sizes and locations will result in different sound speed variations in the breast model.) The white circle in the image corresponds to the actual contour of the tumor. Although all the methods can detect the tumor, only ARMOR can be used to form an image of the tumor with the best agreement with the actual tumor size and location.

By plotting a map (maps are not shown here due to limited space) of the values of μ used in ARMOR, for each focal point, we find that at the tumor locations, μ usually takes smaller values than that at other locations.

B. Experimental Results

We have also tested ARMOR and DAS on two sets of TAT experimental data from mastectomy specimens [4] obtained by the Optical Imaging Laboratory at the Texas A&M University.

The two data sets were acquired from mastectomy specimens using a TAT system. Microwave sources were used to heat the specimens transiently. In the experiment, the breast specimen was formed to a cylindrical shape inside a plastic bowl. The bowl was immersed in ultrasound coupling medium in a container. For breast specimen I, the acoustic signals were recorded at 240 equally spaced scanning stops on a circular track of radius 12.9 cm. The thickness of this specimen was about 4 cm in a round plastic bowl of 17 cm in diameter. This lesion was diagnosed as an invasive metaplastic carcinoma with chondroid and squamous metaplasia. The size of the tumor was measured to be 35 mm in diameter by TAT, and 36 mm in diameter by radiography (see [4] for details). For breast specimen II, the scanning radius was 9.7 cm, with 160 scanning stops. This specimen was

Authorized licensed use limited to: University of Florida. Downloaded on January 29, 2010 at 14:45 from IEEE Xplore. Restrictions apply.

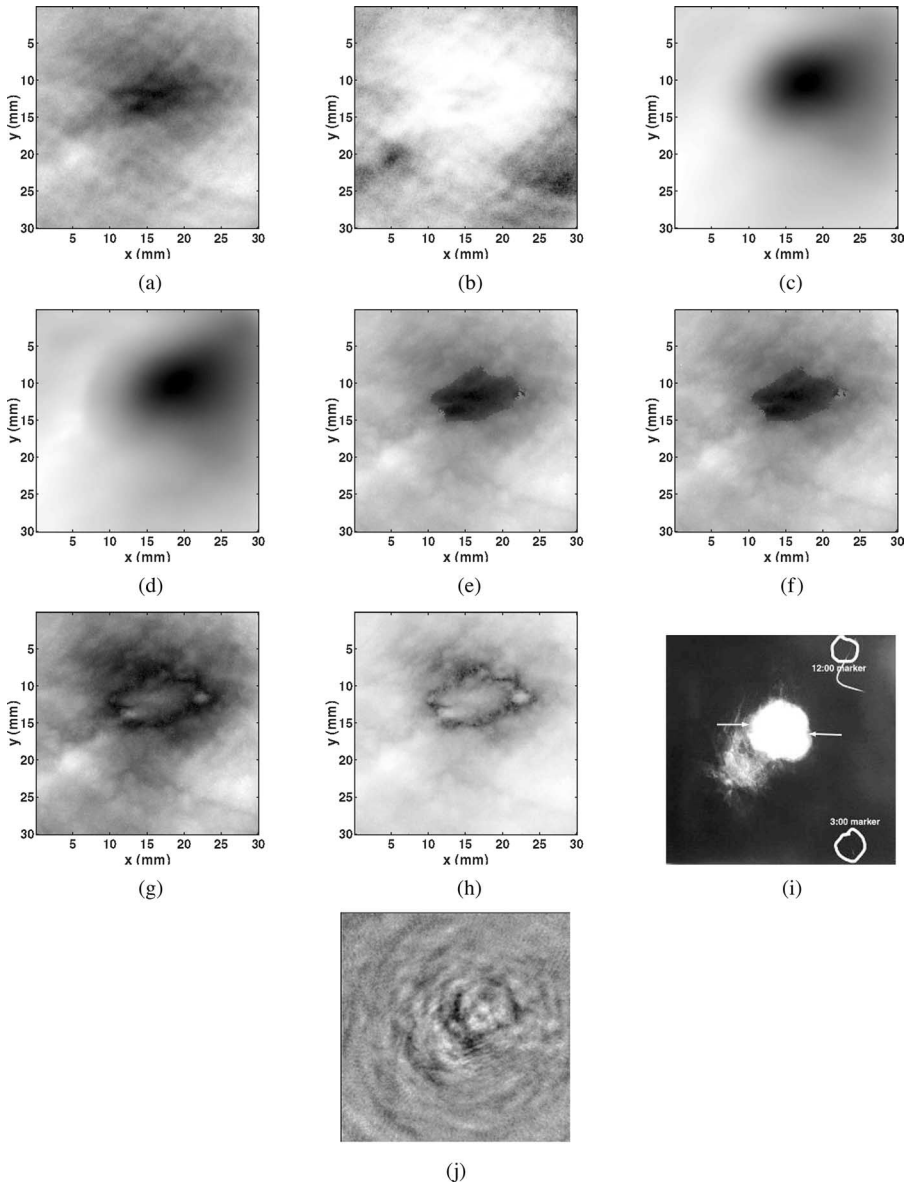

Fig. 6. Reconstructed images for breast specimen I. (a) DAS-C. (b) DAS-E1. (c) DAS-E2. (d) RCB-E2, with $\varepsilon = 0.5M$. (e) DAS-P. (f) ARMOR-P, with $\varepsilon = 0.5M$. (g) DAS-PP. (h) ARMOR-PP, with $\varepsilon = 0.5M$. (i) X-ray image. (j) Inverse solution.

9 cm thick in a round plastic bowl of 11 cm in diameter. The lesion in the specimen was diagnosed as infiltrating lobular carcinoma; the size of the tumor was about 20 mm $\times$ 12 mm on TAT image, and about 26 mm $\times$ 15 mm on the radiography (see [4] for more details).

First, we study the delay difference for both the breast specimens to get a qualitative guide for choosing the searching range in Step II of ARMOR. The results are shown in Fig. 3(c) and 3(d), respectively. Note that breast specimen II has a larger variance in delay differences than breast specimen I. In Fig. 3(c), 70% of the delay differences are roughly between -23 to 23 samples, whereas in Fig. 3(d), 70% of the delay differences are between -40 and 40 samples. Therefore we should set a larger searching range for breast specimen II than for breast specimen I.

Fig. 6 shows the reconstructed images for breast specimen I. In the following images, the searching range was set to $[-3, 3]$ after adjustment, and $\varepsilon = 0.5M$ for all the RCBs used herein. In Fig. 6(a), for DAS-C, the dark region shows a blurred object corresponding to the breast tumor. In Fig. 6(b), for DAS-E1, the light region shows a vague boundary of the tumor. Fig. 6(c), for DAS-E2, and 6(d), for RCB-E2, have similar performances. In Fig. 6(e), for DAS-P, and 6(f), for ARMOR-P, a dark region with a clear cut has a good correspondence with the location and shape of the tumor in the radiograph [4]. In Fig. 6(g), for DAS-PP, and 6(h), for ARMOR-PP, not only a clear image of the tumor is obtained, but also the detailed boundary is revealed. For comparison, the images from X-ray mammography, considered the "gold standard" of breast imaging, and the exact inverse solution of TAT (see [4] for more details) are shown in Fig. 6(i)

Authorized licensed use limited to: University of Florida. Downloaded on January 29, 2010 at 14:45 from IEEE Xplore. Restrictions apply.

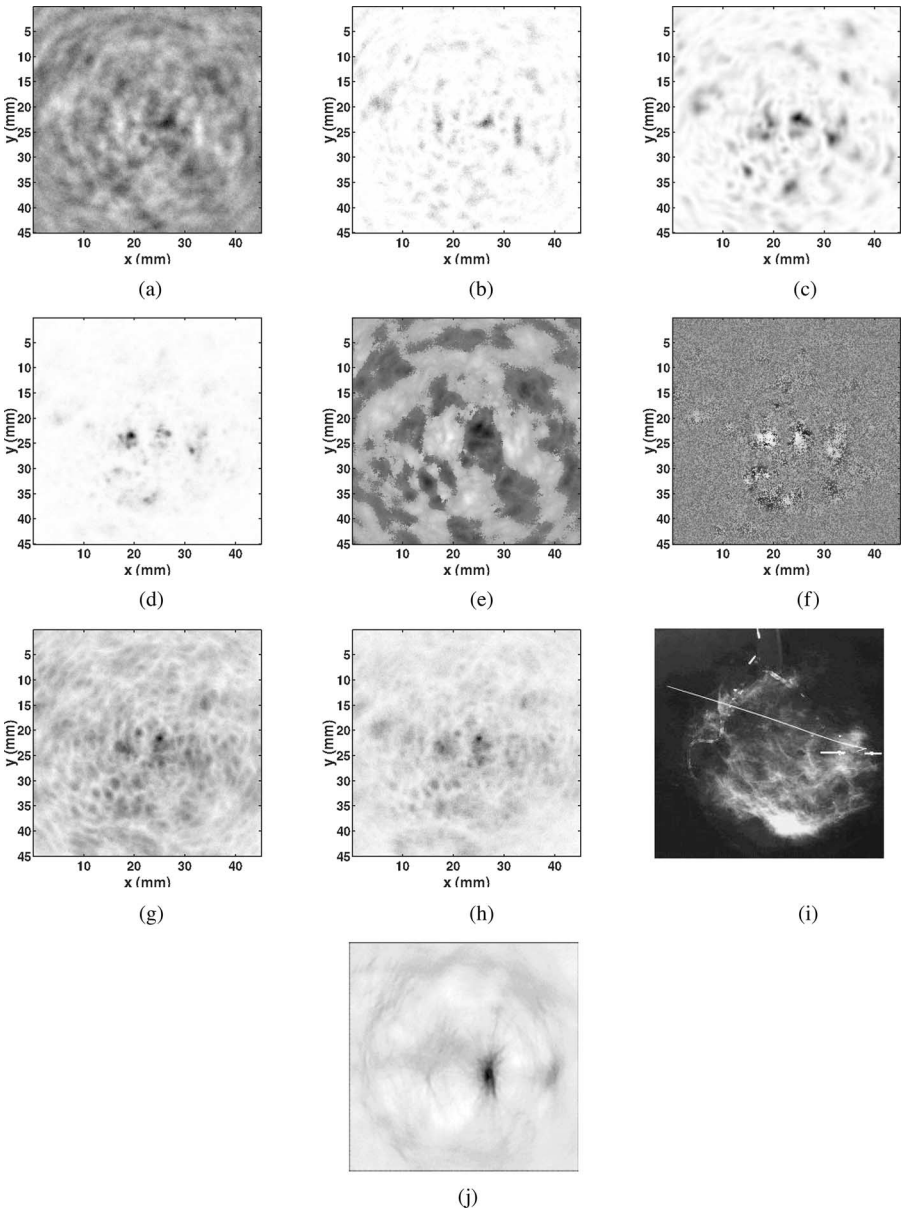

Fig. 7. Reconstructed images for breast specimen II. (a) DAS-C. (b) DAS-E1. (c) DAS-E2. (d) RCB-E2, with $\varepsilon = 0.5M$. (e) DAS-P. (f) ARMOR-P, with $\varepsilon = 0.5M$. (g) DAS-PP. (h) ARMOR-PP, with $\varepsilon = 0.5M$. (i) X-ray image. (j) Inverse solution.

and 6(j), respectively. We give Fig. 6 and the following Fig. 7 in gray scale to have a better comparison with the X-ray images.

Fig. 7 shows the reconstructed images for breast specimen II. The tumor size here is smaller, and a high level of interference and noise is present in the recorded data. The searching interval is eventually adjusted to $[-120, 120]$ and RCB parameter $\varepsilon = 0.5M$. In Fig. 7(a), for DAS-C, the true tumor is barely identifiable from the surrounding clutters. The DAS-E1 shown in Fig. 7(b) and the DAS-E2 shown in Fig. 7(c) provide higher imaging contrast than DAS-C but show strong clutter. In Fig. 7(d), for RCB-E2, a false tumor shows up, which demonstrates the need for robustness in the presence of relatively strong phase distortion. DAS-P is shown in Fig. 7(e) and ARMOR-P is shown in Fig. 7(f). DAS-PP and ARMOR-PP produce the best images in Figs. 7(g) and 7(h), respectively, with the location and shape of the tumor consistent with the radiograph in Fig. 7(i) [4]. If we define the signal-to-background ratio (SBR) (i.e., squaring the pixel values of the image, the ratio of the maximum to the total sum of the squared values) as an image quality measurement metric, ARMOR-PP has an SBR twice that of DAS-PP, which means a 3 dB gain for ARMOR-PP. For comparison, the image formed by the exact inverse solution of TAT (see [4] for more details) is shown in Fig. 7(j).

The effects of the uncertainty parameter ε in ARMOR is studied in our next example. We vary ε of RCB used in ARMOR. The imaging results for breast specimen I, shown in Fig. 8, are consistent with our previous analysis: when ε is large, the performance of RCB, in Fig. 8(a), is close to that of DAS in Fig. 6(g). When the parameter ε is small, as shown in Fig. 8(c), the resolution is improved at the cost of robustness.

Authorized licensed use limited to: University of Florida. Downloaded on January 29, 2010 at 14:45 from IEEE Xplore. Restrictions apply.

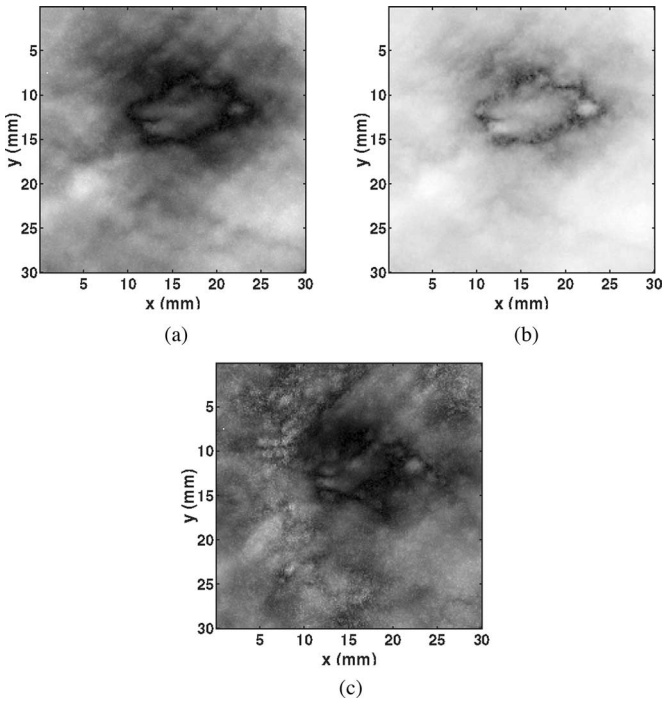

Fig. 8. Effects of uncertainty parameter ε on ARMOR-PP, with a searching range $[-3, 3]$. (a) $\varepsilon = 0.7M$. (b) $\varepsilon = 0.5M$. (c) $\varepsilon = 0.3M$.

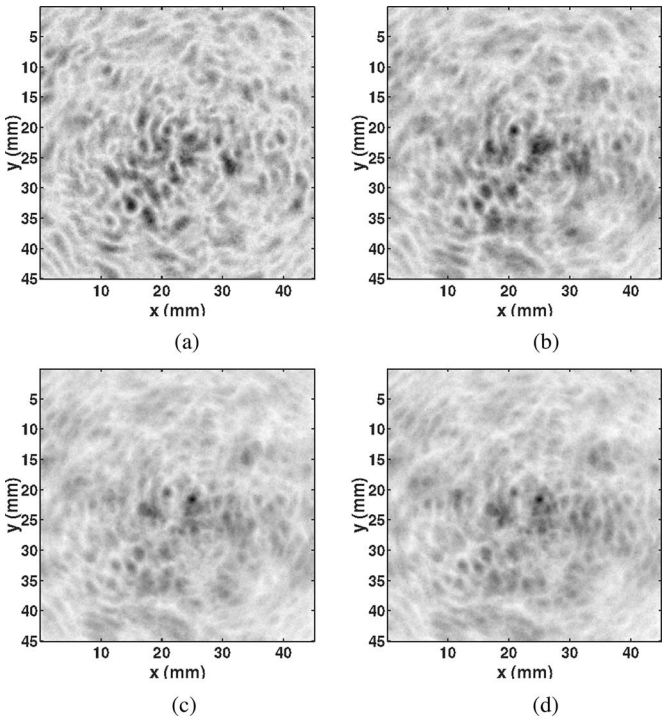

Fig. 9. Effects of the searching range on the DAS-PP images. (a) Searching range $[-20, 20]$. (b) Searching range: $[-40, 40]$. (c) Searching range $[-60, 60]$. (d) Searching range: $[-80, 80]$.

In our last example, the effect of the searching-range width on the imaging quality is considered. We use DAS-PP as an example since it shows more dependence on the searching range. The conclusion drawn for DAS applies to ARMOR. A symmetric searching range centered around the calculated arrival time is used. From the discussions in Section IV, we know that there is a tradeoff in choosing the searching range. Clearly, when the searching range is too small, such as in Fig. 9(a), we miss the true peaks. With an increase in the searching range, the image quality becomes gradually better, as shown in Fig. 9(b) and 9(c). However, when the searching range passes a certain threshold, with too much interference coming into the searching range, the image quality degrades because of increased clutters, as shown in Fig. 9(d).

From our numerical examples, we conclude that ARMOR has higher resolution and better interference rejection capability and more robustness against wavefront distortion than DAS. Also, we find that the amplitude-based measures reveal more details of the tumor in the reconstructed images than their energy-based counterparts. The energy-based measures are not sensitive to phase distortions; however, they tend to blur the reconstructed images, causing loss of details with a low-pass filtering-like effect.

VII. Conclusion

ARMOR has been proposed for thermoacoustic tomography. ARMOR is robust to the amplitude and phase distortions in the recorded signals caused by the acoustic heterogeneity of biological tissues. ARMOR consists of three steps: in the first step, ARMOR uses the data-adaptive robust Capon beamforming (RCB) for waveform estimation; in the second step of ARMOR, a simple, yet effective, peak searching method is used to mitigate the phase distortion in the estimated waveform; in the third step, the response intensity is calculated for the focal point using various approaches, among which the peak-to-peak difference measure further enhances the image contrast. Examples based on a numerically simulated 2-D breast model and two sets of experimentally measured data from human mastectomy specimens demonstrate the excellent performance of ARMOR: high-resolution, low sidelobe level, and much improved interference suppression capability.

Appendix

Thermal Acoustic Simulations

We consider the microwave-induced thermal acoustic simulation in two steps. In the first step, the electromagnetic field inside the breast model is simulated and the specific absorption rate (SAR) distribution is calculated based on the simulated electromagnetic field. The second step is for the acoustic wave simulation, where the SAR distribution obtained in the first step is used as the acoustic pressure source through the thermal expansion coefficient. In both steps, the finite-difference time-domain (FDTD) method [28] is used for the simulation examples.

The 2-D electromagnetic breast model used is as shown in Fig. 2(a). A narrow electromagnetic pulse is used to irradiate the breast from the top of the model. The electromagnetic field is simulated using the FDTD method. The grid-cell size used by FDTD is 0.5 mm $\times$ 0.5 mm and the computational region is terminated by perfectly matched layer (PML) absorbing boundary conditions [29].

Authorized licensed use limited to: University of Florida. Downloaded on January 29, 2010 at 14:45 from IEEE Xplore. Restrictions apply.

TABLE II
NOMINAL DIELECTRIC PROPERTIES OF BREAST TISSUES [24]

Tissues	Dielectric Properties	
	Permittivity (F/m)	Conductivity (S/m)
Immersion Liquid	9	0
Chest Wall	50	7
Skin	36	4
Fatty Breast Tissue	9	0.4
Nipple	45	5
Glandular Tissue	11-15	0.4-0.5
Tumor	50	4

TABLE III
ACOUSTIC PARAMETERS FOR BIOLOGICAL TISSUES

Tissue	ρ (kg/m^3)	c (m/s)	α^* (dB/cm)	β (1/° C)	C_p (J/(° C · kg))
Breast	1020	1510	$0.75f^{1.5}$	3E-4	3550
Skin	1100	1537	3.5	3E-4	3500
Muscle	1041	1580	$0.57f$	3E-4	3510
Tumor	1041	1580	$0.57f$	3E-4	3510

* f is the acoustic frequency, and the unit is in megahertz.

The SAR distribution is given as [30]

$$\mathrm{SAR}(\mathbf{r}) = \frac{\sigma(\mathbf{r})E^2(\mathbf{r})}{2\rho(\mathbf{r})} \tag{26}$$

where $\sigma(\mathbf{r})$ is the conductivity of the biological tissues at location $\mathbf{r}$, $E(\mathbf{r})$ is the electric field at location $\mathbf{r}$, and $\rho(\mathbf{r})$ is the mass density of the biological tissues at location $\mathbf{r}$.

In the microwave-induced TAI system, the microwave energy is small, and as a result, the acoustic pressure field induced by the microwave is also small. So, the nonlinear acoustic effect does not need to be considered in the TAI system. The two basic linear acoustic wave generation equations are [9]

$$\rho\frac{\partial}{\partial t}\mathbf{u}(\mathbf{r},t) = -\nabla p(\mathbf{r},t) \tag{27}$$

and

$$\nabla\cdot\mathbf{u}(\mathbf{r},t) = -\frac{1}{\rho c^2}\frac{\partial}{\partial t}p(\mathbf{r},t) + \alpha p(\mathbf{r},t) + \beta\frac{\partial}{\partial t}T(\mathbf{r},t) \tag{28}$$

where $\mathbf{u}(\mathbf{r},t)$ is the acoustic velocity vector, $p(\mathbf{r},t)$ is the acoustic pressure field, ρ is the mass density, α is the attenuation coefficient, β is the thermal expansion coefficient, and $T(\mathbf{r},t)$ is the temperature. The values for these acoustic properties for different breast tissues are listed in Table III [25].

Because the duration of the microwave pulse is much shorter than the thermal diffusion time, thermal diffusion can be neglected [9], and the thermal equation is

$$C_p\frac{\partial}{\partial t}T(\mathbf{r},t) = \mathrm{SAR}(\mathbf{r},t) \tag{29}$$

where C_p is the specific heat. Substituting (29) into (28) gives

$$\nabla\cdot\mathbf{u}(\mathbf{r},t) = -\frac{1}{\rho c^2}\frac{\partial}{\partial t}p(\mathbf{r},t) + \alpha p(\mathbf{r},t) + \frac{\beta}{C_p}\mathrm{SAR}(\mathbf{r},t). \tag{30}$$

FDTD is used again to compute the thermal acoustic wave based on (27) and (30).

The breast model for the acoustic simulation is shown in Fig. 2(b), which is constructed similarly to the model for electromagnetic simulation. An acoustic sensor array deployed uniformly around the breast model is used to record the thermal acoustic signals. The grid-cell size used by the acoustic FDTD is 0.1 mm × 0.1 mm and the computational region is terminated by PML-absorbing boundary conditions. Note that the size of the FDTD cell for the acoustic simulation is much finer than that of the FDTD cell for the electromagnetic simulation because the wavelength of an acoustic wave is much smaller than that of a microwave. The SAR distribution data is interpolated to achieve a desired grid resolution for the acoustic breast model.

REFERENCES

[1] R. G. Olsen and J. C. Lin, "Acoustic imaging of a model of a human hand using pulsed microwave irradiation," *Bioelectromagnetics*, vol. 4, pp. 397–400, 1983.

[2] R. A. Kruger, P. Liu, Y. R. Fang, and C. R. Appledorn, "Photoacoustic ultrasound (PAUS)—reconstruction tomography," *Med. Phys.*, vol. 22, pp. 1605–1609, Oct. 1995.

[3] R. A. Kruger, K. D. Miller, H. E. Reynolds, W. L. Kiser, D. R. Reinecke, and G. A. Kruger, "Breast cancer *in vivo*: Contrast enhancement with thermoacoustic CT at 434 MHz—feasibility study," *Radiology*, vol. 216, pp. 279–283, 2000.

[4] G. Ku, B. D. Fornage, X. Jin, M. Xu, K. K. Hunt, and L. V. Wang, "Thermoacoustic and photoacoustic tomography of thick biological tissues toward breast imaging," *Technol. Cancer Res. Treat.*, vol. 4, pp. 1–7, Oct. 2005.

[5] S. S. Chaudhary, R. K. Mishra, A. Swarup, and J. M. Thomas, "Dielectric properties of normal and malignant human breast tissues at radiowave and microwave frequencies," *Indian J. Biochem. Biophys.*, vol. 21, pp. 76–79, Feb. 1984.

[6] M. A. Anastasio, J. Zhang, X. Pan, Y. Zou, G. Ku, and L. V. Wang, "Half-time image reconstruction in thermoacoustic tomography," *IEEE Trans. Med. Imag.*, vol. 24, no. 2, pp. 199–210, Feb. 2005.

[7] Y. Xu, D. Feng, and L. V. Wang, "Exact frequency-domain reconstruction for thermoacoustic tomography: I. Planar geometry," *IEEE Trans. Med. Imag.*, vol. 21, no. 7, pp. 823–828, Jul. 2002.

[8] Y. Xu, M. Xu, and L. V. Wang, "Exact frequency-domain reconstruction for thermoacoustic tomography: II. Cylindrical geometry," *IEEE Trans. Med. Imag.*, vol. 21, no. 7, pp. 829–833, Jul. 2002.

[9] M. Xu and L. V. Wang, "Time-domain reconstruction for thermoacoustic tomography in a spherical geometry," *IEEE Trans. Med. Imag.*, vol. 21, no. 7, pp. 814–822, Jul. 2002.

[10] M. Xu, Y. Xu, and L. V. Wang, "Time-domain reconstruction algorithms and numerical simulations for thermoacoustic tomography in various geometries," *IEEE Trans. Biomed. Eng.*, vol. 50, no. 9, pp. 1086–1099, Sep. 2003.

[11] C. G. A. Hoelen and F. F. M. de Mul, "Image reconstruction for photoacoustic scanning of tissue structures," *Appl. Opt.*, vol. 39, no. 31, pp. 5872–5883, 2000.

[12] D. Feng, Y. Xu, G. Ku, and L. V. Wang, "Microwave-induced thermoacoustic tomography: Reconstruction by synthetic aperture," *Med. Phys.*, vol. 28, pp. 2427–2431, Dec. 2001.

[13] Y. V. Zhulina, "Optimal statistical approach to optoacoustic image reconstruction," *Appl. Opt.*, vol. 39, no. 32, pp. 5971–5977, 2000.

[14] G. Kossoff, E. K. Fry, and J. Jellins, "Average velocity of ultrasound in the human female breast," *J. Acoust. Soc. Amer.*, vol. 53, no. 6, pp. 1730–1736, 1973.

[15] T. Szabo, *Diagnostic Ultrasound Imaging: Inside Out.* New York: Academic, Sep. 2004.

[16] Y. Xu and L. V. Wang, "Effects of acoustic heterogeneity in breast thermoacoustic tomography," *IEEE. Trans. Ultrason., Ferroelect. Freq. Control*, vol. 50, no. 9, pp. 1134–1146, Sep. 2003.

[17] D. Liu and R. C. Waag, "Time-shift compensation of ultrasonic pulse focus degradation using least-mean-square error estimates of arrival time," *J. Acoust. Soc. Amer.*, vol. 95, pp. 542–555, Jan. 1994.

[18] Q. Zhu and B. D. Steinberg, "Deaberration of incoherent wavefront distortion: An approach toward inverse filtering," *IEEE Trans. Ultrason., Ferroelect, Freq. Control*, vol. 44, no. 3, pp. 575–589, May 1997.

[19] J. Li, P. Stoica, and Z. Wang, "On robust Capon beamforming and diagonal loading," *IEEE Trans. Signal Process*, vol. 51, no. 7, pp. 1702–1715, Jul. 2003.

Authorized licensed use limited to: University of Florida. Downloaded on January 29, 2010 at 14:45 from IEEE Xplore. Restrictions apply.

[20] M. Xu and L. V. Wang, "Pulsed-microwave-induced thermoacoustic tomography: Filtered backprojection in a circular measurement configuration," *Med. Phys.*, vol. 29, no. 8, pp. 1661–1669, 2002.
[21] J. Li and P. Stoica, Eds., *Robust Adaptive Beamforming.* New York: Wiley, 2005.
[22] Q. Zhu and B. D. Steinberg, "Wavefront amplitude distribution in the female breast," *J. Acoust. Soc. Amer.*, vol. 96, pp. 1–9, Jul. 1994.
[23] X. Li and S. C. Hagness, "A confocal microwave imaging algorithm for breast cancer detection," *IEEE Microw. Wireless Compon. Lett.*, vol. 11, no. 3, pp. 130–132, Mar. 2001.
[24] B. Guo, Y. Wang, J. Li, P. Stoica, and R. Wu, "Microwave imaging via adaptive beamforming methods for breast cancer detection," *J. Electromagn. Waves Appl.*, vol. 20, no. 1, pp. 53–63, 2006.
[25] E. J. Bond, X. Li, S. C. Hagness, and B. D. Van Veen, "Microwave imaging via space–time beamforming for early detection of breast cancer," *IEEE Trans. Antennas Propag.*, vol. 51, no. 8, pp. 1690–1705, Aug. 2003.
[26] C. Gabriel, R. W. Lau, and S. Gabriel, "The dielectric properties of biological tissues: II. Measured in the frequency range 10 Hz to 20 GHz," *Phys. Med. Biol.*, vol. 41, pp. 2251–2269, Nov. 1996.
[27] Y. Sumino and R. Waag, "Measurements of ultrasonic pulse arrival time differences produced by abdominal wall specimens," *J. Acoust. Soc. Am.*, vol. 90, pp. 2924–2930, Dec. 1991.
[28] A. Taflove and S. C. Hagness, *Computational Electrodynamics: The Finite-Difference Time-Domain Method*, 3rd ed. Boston, MA: Artech House, Jul. 2005.
[29] S. D. Gedney, "An anisotropic perfectly matched layer-absorbing medium for the truncation of FDTD lattices," *IEEE Trans. Antennas Propag.*, vol. 44, no. 12, pp. 1630–1639, Dec. 1996.
[30] P. Bernardi, M. Cavagnaro, S. Pisa, and E. Piuzzi, "SAR distribution and temperature increase in an anatomical model of the human eye exposed to the field radiated by the user antenna in a wireless LAN," *IEEE Trans. Microw. Theory Tech.*, vol. 46, no. 12, pp. 2074–2082, Dec. 1998.

Yao Xie (S'04) received the B.Sc. degree from the University of Science and Technology of China (USTC), Hefei, China, in 2004, and the M.Sc. degree from the University of Florida, Gainesville, in 2006, both in electrical engineering. She is currently working toward the Ph.D. degree at the Department of Electrical Engineering, Stanford University, Stanford, CA.

Her current research interests include optimization, information theory, and their applications in wireless communications, signal processing, and medical imaging.

Ms. Xie is a member of Tau Beta Pi and Etta Kappa Nu. She was the first-place winner in the Student Best Paper Contest at the 2005 Annual Asilomar Conference on Signals, Systems, and Computers, for her work on breast cancer detection.

Bin Guo (S'05–M'07) received the B.E. and M.S. degrees in electrical engineering from Xian Jiaotong University, Xian, China, in 1997 and 2000, respectively, and the Ph.D. degree from the Department of Electrical and Computer Engineering, University of Florida, Gainesville, in 2007.

Currently, he is a Research Associate in the Department of Electrical and computer Engineering, Duke University, Durham, NC. Prior to joining Duke University, he was a Research Assistant with the Department of Electrical and Computer Engineering, University of Florida, from 2003 to 2007, and was an Associate Research Scientist with the Temasek Laboratories, National University of Singapore, Singapore, from 2002 to 2003. His current research interests include signal processing, microwave imaging, and computational electromagnetics.

Jian Li (S'87–M'91–SM'97–F'05) received the M.Sc. and Ph.D. degrees in electrical engineering from Ohio State University, Columbus, in 1987 and 1991, respectively.

From April 1991 to June 1991, she was an Adjunct Assistant Professor with the Department of Electrical Engineering, Ohio State University. From July 1991 to June 1993, she was an Assistant Professor with the Department of Electrical Engineering, University of Kentucky, Lexington. Since August 1993, she has been with the Department of Electrical and Computer Engineering, University of Florida, Gainesville, where she is currently a Professor. Her current research interests include spectral estimation, statistical and array signal processing, and their applications.

Prof. Li is a Fellow of the Institution of Engineering and Technology (IET). She is a member of Sigma Xi and Phi Kappa Phi. She received the 1994 National Science Foundation Young Investigator Award and the 1996 Office of Naval Research Young Investigator Award. She is presently a member of two of the IEEE Signal Processing Society technical committees: the Signal Processing Theory and Methods (SPTM) Technical Committee and the Sensor Array and Multichannel (SAM) Technical Committee. She was an Executive Committee Member of the 2002 International Conference on Acoustics, Speech, and Signal Processing, Orlando, FL, in May 2002. She was an Associate Editor of the IEEE TRANSACTIONS ON SIGNAL PROCESSING from 1999 to 2005, an Associate Editor of the IEEE SIGNAL PROCESSING MAGAZINE from 2003 to 2005, and a member of the Editorial Board of *Signal Processing*, a publication of the European Association for Signal Processing (EURASIP), from 2005 to 2007. She has been a Member of the Editorial Board of *Digital Signal Processing—A Review Journal*, a publication of Elsevier, since 2006. She is a coauthor of the papers that have received the First- and Second-Place Best Student Paper Award, respectively, at the 2005 and 2007 Annual Asilomar Conferences on Signals, Systems, and Computers in Pacific Grove, CA. She is also a coauthor of the paper that has received the M. Barry Carlton Award for the best paper published in IEEE TRANSACTIONS ON AEROSPACE AND ELECTRONIC SYSTEMS in 2005.

Geng Ku received the B.S. and M.S. degrees from Huazhong University of Science and Technology, Wuhan, China, and the Ph.D. degree from the Department of Biomedical Engineering, Texas A&M University, College Station.

He is a Research Faculty Member in the Department of Biomedical Engineering, Washington University at St. Louis, St. Louis. His current research interests include laser-based photoacoustic tomography and microwave-based thermoacoustic tomography.

Lihong V. Wang (M'96–SM'00–F'06) received the Ph.D. degree from Rice University, Houston, TX, under the tutelage of Dr. Robert Curl, Dr. Richard Smalley, and Dr. Frank Tittel.

He holds the Gene K. Beare Distinguished Professorship in the Department of Biomedical Engineering, Washington University at St. Louis, St. Louis, and directs the Optical Imaging Laboratory. He invented or discovered frequency-swept ultrasound-modulated optical tomography, dark-field confocal photoacoustic microscopy, photoacoustic Doppler sensing, photoacoustic reporter gene imaging, focused scanning microwave-induced thermoacoustic tomography, exact reconstruction algorithms for photoacoustic or thermoacoustic tomography, sonoluminescence tomography, Mueller-matrix optical coherence tomography, and oblique-incidence reflectometry. His Monte Carlo model of photon transport in scattering media is used worldwide as a standard tool. He authored more than 137 peer-reviewed journal articles, and one of the first textbooks in biophotonics entitled *Biomedical Optics Principles and Imaging* (Wiley, 2007).

Prof. Wang is a Fellow of the American Institute for Medical and Biomedical Engineering (AIMBE), The Optical Society of America (OSA), and The International Society for Optical Engineering (SPIE). He serves on the editorial boards of the *Journal of Biomedical Optics* and *Applied Optics*. He is the Chair of the International Biomedical Optics Society. He was the recipient of the National Institutes of Health (NIH) FIRST award, the National Science Foundation (NSF) CAREER award, and the Outstanding Young Scientist Award sponsored by Johnson & Johnson Medical and the Houston Society for Engineering in Medicine and Biology.

Authorized licensed use limited to: University of Florida. Downloaded on January 29, 2010 at 14:45 from IEEE Xplore. Restrictions apply.

Waveform Diversity Based Ultrasound System for Hyperthermia Treatment of Breast Cancer

Bin Guo, *Member, IEEE,* and Jian Li, *Fellow, IEEE*

***Abstract*—In this letter, we present a new waveform-diversity-based ultrasound hyperthermia technique for the treatment of breast cancer. Waveform diversity offers a new paradigm for beampattern design. By choosing a proper covariance matrix of the transmitted waveforms under the uniform elemental power constraint, the ultrasound system can provide a focal spot matched to the entire tumor region, and meanwhile, minimize the impact to the surrounding healthy breast tissues. As shown in our 2-D numerical simulations, this method has better acoustic power deposition than the existing methods, and can provide the necessary temperature gradients required for the effective hyperthermia treatment of breast cancer.**

***Index Terms*—Beampattern design, breast cancer, finite-difference time domain (FDTD), ultrasound hyperthermia, waveform diversity.**

I. Introduction

BREAST CANCER is the most common nonskin malignancy in women and the second leading cause of female cancer mortality [1]. There are over 200 000 new cases of invasive breast cancer diagnosed each year in the United States, and one out of every seven women in the United States will be diagnosed with breast cancer in their life time.[1]

The development of breast cancer imaging techniques, such as microwave imaging [2], [3], ultrasound imaging [4], [5], thermal acoustic imaging [6], and magnetic resonance imaging (MRI), has improved the ability to visualize and accurately locate the breast tumor without the need for surgery [7]. This has led to the probability of noninvasive local hyperthermia treatment of breast cancer. Many studies have been performed to demonstrate the effectiveness of the local hyperthermia on the treatment of breast cancer [8], [9]. A challenge in the local hyperthermia treatment of breast cancer is to heat the malignant tumors to a temperature above 43 °C for about 30–60 min, but to maintain a low-temperature level in the surrounding healthy breast tissue region.

There are two major classes of local hyperthermia techniques: microwave hyperthermia [10] and ultrasound hyperthermia [11]. The penetration of microwave is poor in biological tissues. Moreover, the focal spot generated by microwave is undesirable at the normal/cancerous tissues interface because of the long wavelength of the microwave. Ultrasound can achieve much better penetration depths than microwave. However, because the acoustic wavelength is very short, the focal spot generated by ultrasound is very small (millimeter or submillimeter in diameter) compared to the large tumor region (centimeter in diameter on average). Thus, many focal spots are required for complete tumor coverage, and this results in a long treatment time and missed cancer cells.

In this letter, we present a waveform-diversity-based ultrasound hyperthermia technique for the treatment of breast cancer. Waveform diversity is a new beampattern design technique recently proposed for multiple-input–multiple-output (MIMO) radar (see [12] and the references therein). Unlike the standard phased-array technique, transmitting multiple different waveforms via its transducers offers more flexibility for transmit beampattern design. By designing the transmitted signal cross-correlation matrix under the uniform elemental power constraint, the waveform diversity can be exploited to maximize the power deposition at the entire tumor region while minimizing the impact on the surrounding healthy tissue region.

To validate our algorithm, we develop a 2-D breast model with an embedded tumor. The model includes the breast tissue, skin, and chest wall. The finite-difference time-domain (FDTD) method is used to simulate the acoustic field and the temperature distribution within the breast. We show with numerical simulations that the proposed method can provide the necessary temperature gradients required for the effective hyperthermia treatment of the tumor and maintain a low-temperature level at the surrounding healthy tissue region.

II. Waveform-Diversity-Based Ultrasound Hyperthermia

We consider an ultrasound hyperthermia system as shown in Fig. 1. Let $\mathbf{r}_0$ denote the center location of the tumor, which is assumed to be estimated accurately *a priori* using breast cancer imaging techniques. There are M acoustic transducers deployed around the breast at locations $\mathbf{r}_m$ ($m = 1, 2, \ldots, M$). Let $x_m(n)$ ($n = 1, 2, \ldots, N$) denote the discrete-time baseband signal transmitted by the mth acoustic transducer, where N denotes the number of samples of each transmitted signal pulse.

Manuscript received October 3, 2006; revised April 13, 2007. This work was supported in part by the National Science Foundation under Grant CCF-0634786, the U.S. Army Medical Research and Materiel Command under Contract W81XWH-06-1-0389, and the National Natural Science Foundation of China under Grant 60428101. *Asterisk indicates corresponding author*.

*B. Guo was with the Department of Electrical and Computer Engineering, University of Florida, P.O. Box 116130, Gainesville, FL 32611 USA. He is now with the Department of Electrical and Computer Engineering, Duke University, Durham, NC 27705 USA(e-mail: guobin@dsp.ufl.edu).

J. Li is with the Department of Electrical and Computer Engineering, University of Florida, Gainesville, FL 32611 USA (e-mail: li@dsp.ufl.edu).

Color versions of one or more of the figures in this letter are available online at http://ieeexplore.ieee.org.

Digital Object Identifier 10.1109/TBME.2007.912676

[1]The American Cancer Society, 2006, http://www.cancer.org

0018-9294/$25.00 © 2008 IEEE

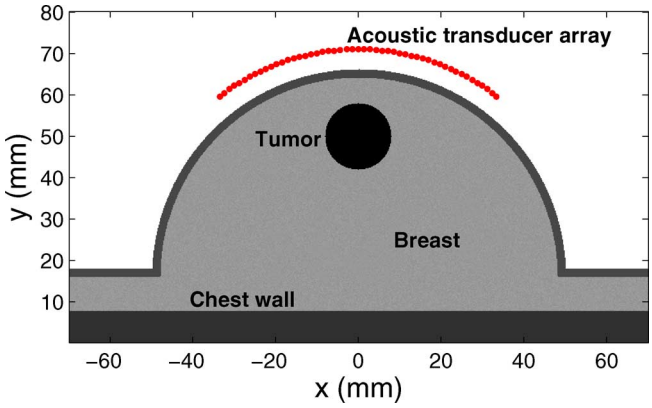

Fig. 1. Breast model.

We assume that the transmitted acoustic signals are narrowband and each acoustic transducer is omnidirectional. The baseband signal at a location $\mathbf{r}$ inside the breast can be described as

$$y(\mathbf{r},n)=\sum_{m=1}^{M}\frac{e^{-j2\pi f_0\tau_m(\mathbf{r})}}{||\mathbf{r}_m-\mathbf{r}||^{1/2}}x_m(n),\qquad n=1,\,2,\,\ldots,\,N \tag{1}$$

where f_0 is the carrier frequency

$$\tau_m(\mathbf{r})=\frac{||\mathbf{r}_m-\mathbf{r}||}{c} \tag{2}$$

is the time needed by the signal emitted via the mth transducer to arrive at the location $\mathbf{r}$, with c being the sound speed inside the breast tissues, and $1/||\mathbf{r}_m-\mathbf{r}||^{1/2}$ is the propagation attenuation of the acoustic wave. Let

$$\mathbf{a}(\mathbf{r})=\left[\frac{e^{j2\pi f_0\tau_1(\mathbf{r})}}{||\mathbf{r}_1-\mathbf{r}||^{1/2}}\quad\frac{e^{j2\pi f_0\tau_2(\mathbf{r})}}{||\mathbf{r}_2-\mathbf{r}||^{1/2}}\quad\cdots\quad\frac{e^{j2\pi f_0\tau_M(\mathbf{r})}}{||\mathbf{r}_M-\mathbf{r}||^{1/2}}\right]^{\mathrm{T}} \tag{3}$$

be the steering vector with $(\cdot)^{\mathrm{T}}$ denoting the transpose, and let

$$\mathbf{x}(n)=[x_1(n)\quad x_2(n)\quad\cdots\quad x_M(n)]^{\mathrm{T}}. \tag{4}$$

Equation (1) can be rewritten as

$$y(\mathbf{r},n)=\mathbf{a}^*(\mathbf{r})\mathbf{x}(n),\qquad n=1,\,2,\,\ldots,\,N \tag{5}$$

where $(\cdot)^*$ denotes the conjugate transpose.

The power of the transmitted signals at location $\mathbf{r}$, which is also called the transmit beampattern [12], is given by

$$P(\mathbf{r})=\mathrm{E}\{y(\mathbf{r},n)y^*(\mathbf{r},n)\}=\mathbf{a}^*(\mathbf{r})\mathbf{R}\mathbf{a}(\mathbf{r}) \tag{6}$$

where $\mathbf{R}$ is the covariance matrix of $\mathbf{x}(n)$, i.e.,

$$\mathbf{R}=\mathrm{E}\{\mathbf{x}(n)\mathbf{x}^*(n)\}. \tag{7}$$

The transmit beampattern is a function of the location $\mathbf{r}$.

The purpose of our waveform-diversity technique is to focus the acoustic power onto the entire tumor region while minimizing the peak power level at the surrounding healthy breast tissue region. The corresponding beampattern design problem is to choose the covariance matrix $\mathbf{R}$ under the uniform elemental power constraint

$$R_{mm}=\frac{b}{M},\qquad m=1,\,2,\,\ldots,\,M \tag{8}$$

where R_{mm} denotes the (m,m)th element of $\mathbf{R}$, and b is the total transmitted power, to achieve the following goals:

1) achieve a predetermind main-beam width matching the entire tumor region (be within 10% of the power deposited at the tumor center);
2) minimize the peak sidelobe level in a prescribed region (the surrounding healthy breast tissue region).

This problem can be formulated as

$$\begin{aligned}&\min_{t,\mathbf{R}}\ -t\\ &\text{s.t.}\quad \mathbf{a}^*(\mathbf{r}_0)\mathbf{R}\mathbf{a}(\mathbf{r}_0)-\mathbf{a}^*(\boldsymbol{\mu})\mathbf{R}\mathbf{a}(\boldsymbol{\mu})\ge t\qquad \forall\,\boldsymbol{\mu}\in\Omega_B\\ &\qquad \mathbf{a}^*(\boldsymbol{\nu})\mathbf{R}\mathbf{a}(\boldsymbol{\nu})\ge 0.9\mathbf{a}^*(\mathbf{r}_0)\mathbf{R}\mathbf{a}(\mathbf{r}_0)\qquad \forall\,\boldsymbol{\nu}\in\Omega_T\\ &\qquad \mathbf{a}^*(\boldsymbol{\nu})\mathbf{R}\mathbf{a}(\boldsymbol{\nu})\le 1.1\mathbf{a}^*(\mathbf{r}_0)\mathbf{R}\mathbf{a}(\mathbf{r}_0)\qquad \forall\,\boldsymbol{\nu}\in\Omega_T\\ &\qquad \mathbf{R}\ge 0\\ &\qquad R_{mm}=\frac{b}{M},\qquad m=1,\,2,\,\ldots,M\end{aligned} \tag{9}$$

where Ω_T and Ω_B denote the tumor region and the surrounding healthy breast tissue regions (sidelobe region), respectively.

As shown in [12], this beampattern design problem is a semidefinite program (SDP) and can be efficiently solved in polynomial time using public domain software. Once $\mathbf{R}$ is determined, a signal sequence $\{\mathbf{x}(n)\}$ that has $\mathbf{R}$ as its covariance matrix can be synthesized as

$$\mathbf{x}(n)=\mathbf{R}^{1/2}w(n),\qquad n=1,\,2,\,\ldots,\,N \tag{10}$$

where $\{w(n)\}$ is a sequence of independent identically distributed (i.i.d.) random vectors with mean zero and covariance matrix $\mathbf{I}$, and $\mathbf{R}^{1/2}$ denotes a square root of $\mathbf{R}$.

By transmitting $\mathbf{x}(n)$ given in (10) using the acoustic transducer array, we can approximately get a desired high acoustic power deposition matching the entire tumor region while minimizing the power deposition at the surrounding healthy breast tissue region.

III. Model and Numerical Results

A. Breast Model and Simulation

For simulation purposes, a 2-D breast model is established, as shown in Fig. 1. The breast model is a 10-cm-diameter semicircle, which includes breast tissues, skin, and chest wall. The acoustic properties of the breast tissues within the breast are assumed random with a variation of ±5% around the nominal values. A 16-mm-diameter tumor is embedded below the skin with the tumor center location being ($x=0$ mm and $y=50$ mm). There are 51 acoustic transducers deployed uniformly around the breast model. The distance between the neighboring acoustic transducers is 1.5 mm (half wavelength of the carrier frequency). Acoustic wave with frequency 500 kHz is used as the carrier frequency.

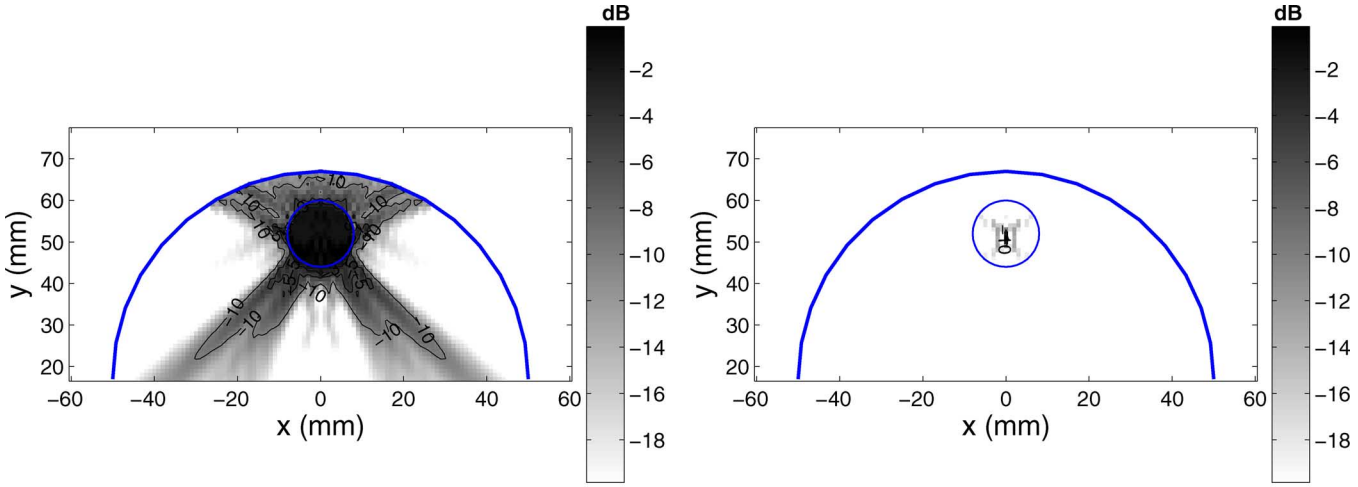

Fig. 2. Beampattern. (a) Waveform diversity. (b) Phased array.

TABLE I
TYPICAL ACOUSTIC PROPERTIES OF BREAST TISSUES

Tissues	$\rho\ (kg/m^3)$	$c\ (m/s)$	$\alpha\ (dB/cm)$
Breast Tissue	1020	1510	0.26
Skin	1100	1537	1.0
Chest Wall	1041	1580	0.28
Tumor	1041	1580	0.28

TABLE II
TYPICAL THERMAL PROPERTIES OF BREAST TISSUES

Tissues	K $(\frac{W}{m\cdot^\circ C})$	A $(\frac{W}{m^3})$	B $(\frac{W}{^\circ C\cdot m^3})$	C $(\frac{J}{kg\cdot^\circ C})$
Breast Tissue	0.499	480	2700	3550
Skin	0.376	1620	9100	3500
Chest Wall	0.564	480	2700	3510
Tumor	0.564	480	2700	3510

The two basic linear acoustic wave generation equations are [13], [14]

$$\rho\frac{\partial}{\partial t}\mathbf{u}(\mathbf{r},t) = -\nabla p(\mathbf{r},t) \tag{11}$$

and

$$\nabla\cdot\mathbf{u}(\mathbf{r},t) = -\frac{1}{\rho c^2}\frac{\partial}{\partial t}p(\mathbf{r},t) + \alpha p(\mathbf{r},t) \tag{12}$$

where $\mathbf{u}(\mathbf{r},t)$ is the acoustic velocity vector, $p(\mathbf{r},t)$ is the acoustic pressure field, ρ is the mass density, and α is the attenuation coefficient. The nominal values for these acoustic properties for different breast tissues are listed in Table I [4], [15], [16]. The values for the tumor are approximated using those for muscle because we cannot find the values specific to the tumor. FDTD is used to compute the acoustic field distribution based on (11) and (12). More details about FDTD for acoustic simulations can be found in [17] and [18].

Once the acoustic pressure is calculated, the acoustic power deposition at location $\mathbf{r}$, denoted as $Q(\mathbf{r})$, is given as [14]

$$Q(\mathbf{r}) = \frac{\alpha}{\rho c}|p(\mathbf{r})|^2. \tag{13}$$

After obtaining the acoustic power deposition, the 2-D thermal model, corresponding to the 2-D acoustic models, is used to calculate the temperature distribution in the breast tissues. The thermal model is based on the bioheat equation [19]

$$\nabla(K(\mathbf{r})\nabla T) + A(\mathbf{r}) + Q(\mathbf{r}) - B(\mathbf{r})(T - T_B) = C(\mathbf{r})\rho(\mathbf{r})\frac{\partial T}{\partial t} \tag{14}$$

where $K(\mathbf{r})$ is the thermal conductivity, $A(\mathbf{r})$ is metabolic heat production, $B(\mathbf{r})$ represents the heat exchange mechanism due to capillary blood perfusion, $C(\mathbf{r})$ is the specific heat, and T_B is the blood temperature, which can be assumed as the body temperature. The thermal properties for our breast model are listed in Table II. More detailed discussions can be found in [19].

The thermal models are also simulated using the FDTD method [20]. The body temperature and the environmental temperature are set at 36.8 °C and 20 °C, respectively. The convective boundary condition is used at the skin surface.

B. Numerical Results

We demonstrate the performance of our waveform-diversity-based method via several numerical examples. For comparison purposes, the conventional delay-and-sum (DAS)-based phased-array beamforming method is also applied to the same model, and its results are compared with those of our waveform-diversity-based method.

DAS-based phased-array beamformer transmits the same waveform using a weight vector

$$\mathbf{w} = \frac{\mathbf{a}(\mathbf{r}_0)}{||\mathbf{a}(\mathbf{r}_0)||^2}. \tag{15}$$

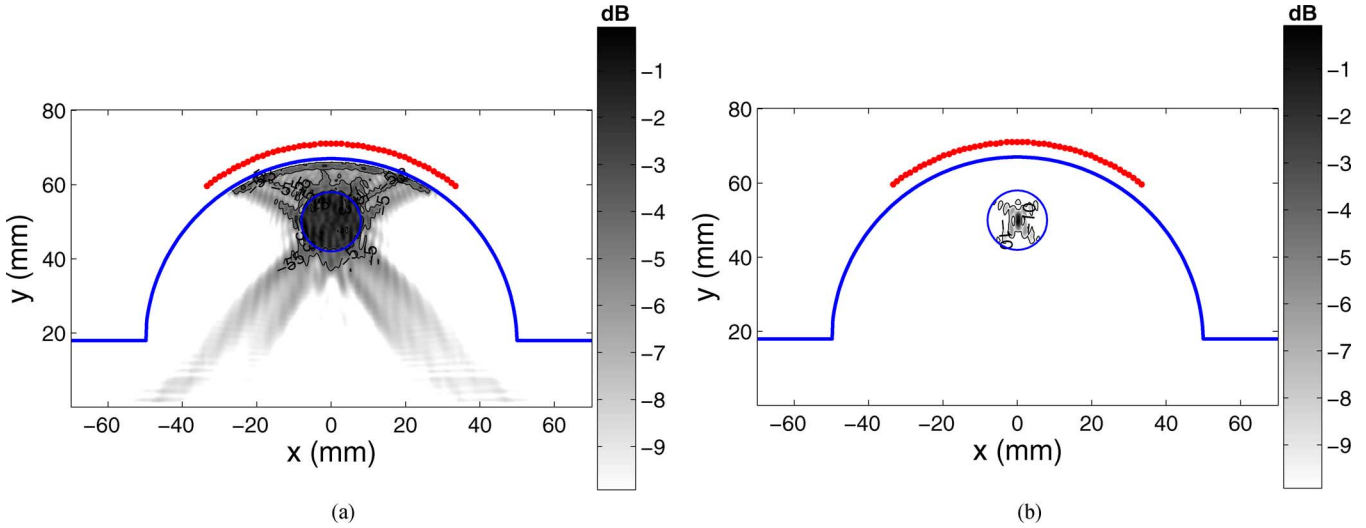

Fig. 3. Power deposition. (a) Waveform diversity. (b) Phased array.

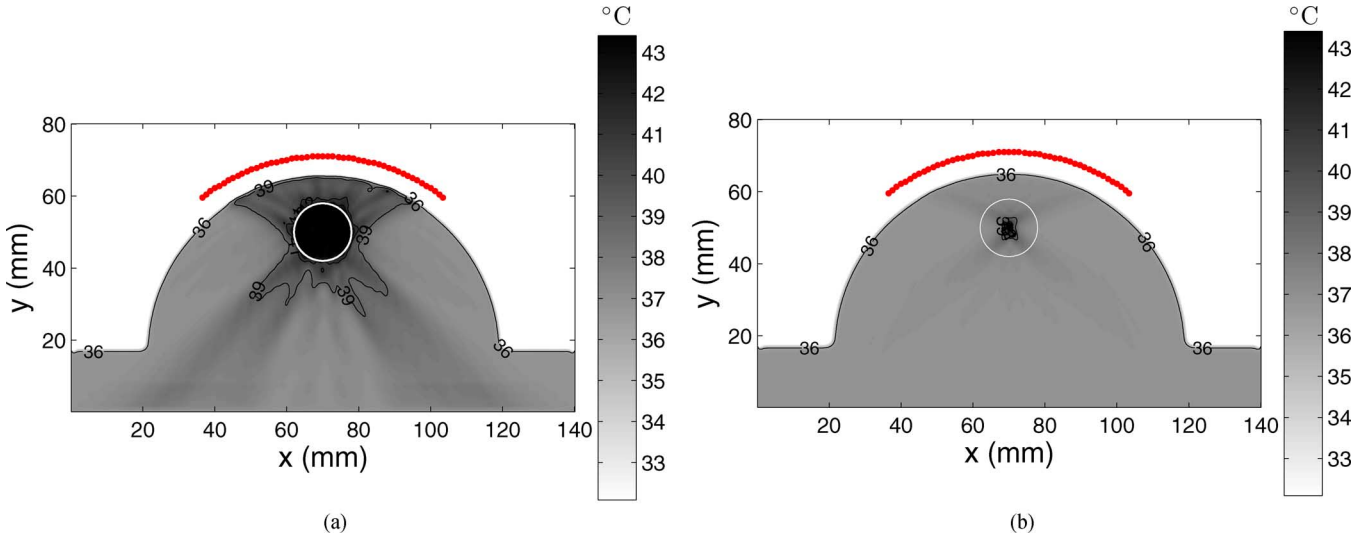

Fig. 4. Temperature distribution. (a) Waveform diversity. (b) Phased array.

The corresponding beampattern is

$$P(\mathbf{r}) = |\mathbf{a}^*(\mathbf{r})\,\mathbf{w}|^2. \tag{16}$$

Fig. 2 shows the calculated beampattern within the breast model. The blue lines in these figures mark the boundary of the breast and the tumor. Fig. 2(a) is the beampattern due to our waveform diversity technique which is calculated by using (6) with the optimal covariance matrix $\mathbf{R}$ determined by using (9). The figure shows that the 3-dB main beam is matched to the tumor region well, and the sidelobe level is low. Fig. 2(b) is the DAS beampattern which is calculated using (16). It is shown that the DAS beampattern is very narrow, and only focuses at the center region of the tumor.

Fig. 3(a) and (b) shows the acoustic power densities within the breast model for the waveform diversity technique and DAS, respectively. The dots mark the locations of the acoustic transducers. It is shown that the acoustic power densities in Fig. 3 agree with the beampatterns in Fig. 2 very well, and our waveform diversity technique gives a focal spot matching the entire tumor region.

Fig. 4 shows the temperature distributions within the breast model. Fig. 4(a) is the result of waveform diversity, which shows that the entire tumor region is heated to a temperature greater than 43 °C while maintaining the surrounding healthy tissues at a low-temperature level (below 40 °C). As a comparison, DAS only heats a very small region to a temperature greater than 43 °C at the center of the tumor.

IV. Conclusion

In this letter, we have presented a new waveform-diversity-based ultrasound hyperthermia technique for the treatment of breast cancer. By choosing the covariance matrix of the transmitted waveforms properly, this method can provide a focal spot matching the entire tumor region while minimizing the impact on the surrounding healthy breast region. As shown with 2-D

simulation examples, this method has better acoustic power deposition than its conventional counterpart, and can provide the necessary temperature gradients required for the effective hyperthermia of breast cancer.

REFERENCES

[1] E. C. Fear, P. M. Meaney, and M. A. Stuchly, "Microwaves for breast cancer detection," *IEEE Potentials*, vol. 22, no. 1, pp. 12–18, Feb.–Mar. 2003.

[2] P. M. Meaney, M. W. Fanning, D. Li, S. P. Poplack, and K. D. Paulsen, "A clinical prototype for active microwave imaging of the breast," *IEEE Trans. Microw. Theory Tech.*, vol. 48, no. 11, pp. 1841–1853, Nov. 2000.

[3] B. Guo, Y. Wang, J. Li, P. Stoica, and R. Wu, "Microwave imaging via adaptive beamforming methods for breast cancer detection," *J. Electromagn. Waves Appl.*, vol. 20, no. 1, pp. 53–63, 2006.

[4] T. Szabo, *Diagnostic Ultrasound Imaging: Inside Out*. Burlington, MA: Elsevier, 2004.

[5] F. W. Kremkau, *Diagnostic Ultrasound: Principles and Instruments*. Philadelphia, PA: W. B. Saunders, 1993.

[6] R. A. Kruger, K. K. Kopecky, A. M. Aisen, D. R. Reinecke, G. A. Kruger, and W. L. Kiser, "Thermoacoustic CT with radio waves: A medical imaging paradigm," *Radiology*, vol. 211, pp. 275–278, Apr. 1999.

[7] D. Gianfelice, A. Khiat, M. Amara, A. Belblidia, and Y. Boulanger, "MR imaging-guided focused US ablation of breast cancer: Histopathologic assessment of effectiveness-initial experience," *Radiology*, vol. 227, pp. 849–855, Apr. 2003.

[8] M. H. Falk and R. D. Issels, "Hyperthermia in oncology," *Int. J. Hyperthermia*, vol. 17, pp. 1–18, Jan. 2001.

[9] C. C. Vernon, J. W. Hand, S. B. Field, D. Machin, J. B. Whaley, J. Van Der Zee, W. L. J. Van Putten, G. C. Van Rhoon, J. D. P. Van Dijk, D. G. González, F. Liu, P. Goodman, and M. Sherar, "Radiotherapy with or without hyperthermia in the treatment of superficial localized breast cancer: Results from five randomized controlled trials," *Int. J. Radiat. Oncol. Biol. Phys.*, vol. 35, pp. 731–744, Jul. 1996.

[10] A. J. Fenn, V. Sathiaseelan, G. A. King, and P. R. Stauffer, "Improved localization of energy deposition in adaptive phased-array hyperthermia treatment of cancer," *Lincoln Lab. J.*, vol. 9, no. 2, pp. 187–195, 1996.

[11] C. J. Diederich and K. Hynynen, "Ultrasound technology for hyperthermia," *Ultrasound Med. Biol.*, vol. 25, pp. 871–887, Jul. 1999.

[12] P. Stoica, J. Li, and Y. Xie, "On probing signal design for MIMO radar," *IEEE Trans. Signal Process.*, vol. 55, no. 8, pp. 4151–4161, Aug. 2007.

[13] D. T. Blackstock, *Fundamentals of Physical Acoustics*. New York: Wiley, 2000.

[14] A. D. Pierce, *Acoustics: An Introduction to Its Physical Principles and Applications*. New York: McGraw-Hill, 1994.

[15] F. A. Duck, *Physical Properties of Tissue*. London, U.K.: Academic, 1990.

[16] F. A. Duck, A. C. Baker, and H. C. Starritt, *Ultrasound in Medicine*. Philadelphia, PA: Institute of Physics, 1998.

[17] X. Yuan, D. Borup, J. Wiskin, M. Berggren, and S. A. Johnson, "Simulation of acoustic wave propagation in dispersive media with relaxation losses by using FDTD method with PML absorbing boundary condition," *IEEE Trans. Ultrason. Ferroelectr. Freq. Control*, vol. 46, no. 1, pp. 14–23, Jan. 1999.

[18] T. K. Katsibas and C. S. Antonopoulos, "A general form of perfectly matched layers for three-dimensional problems of acoustic scattering in lossless and lossy fluid media," *IEEE Trans. Ultrason. Ferroelectr. Freq. Control*, vol. 51, no. 8, pp. 964–972, Aug. 2004.

[19] P. Bernardi, M. Cavagnaro, S. Pisa, and E. Piuzzi, "Specific absorption rate and temperature elevation in a subject exposed in the far-field of radio-frequency sources operating in the 10–900-MHz range," *IEEE Trans. Biomed. Eng.*, vol. 50, no. 3, pp. 295–304, Mar. 2003.

[20] J. Wang and O. Fujiwara, "FDTD computation of temperature rise in the human head for portable telephones," *IEEE Trans. Microw. Theory Tech.*, vol. 47, no. 8, pp. 1528–1534, Aug. 1999.

Multifrequency Microwave-Induced Thermal Acoustic Imaging for Breast Cancer Detection

Bin Guo, *Member, IEEE*, Jian Li*, *Fellow, IEEE*, Henry Zmuda, *Member, IEEE*, and Mark Sheplak

***Abstract*—Microwave-induced thermal acoustic imaging (TAI) is a promising early breast cancer detection technique, which combines the advantages of microwave stimulation and ultrasound imaging and offers a high imaging contrast, as well as high spatial resolution at the same time. A new multifrequency microwave-induced thermal acoustic imaging scheme for early breast cancer detection is proposed in this paper. Significantly more information about the human breast can be gathered using multiple frequency microwave stimulation. A multifrequency adaptive and robust technique (MART) is presented for image formation. Due to its data-adaptive nature, MART can achieve better resolution and better interference rejection capability than its data-independent counterparts, such as the delay-and-sum method. The effectiveness of this procedure is shown by several numerical examples based on 2-D breast models. The finite-difference time-domain method is used to simulate the electromagnetic field distribution, the absorbed microwave energy density, and the thermal acoustic field in the breast model.**

***Index Terms*—Breast cancer detection, finite-difference time-domain (FDTD) methods, multifrequency adaptive and robust technology (MART), robust capon beamforming (RCB), thermal acoustic imaging (TAI).**

I. Introduction

BREAST cancer is the most common nonskin malignancy in women and the second leading cause of female cancer mortality [1]. There are over 200 000 new cases of invasive breast cancer diagnosed each year in the U. S., and one out of every seven women in the U.S. will be diagnosed with breast cancer in their life time (the American Cancer Society, 2006) and early diagnosis is key to surviving breast cancer [2]. Microwave imaging is a method for early breast cancer detection [3]–[9], which exploits the significant contrast in dielectric properties between normal and cancerous tissues [10]–[12]. However, it is difficult for microwave imaging techniques to achieve good (submillimeter) spatial resolution because of its long wavelength [13]. Ultrasound is another option which offers a high spatial resolution because of its short acoustic wavelength [14]–[16]. However, the contrast in acoustic properties between normal and tumor tissues is very small due to both being soft tissues.

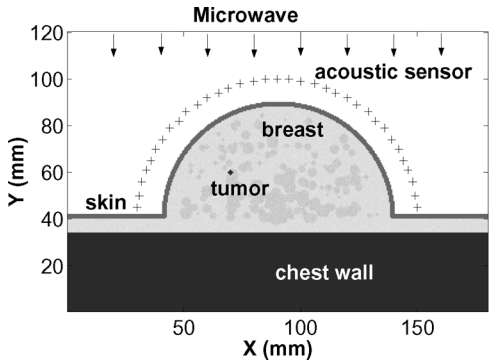

Fig. 1. Model of microwave-induced TAI for breast cancer detection.

Microwave-induced thermal acoustic imaging (TAI) combines the advantages of microwave stimulation and ultrasound imaging [13], which offers a high imaging contrast (due to the significantly different dielectric properties of tumor and normal breast tissues), as well as high spatial resolution (due to the low propagation velocity or the short wavelength of acoustic waves in biological tissues) at the same time. To use microwave-induced TAI techniques for breast cancer imaging, a microwave source with a short duration time is used to irradiate the breast, as shown in Fig. 1. The normal breast tissues, as well as tumors, absorb microwave energy and emanate thermal acoustic waves by thermoelastic expansion. It is well-known that malignant breast tissue has a higher water content [1], [10], [12], [17], with a much higher conductivity than normal breast tissues (with low water content). As a result, the microwave energy absorbed by tumor and normal breast tissues will be significantly different and a stronger acoustic wave will be produced by the tumor. The acoustic waves generated in this manner carry the information about the microwave energy absorption properties of the tissues under irradiation. The thermal acoustic waves propagate out of the breast and are recorded by an acoustic sensor array placed around the breast. The tumor locations can be accurately determined since the received acoustic signals from the malignant tumors are at higher levels, hence aiding image construction.

During the last decade, several research groups have been working on the microwave-induced TAI of biological tissues [18]–[23]. The microwave frequency used ranges from 400 MHz [22] to 3 GHz [13]. Image reconstruction algorithms include the

Manuscript received August 22, 2006; revised February 7, 2007. This work was supported in part by the National Institutes of Health under Grant 1R41CA107903-1, in part by the U.S. Army Medical Command under Contract W81XWH-06-1-0389, and in part by the National Natural Science Foundation of China under Grant 60428101. *Asterisk indicates corresponding author*.

B. Guo and H. Zmuda are with the Department of Electrical and Computer Engineering, University of Florida, Gainesville, FL 32611 USA (e-mail: guobin@dsp.ufl.edu).

*J. Li is with the Department of Electrical and Computer Engineering, P.O. Box 116130, University of Florida, Gainesville, FL 32611 USA (e-mail: li@dsp.ufl.edu).

M. Sheplak is with the Department of Mechanical and Aerospace Engineering, University of Florida, Gainesville, FL 32611 USA.

Color versions of one or more of the figures in this paper are available online at http://ieeexplore.ieee.org.

Digital Object Identifier 10.1109/TBME.2007.895108

0018-9294/$25.00 © 2007 IEEE

widely used delay-and-sum (DAS) method [20], [23], the frequency-domain inverse method [24], [25], and the time-domain inverse method [13], [19].

Microwave-induced TAI does, however, present several challenges. First, the human breast is large in size, usually has an irregular shape if not compressed, and is covered with a 2–mm-thick skin with dielectric properties significantly different from the normal breast tissues. Moreover the breast tissue is far from homogeneous because the dielectric properties of glandular tissue are different from that of breast fatty tissue. All these factors make it difficult to approximate the back propagation properties of thermal acoustic signals inside the breast. Due to the slow acoustic wave propagation speed or short wavelength in biological tissues, the errors on the order of millimeters in determining the acoustic signal propagation path lengths will severely degrade the image quality.

In this paper, a multifrequency microwave-induced TAI system is proposed which remedy the problems mentioned above. Instead of using a single frequency microwave source, as generally done by other research groups in this field, here a multiple frequency source is used, since the desired thermal acoustic signals can be induced by microwave sources operating at a wide range of frequencies. We show in this paper that the rich information collected from the multifrequency stimulation can help mitigate the challenges mentioned. The multifrequency microwave-induced thermal acoustic signals will offer higher signal-to-noise ratio (SNR) and higher imaging contrast than single-frequency microwave-induced thermal acoustic signals since much more information about the human breast can be harvested from the multiple stimulating frequencies within the microwave frequency band. Furthermore, the interference due to inhomogeneous breast tissue can be suppressed more effectively when multifrequency microwave-induced thermal acoustic signals are used for image reconstruction since more information about breast tissue can be used by the adaptive image reconstruction algorithms.

Another challenge encountered by microwave-induced TAI is the need to develop accurate and robust image reconstruction methods. DAS is a widely used reconstruction algorithm in medical imaging. This method is data-independent and tends to suffer from poor resolution and high sidelobe level problems. Data-adaptive approaches, such as the recently introduced robust Capon beamforming (RCB) [26], [27] method, can have much better resolution and much better interference rejection capabilities than their data-independent counterpart. Several medical imaging algorithms [4], [5], [28], [29] based on RCB have been developed and used for microwave imaging and thermal acoustic imaging. Good performances of these algorithms have been reported.

We present a multifrequency adaptive and robust technique (MART) based on RCB for multifrequency microwave-induced TAI. There are three stages in our MART. In Stage I, RCB is used to estimate the thermal acoustic responses from the grid locations within the breast for each stimulating microwave frequency. Then, in Stage II, a scalar acoustic waveform at each grid location is estimated based on the response estimates for all stimulating frequencies from Stage I. Finally, in Stage III, the positive peak and the negative peak of the estimated acoustic waveform at each grid location are determined, and the peak-to-peak difference is computed and referred to as the image intensity.

To validate the effectiveness of the proposed algorithm, we develop a 2-D inhomogeneous breast model, which includes skin, breast fatty tissues, glandular tissues, and the chest wall. Small tumors are set below the skin. The finite-difference time-domain (FDTD) method is used to simulate the electromagnetic field inside the breast tissues [30], [31]. The specific absorption rate (SAR) distribution is calculated based on the simulated electromagnetic field [32], [33]. Then FDTD is used again to simulate the propagation of the microwave-induced thermal acoustic waves [34], [35].

The remainder of this paper is organized as follows. In Section II, the microwave frequency properties of human breast are described. A proper microwave frequency band for multifrequency microwave-induced TAI is also given in this section. MART is proposed for image formation in Section III. In Section IV, 2-D electromagnetic and acoustic breast models are developed. The electromagnetic and acoustic simulation methods are also presented in this section. Imaging results based on numerical examples are provided in Section V. Section VI concludes the paper.

II. Microwave Properties of Human Breast

A. Cutoff Frequency of Human Breast

In a microwave-induced TAI system, the biological tissues should be heated by microwave sources in a uniform manner, otherwise thermal acoustic signals will be induced by a nonuniform microwave energy distribution, resulting in images difficult to interrupt. It is well-known that high-order electromagnetic field modes will be excited in a media if the microwave works at a frequency higher than a cutoff frequency of the media [36], and the microwave energy distribution is nonuniform at high-order modes [37]. To minimize the nonuniform microwave energy distribution inside the breast caused by the high-order electromagnetic modes, the microwave source should work at a frequency below a certain cutoff frequency.

To estimate the cutoff frequency for the human breast, we consider the simplified breast model shown in Fig. 2(a) consisting of a semicircular dielectric waveguide with a perfect magnetic conductor (PMC) at the bottom of the semicircle. Recall that the tangential components of the magnetic field are zero on the surface at the PMC. The PMC assumption is reasonable because the permittivity of the chest wall ($\varepsilon_r = 50$) is much greater than that of the normal breast tissues ($\varepsilon_r = 9$). In circular dielectric waveguide, if an electromagnetic mode has a field distribution whose tangential magnetic field components are zero at the center line of the circular waveguide, as shown in Fig. 2(b), the introduction of a PMC at the center line of the circular waveguide will not significantly change the boundary conditions and, hence, will not significantly alter the mode distribution. The modes in the semicircular dielectric waveguide can, thus, be estimated by determining the modes in a corresponding circular dielectric waveguide.

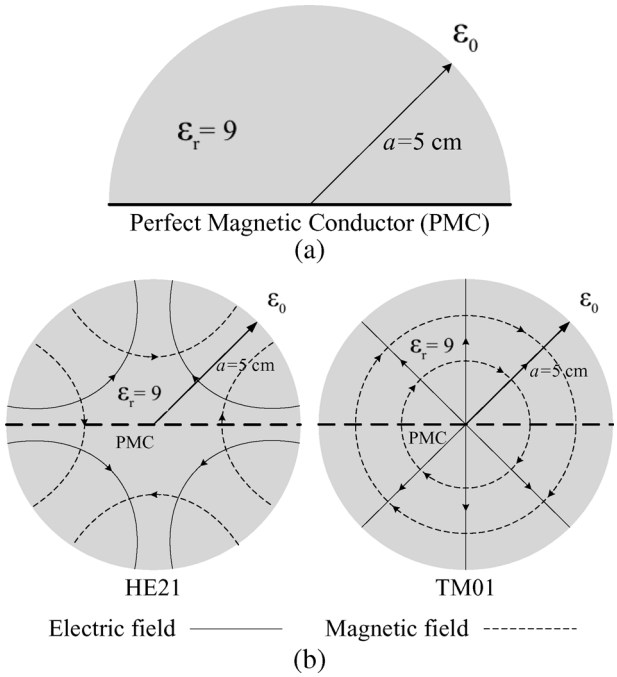

Fig. 2. Simplified breast model. (a) Semicircular dielectric waveguide with PEC, and (b) corresponding circular dielectric waveguide.

The dominant mode of a circular dielectric waveguide is the HE11 mode, the cutoff frequency of which is zero. The electromagnetic field distribution is near uniform at this mode. The dominant mode is followed by the TE01, TM01, and HE21 modes. These modes are degenerate, and have a cutoff frequency given by [36]

$$f_c = \frac{\chi_{01} C_0}{2\pi a \sqrt{\varepsilon_r - 1}} \tag{1}$$

where C_0 is the speed of light in free space, $\chi_{01} = 2.405$ is the first root of the Bessel function of the first kind of order zero $(J_0(\chi_{01}) = 0)$, a and ε_r are the radius and average permittivity of the circular dielectric waveguide, respectively. TM01 and HE21, as well as the interference between them, satisfy the zero tangential magnetic field component condition at the center line of the circular waveguide. These modes can also exist in the semicircular dielectric waveguide. By substituting the parameters of the breast model into (1), we obtain the cutoff frequency of the semicircular breast model to be

$$f_c = \frac{2.405 \cdot 3 \times 10^8}{2\pi \cdot 0.05 \cdot \sqrt{9-1}} = 812 \text{ MHz} \tag{2}$$

where we have used $a = 5$ cm and $\varepsilon_r = 9$ as typical values for human breast. Consequently, the stimulating microwave frequency for the TAI system should be below 812 MHz.

B. Microwave Energy Absorption Properties of Breast Tissues and Tumor

It is well-known that the complex relative dielectric properties of a medium can be expressed as

$$\varepsilon_r = \varepsilon_r' - j\varepsilon_r'' \tag{3}$$

TABLE I
COLE–COLE PARAMETERS FOR BIOLOGICAL TISSUES

Tissue	Breast	Skin	Muscle	Tumor
ε_∞	2.5	4.0	4.0	4.0
σ	0.01	0.0002	0.2	0.7
$\triangle\varepsilon_1$	3.0	32.0	50.0	50.0
τ_1 (ps)	17.68	7.23	7.23	7.0
α_1	0.1	0.0	0.1	0.0
$\triangle\varepsilon_2$	15	1100	7000	0
τ_2 (ns)	63.66	32.48	353.68	N/A
α_2	0.1	0.2	0.1	N/A
$\triangle\varepsilon_3$	5.0E4	0	1.2E6	0
τ_3 (μs)	454.7	N/A	318.31	N/A
α_3	0.1	N/A	0.1	N/A
$\triangle\varepsilon_4$	2.0E7	N/A	2.5E7	0
τ_4 (ms)	13.26	N/A	2.274	N/A
α_4	0.0	N/A	0.0	N/A

where ε_r' is the relative permittivity and ε_r'' is the out-of-phase loss factor which can be written as

$$\varepsilon_r'' = \frac{\sigma}{\varepsilon_0 \omega} \tag{4}$$

with σ being the total conductivity, ε_0 the free space permittivity, and ω the electromagnetic frequency. The tissue absorption property of the electromagnetic wave energy is

$$Q(\mathbf{r}) = \frac{1}{2}\sigma |E(\mathbf{r})|^2 \tag{5}$$

which is a function of the total conductivity and the electric field inside the tissue. If we assume that the microwave energy distribution is uniform inside the breast in a TAI system, the absorption of the microwave energy by the breast is characterized by the total conductivity of the breast tissues

$$\sigma(\omega) = \varepsilon_r'' \varepsilon_0 \omega. \tag{6}$$

Hence, instead of using the attenuation coefficient α, as used in [23], in this paper, we study the absorption properties of breast tissues using the total conductivity σ.

The dielectric properties of biological tissues can be accurately modeled by the Cole–Cole equation [38]

$$\varepsilon_r(\omega) = \varepsilon_\infty + \sum_{i=1}^{K} \frac{\Delta\varepsilon_i}{1 + (j\omega\tau_i)^{1-\alpha_i}} + \frac{\sigma_0}{j\omega\varepsilon_0} \tag{7}$$

where K is the order of the Cole–Cole model, ε_∞ is the high-frequency permittivity, τ_i is the relaxation time, $\Delta\varepsilon_i$ is the pole amplitude, α_i $(0 \le \alpha_i \le 1)$ is a measure of the broadening of dispersion, and σ_0 is the static ionic conductivity. The Cole–Cole parameters for skin, breast fatty tissue, chest wall (mainly consisting of muscle), as well as tumor are listed in Table I [39], [40]. Because we cannot find the values specific to the tumor, the dielectric properties of the tumor is approximated using a Debye model [3], [41], which is a special case of the Cole–Cole model.

Substituting (7) into (6), we obtain the total conductivity of the breast tissue as follows:

$$\sigma(\omega) = -\text{imag}\left(\varepsilon_\infty + \sum_{i=1}^{K} \frac{\Delta\varepsilon_i}{1 + (j\omega\tau_i)^{1-\alpha_i}} + \frac{\sigma}{j\omega\varepsilon_0}\right)\varepsilon_0\omega \tag{8}$$

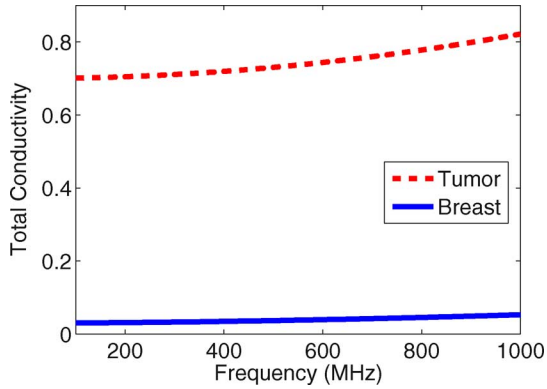

Fig. 3. Total conductivity of normal breast tissues and tumor as a function of frequency.

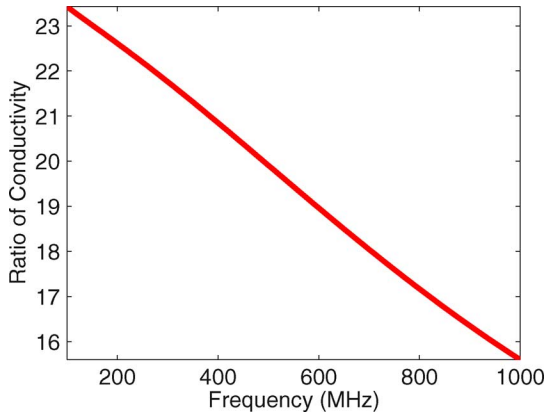

Fig. 4. Ratio of conductivity between tumor and normal breast tissue as a function of frequency.

which is a function of the stimulating microwave frequency, where $\mathrm{imag}(\cdot)$ denotes the imaginary part of the complex relative permittivity. Fig. 3 gives the total conductivity of breast fatty tissue and tumor over a frequency band from 100–1000 MHz. Note that the total conductivity increases with the microwave frequency, which means that more microwave energy is absorbed and converted to heat by tissues at higher microwave frequency region, or in other words, the SNR is higher in the received thermal acoustic signals at higher stimulating microwave frequency region. On the other hand, the penetration at higher microwave frequencies is smaller because the tissues are lossy. We define the conductivity ratio between the tumor and the normal breast tissue as

$$r_\sigma(\omega) = \frac{\sigma_{\mathrm{tumor}}(\omega)}{\sigma_{\mathrm{breast}}(\omega)} \tag{9}$$

and plot it as a function of frequency in Fig. 4. A high conductivity ratio means that more microwave energy is absorbed and converted to heat by tumor than by normal breast tissues. In other words, the higher the conductivity ratio, the higher the imaging contrast. Fig. 4 shows that the imaging contrast is higher at the lower microwave frequency region because the conductivity ratio decreases with the frequency.

These microwave energy absorption properties of breast tissues and tumor motivate us to consider inducing thermal acoustic signals with different microwave frequencies. By taking into account the aforementioned cutoff frequency given in (2), we choose a frequency range from 200–800 MHz. The frequency step is 100 MHz, with a total of seven frequencies. Note that wideband antenna techniques should be used for the practical implementation because the frequency range is wide. However, since the exciting microwave frequency is stepped, an antenna with a broad instantaneous bandwidth is not required. Another advantage of using multiple frequencies for stimulation is that more information about the inhomogeneous breast tissues will be harvested from the multifrequency microwave-induced thermal acoustic signals. The microwave energy distribution inside the breast model is not uniform because the human breast is inhomogeneous media, and thermal acoustic signals will be induced by the inhomogeneous energy distribution. These thermal acoustic signals will appear as clutter in the resulting images. However, the inhomogeneous microwave energy distributions are different at different stimulating frequencies because of the different microwave wavelengths in breast tissues. When a multifrequency microwave source is used for TAI, the thermal acoustic clutter induced by the inhomogeneous breast tissues can be suppressed by our adaptive and robust imaging algorithm.

III. Multifrequency Adaptive and Robust Technology (MART) for Breast Cancer Imaging

We consider a multifrequency microwave-induced TAI system as shown in Fig. 1, where an acoustic sensor array is arranged on a semicircle relatively close to the breast skin. The location of each acoustic sensor is $\mathbf{r}_j$ $(j = 1, \cdots, N)$, where N is the number of acoustic sensors. Assume that $M = 7$ microwave sources with different frequencies are used to irradiate the breast model. Let $p_{i,j}(t)$ $(i = 1, \cdots, M;\ j = 1, \cdots, N;\ t = 0, \cdots, T-1)$ denote the thermal acoustic signal induced by the i^{th} frequency and received by the j^{th} acoustic sensor, where T is the recording time which is sufficiently long to allow acoustic sensors to record all responses from the breast. Our goal is to detect the tumor by reconstructing an image of the thermal acoustic response intensity $I(\mathbf{r})$ as a function of scan location $\mathbf{r}$ within the breast.

A. Data Preprocessing

Because the breast skin, breast tissues, chest wall, and tumor absorb the microwave energy and convert the energy to heat, all of them produce thermal acoustic signals. The received thermal acoustic waveforms include the responses from the tumor, as well as from other healthy breast tissues. The thermal acoustic signals generated by the skin are much stronger than those by a small tumor because of the high conductivity of the skin and the acoustic sensors being very close to the skin. We must remove the skin responses to enhance the tumor responses. Because the distances between the acoustic sensors and the nearest breast skin are similar to one another, the signals recorded by various sensors have similar skin responses. Hence, we can remove the skin response by subtracting out a fixed calibration signal from all received signals. This calibration signal can be obtained simply by averaging the recorded signals from all channels.

Let $x_{i,j}(t)$ denote the signals after subtracting out the calibration signal. To process the signals coherently for a focal point

at $\mathbf{r}$, we align the signals $x_{i,j}(t)$ by time shifting each signal a number of samples $n_j(\mathbf{r})$. The discrete time delay between $\mathbf{r}$ and the j^{th} acoustic sensor can be calculated as

$$n_j(\mathbf{r}) = \left\lfloor \frac{\|\mathbf{r}_j - \mathbf{r}\|}{\Delta t c} \right\rceil \tag{10}$$

where $\lfloor \gamma \rceil$ stands for rounding to the greatest integer less than γ, $\|\mathbf{r}_j - \mathbf{r}\|$ is the distance between $\mathbf{r}_j$ and $\mathbf{r}$, c is the velocity of the acoustic wave propagating in breast tissues, and Δt is the sampling interval, which is assumed to be sufficiently small. The time-shifted signals are denoted as

$$\tilde{x}_{i,j}(t, \mathbf{r}) = x_{i,j}\left(t + n_j(\mathbf{r})\right), \quad t = -n_j(\mathbf{r}), \cdots, T - n_j(\mathbf{r}). \tag{11}$$

After time shifting, the acoustic signals from the imaging location $\mathbf{r}$ are aligned so that they all start approximately from time $t = 0$ for all channels. Now the aligned signals are windowed by

$$\text{Window}(l) = \begin{cases} 1, & 0 \le l \le L-1 \\ 0, & \text{otherwise} \end{cases} \tag{12}$$

to isolate the signals from the focal point at $\mathbf{r}$. The windowed signals are denoted as $\tilde{x}_{i,j}(l, \mathbf{r}), l = 0, \cdots, L-1$, where $L\Delta t$ is the approximate duration of the thermal acoustic pulse, which can be determined from the pulse duration of the pulsed microwave source.

Attenuation exists when acoustic waves propagate within the breast. This attenuation has two parts: the attenuation due to the lossy media and the propagation attenuation. Thus, the attenuation of the tumor responses at various channels are different because of the different distances between the imaging position $\mathbf{r}$ and the acoustic sensors. For the 2-D case considered here, the compensation factor for the j^{th} channel is given by

$$K_j(\mathbf{r}) = \exp\left(\alpha \|\mathbf{r}_j - \mathbf{r}\|\right) \cdot \|\mathbf{r}_j - \mathbf{r}\|^{1/2} \tag{13}$$

where the first term of the right side of (13) compensates for the attenuation due to the lossy media, and the second term compensates for the geometric attenuation. The compensated signal can be calculated as

$$y_{i,j}(l, \mathbf{r}) = K_j(\mathbf{r}) \cdot \tilde{x}_{i,j}(l, \mathbf{r}), \quad l = 0, \cdots, L-1. \tag{14}$$

B. Multifrequency Adaptive and Robust Technology (MART)

Without loss of generality, we consider imaging at a generic location $\mathbf{r}$ only. For notational convenience, we drop the dependence of $y_{i,j}(l, \mathbf{r})$ on $\mathbf{r}$, and simply denote it as $y_{i,j}(l)$. Now we consider the data model

$$y_{i,j}(l) = s_{i,j}(l) + e_{i,j}(l) \tag{15}$$

where $s_{i,j}(l)$ represents the tumor response and $e_{i,j}(l)$ represents the residual term, which includes the noise and interference from breast skin, chest wall, and other responses. The structure of the data model is a data cube as shown in Fig. 5.

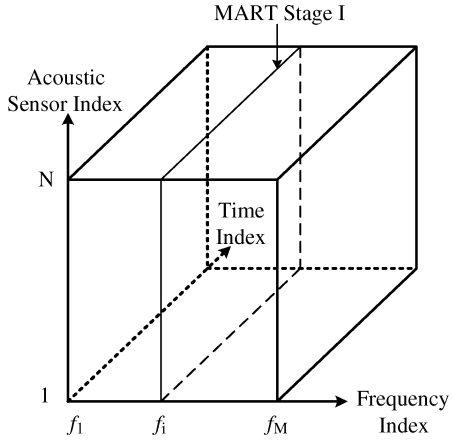

Fig. 5. Data cube model. In Stage I, MART slices the data cube for each frequency index. RCB is applied to each data slice to estimate the corresponding waveform.

MART is a three-stage time-domain signal processing algorithm. In Stage I, MART slices the data cube corresponding to each frequency index, and processes each data slice by the RCB to obtain the thermal acoustic waveform estimate for each stimulating frequency. Then, in Stage II, a scalar waveform is estimated from all frequencies based on the waveform estimates from Stage I. Finally, the positive peak and the negative peak of the estimated thermal acoustic waveform from Stage II are found in Stage III. The peak-to-peak difference is calculated as the image intensity at the focal point at $\mathbf{r}$. The details of all three stages are given below.

1) Stage I: In Stage I, MART approximates the data model as

$$\mathbf{y}_i(l) = \mathbf{a}_i s_i(l) + \mathbf{e}_i(l) \tag{16}$$

where $\mathbf{y}_i(l) = [y_{i,1}(l), \cdots, y_{i,N}(l)]^T$ and $\mathbf{e}_i(l) = [e_{i,1}(l), \cdots, e_{i,N}(l)]^T$. The scalar waveform $s_i(l)$ denotes the thermal acoustic signal generated at the focal location $\mathbf{r}$ corresponding to the i^{th} stimulating frequency. The vector $\mathbf{a}_i$ is referred to as the array steering vector, which is approximately equal to $\mathbf{1}_{N\times 1} = [1, \cdots, 1]^T$ since all the signals have been aligned temporally and their attenuation compensated for in the preprocessing step. The residual $\mathbf{e}_i(l)$ is the noise and interference term, which is assumed uncorrelated with the signal.

There are two assumptions made to write the model given in (16). First, the steering vector is assumed to vary with the microwave frequency (i) but nearly constant with the time sample (l). Second, we assume that the thermal acoustic signal waveform depends only on the microwave frequency (i) but not on the acoustic sensor (j). The truth, however, is that the steering vector is not exactly known as it changes slightly with both the stimulating frequency and time due to array calibration errors and other factors. The signal waveform can also vary slightly with both the stimulating frequency and acoustic sensor, due to the inhomogeneous and frequency-dependent medium within the breast. The two aforementioned assumptions simplify the problem slightly. They cause little performance degradations when used with our adaptive and robust algorithm.

In practice, the true steering vector in (16) is not $\mathbf{1}_{N\times 1}$. We assume that the true steering vector $\mathbf{a}_i$ lies in the vicinity of the assumed steering vector $\bar{\mathbf{a}} = \mathbf{1}_{N\times 1}$, and the only knowledge we have about $\mathbf{a}_i$ is that

$$\|\mathbf{a}_i - \bar{\mathbf{a}}\|^2 \leq \epsilon_1 \tag{17}$$

where ϵ_1 is a user parameter, which may be determined depending on the various errors discussed previously.

The true steering vector $\mathbf{a}_i$ can be estimated via the following covariance fitting approach of RCB [26], [27]

$$\max_{\delta_i^2, \mathbf{a}_i} \delta_i^2 \quad \text{subject to} \quad \hat{\mathbf{R}}_{\mathbf{Y}_i} - \delta_i^2 \mathbf{a}_i \mathbf{a}_i^T \geq 0 \quad \|\mathbf{a}_i - \bar{\mathbf{a}}\|^2 \leq \epsilon_1 \tag{18}$$

where δ_i^2 is the power of the signal $s_i(l)$ and

$$\hat{\mathbf{R}}_{\mathbf{Y}_i} \triangleq \frac{1}{L} \sum_{l=0}^{L-1} \mathbf{y}_i(l) \mathbf{y}_i^T(l) \tag{19}$$

is the sample covariance matrix. The above optimization problem can be solved as described in [26], and the estimated true steering vector is denoted here as $\hat{\mathbf{a}}_i$.

To obtain the signal waveform estimate, we pass the received signals through a Capon beamformer [27], [42]. The weight vector of the beamformer is determined by using the estimated steering vector $\hat{\mathbf{a}}_i$ in the following expression:

$$\mathbf{w}_i = \frac{\hat{\mathbf{R}}_{\mathbf{Y}_i}^{-1} \hat{\mathbf{a}}_i}{\hat{\mathbf{a}}_i^T \hat{\mathbf{R}}_{\mathbf{Y}_i}^{-1} \hat{\mathbf{a}}_i}. \tag{20}$$

Then the estimated signal waveform corresponding to the i^{th} stimulating frequency is

$$\hat{s}_i(l) = \mathbf{w}_i^T \mathbf{y}_i(l). \tag{21}$$

By repeating the aforementioned process for $i = 1$ through $i = M$, we obtain the complete set of M waveform estimates

$$\hat{\mathbf{s}}(l) = [\hat{s}_1(l), \cdots, \hat{s}_M(l)]^T. \tag{22}$$

2) Stage II: Since the stimulating microwave sources with various frequencies are assumed to have the same power, we assume that the thermal acoustic responses from the tumor at different stimulating frequencies have nearly identical waveforms. Note that the thermal acoustic responses induced by the inhomogeneous microwave energy distribution (due to the inhomogeneous breast tissues) are different at different stimulating frequencies. This means that the elements of the vector $\hat{\mathbf{s}}(l)$ are all approximately equal to an unknown scalar signal $s(l)$, and the noise and interference term can be assumed uncorrelated with this signal. In Stage II of MART, we adopt the data model

$$\hat{\mathbf{s}}(l) = \mathbf{a}_s s(l) + \mathbf{e}_s(l) \tag{23}$$

where $\mathbf{a}_s$ is approximately equal to $\mathbf{1}_{M\times 1}$. However, the "steering vector" may again be imprecise, and, hence, RCB is needed again.

As we did in Stage I, we assume that the only knowledge about $\mathbf{a}_s$ is that

$$\|\mathbf{a}_s - \bar{\mathbf{a}}_s\|^2 \leq \epsilon_2, \tag{24}$$

where $\bar{\mathbf{a}}_s = \mathbf{1}_{M\times 1}$ is the assumed steering vector, and ϵ_2 is a user parameter. Again, the true steering vector $\mathbf{a}_s$ can be estimated via the covariance fitting approach

$$\max_{\delta^2, \mathbf{a}_s} \delta^2 \quad \text{subject to} \quad \hat{\mathbf{R}}_s - \delta^2 \mathbf{a}_s \mathbf{a}_s^T \geq 0 \quad \|\mathbf{a}_s - \bar{\mathbf{a}}_s\|^2 \leq \epsilon_2 \tag{25}$$

where δ^2 is the power of the signal $s(l)$, and

$$\hat{\mathbf{R}}_s \triangleq \frac{1}{L} \sum_{l=0}^{L-1} \hat{\mathbf{s}}(l) \hat{\mathbf{s}}^T(l) \tag{26}$$

is the sample covariance matrix.

After obtaining the estimated steering vector $\hat{\mathbf{a}}_s$, we obtain the adaptive weight vector and the estimated signal waveform, respectively, as

$$\mathbf{w} = \frac{\hat{\mathbf{R}}_s^{-1} \hat{\mathbf{a}}_s}{\hat{\mathbf{a}}_s^T \hat{\mathbf{R}}_s^{-1} \hat{\mathbf{a}}_s} \tag{27}$$

and

$$\hat{s}(t) = \mathbf{w}^T \hat{\mathbf{s}}(t). \tag{28}$$

3) Stage III: Because the thermal acoustic pulse is usually bipolar: a positive peak, corresponding to the compression pulse, and a negative peak, corresponding to the rarefaction pulse [43], we use the peak-to-peak difference as the response intensity for the imaging location $\mathbf{r}$ in the third stage of MART. Compared with other energy or amplitude based response intensity estimation methods, peak-to-peak difference can be used to improve imaging quality with little additional computation costs.

The positive and negative peak values of the estimated waveform for the focal location $\mathbf{r}$ will be searched based on the estimated waveform (28) obtained in Stage II. Because of the nonuniform sound speed in biological tissues, the arrival time of the acoustic pulse generated at location $\mathbf{r}$ cannot be calculated accurately. However, it was reported in [18] that, when the heterogeneity is weak, such as in breast tissues, amplitude distortion caused by multipath is not severe. We assume that the original peak remains a peak in the estimated waveform, and the positive and negative peak values of the thermal acoustic pulse can be searched as

$$P^+ = \max \left\{ \max_{l \in [\Delta_1, \Delta_2]} \{\hat{s}(l)\}, 0 \right\} \tag{29}$$

and

$$P^- = \min \left\{ \min_{l \in [\Delta_1, \Delta_2]} \{\hat{s}(l)\}, 0 \right\} \tag{30}$$

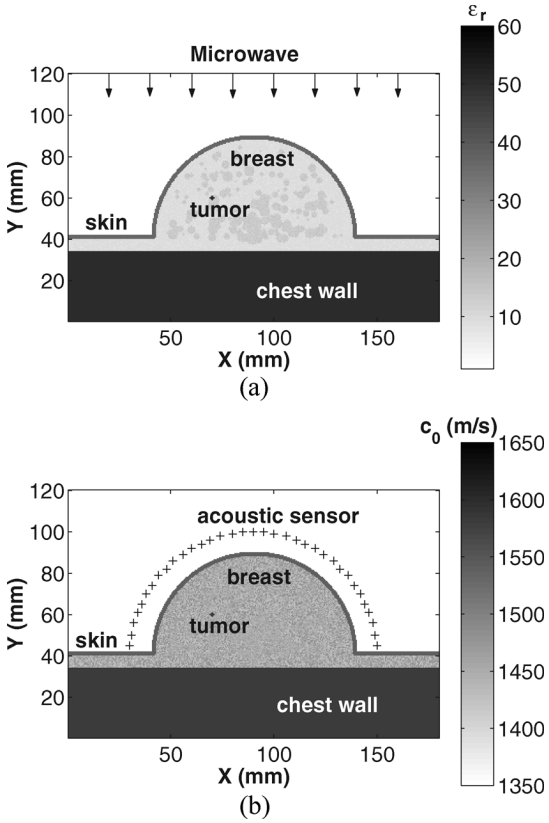

Fig. 6. Breast model for thermal acoustic simulation. (a) Model for electromagnetic simulation and (b) model for acoustic simulation.

where $[\Delta_1, \Delta_2] \in [0, L]$ is the searching range. Here Δ_1 and Δ_2 are user parameters, and the details on how to choose them can be found in [29].

After the positive and negative peak values are found, the response intensity for the focal point at location $\mathbf{r}$ is given as

$$I(\mathbf{r}) = P^+ - P^-. \tag{31}$$

IV. Modeling and Simulations

We consider 2-D breast models simulated in two steps. In the first step, the electromagnetic field inside the breast model is simulated and the SAR distribution is calculated based on the simulated electromagnetic field. The second step is for the acoustic wave simulation, where the SAR distribution obtained in the first step is used as the acoustic pressure source through the thermal expansion coefficient. In both steps, the FDTD method is used for the simulation examples.

A. Electromagnetic Model and Simulation

For simulation purposes, the 2-D electromagnetic breast model used is as shown in Fig. 6(a). The breast model is a 10 cm in diameter semicircle, which includes the skin, breast fatty tissue, glandular tissues, and chest wall (muscle). A 1-mm-diameter tumor is embedded below the skin. The dielectric properties of the breast tissues as well as tumor at the

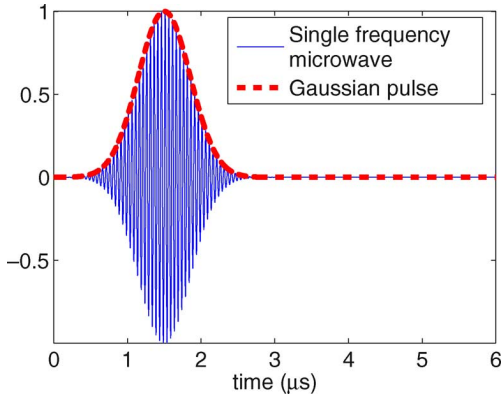

Fig. 7. Gaussian modulated microwave source.

microwave frequency f_i $(i = 1, \cdots, M)$ were calculated based on the Cole–Cole model in (7). The dielectric properties of the normal breast fatty tissue are assumed random with a variation of $\pm 10\%$ around the nominal values. The dielectric constants of glandular tissues are between $\varepsilon_r = 11$ and $\varepsilon_r = 15$.

Fig. 7 shows a Gaussian modulated electromagnetic wave used to irradiate the breast from the top of the model, as shown in Fig. 6(a). The time duration for the Gaussian pulse is 1 μs. The electromagnetic field is simulated using the FDTD method [30], [31]. The grid cell size used by FDTD is 0.5 $\times$ 0.5 mm and the computational region is terminated by perfectly matched layer (PML) absorbing boundary conditions [44], [45].

The SAR distribution is given as [32], [33]

$$\mathrm{SAR}(\mathbf{r}) = \frac{\sigma(\mathbf{r})E^2(\mathbf{r})}{2\rho(\mathbf{r})} \tag{32}$$

where $\sigma(\mathbf{r})$ is the conductivity of the biological tissues at location $\mathbf{r}$, $E(\mathbf{r})$ is the electric field at location $\mathbf{r}$, and $\rho(\mathbf{r})$ is the mass density of the biological tissues at location $\mathbf{r}$.

B. Acoustic Model and Simulation

In the microwave-induced TAI system, the microwave energy is small, and as a result, the acoustic pressure field induced by microwave is also small. So, the nonlinear acoustic effect does not need to be considered in the TAI system. For example, it is shown in [46] that the temperature rise is about 0.1 mK and the acoustic pressure change is only about 100 Pa in the microwave-induced TAI system. The shock distance in breast tissues is [47]

$$\chi_s = \frac{\frac{B}{2A}}{2\left(\frac{B}{2A}+1\right)} \cdot \frac{\rho_0 c^2}{p} \cdot \lambda_{\min} = \frac{\frac{B}{2A}}{2\left(\frac{B}{2A}+1\right)} \cdot \frac{\rho_0 c^2}{p} \cdot \frac{c}{f_{\max}} \tag{33}$$

where $(B/A)(\approx 10)$ is the nonlinear factor of the breast tissues, $\rho_0 (\approx 1000\ \mathrm{kg/m^3})$ is the mass density of the breast tissues, and $c (\approx 1500\ \mathrm{m/s})$ is the sound speed inside the breast tissues [14]. p is the acoustic pressure rise, and $\lambda_{\min}$ and $f_{\max}$ are the minimal acoustic wavelength and the maximal acoustic frequency of the thermal acoustic signal, respectively. For our breast model, the acoustic pressure rise is $p = 100$ Pa, and the

TABLE II
ACOUSTIC PARAMETERS FOR BIOLOGICAL TISSUES.
(* f IS THE ACOUSTIC FREQUENCY AND THE UNIT IS MEGAHERTZ)

Tissue	Breast	Skin	Muscle	Tumor
$\rho\ (kg/m^3)$	1020	1100	1041	1041
$c\ (m/s)$	1510	1537	1580	1580
$\alpha^*\ (dB/cm)$	$0.75f^{1.5}$	3.5	$0.57f$	$0.57f$
$\beta\ (1/^\circ C)$	3E-4	3E-4	3E-4	3E-4
$C_p\ (J/(^\circ C \cdot kg))$	3550	3500	3510	3510

maximal acoustic frequency is $f_{\max} = 500$ KHz. By substituting the parameters into (33), we obtain the shock distance in breast tissues to be

$$\begin{aligned}\chi_s &= \frac{\frac{B}{2A}}{2\left(\frac{B}{2A}+1\right)} \cdot \frac{\rho_0 c^2}{p} \cdot \frac{c}{f_{\max}} \\ &= \frac{5}{2(5+1)} \cdot \frac{1000 \cdot 1500^2}{100} \cdot \frac{1500}{500 \times 10^3} \\ &= 2.8 \times 10^4 \text{ m}. \end{aligned} \tag{34}$$

Because the size of our breast model is only 10 cm, which is much smaller than the shock distance, it is reasonable to ignore the nonlinear acoustic effect in the microwave-induced TAI system.

The two basic linear acoustic wave generation equations are [13]

$$\rho \frac{\partial}{\partial t}\mathbf{u}(\mathbf{r},t) = -\nabla p(\mathbf{r},t) \tag{35}$$

and

$$\nabla \cdot \mathbf{u}(\mathbf{r},t) = -\frac{1}{\rho c^2}\frac{\partial}{\partial t}p(\mathbf{r},t) + \alpha p(\mathbf{r},t) + \beta \frac{\partial}{\partial t}T(\mathbf{r},t) \tag{36}$$

where $\mathbf{u}(\mathbf{r},t)$ is the acoustic velocity vector, $p(\mathbf{r},t)$ is the acoustic pressure field, ρ is the mass density, α is the attenuation coefficient, β is the thermal expansion coefficient, and $T(\mathbf{r},t)$ is the temperature. The values for these acoustic properties for different breast tissues are listed in Table II [14], [46], [48]–[50]. The attenuation coefficient is calculated with $f = 0.15$ MHz. The values for the tumor are approximated using the values for muscle because we cannot find the values specific to the tumor.

Because the duration of the microwave pulse is much shorter than the thermal diffusion time, thermal diffusion can be neglected [13], and the thermal equation is

$$C_p \frac{\partial}{\partial t}T(\mathbf{r},t) = \text{SAR}(\mathbf{r},t) \tag{37}$$

where C_p is the specific heat. Substituting (37) into (36) gives

$$\nabla \cdot \mathbf{u}(\mathbf{r},t) = -\frac{1}{\rho c^2}\frac{\partial}{\partial t}p(\mathbf{r},t) + \alpha p(\mathbf{r},t) + \frac{\beta}{C_p}\text{SAR}(\mathbf{r},t). \tag{38}$$

FDTD is used again to compute the thermal acoustic wave based on (35) and (38). More details about FDTD for acoustic simulations can be found in [34], [35], and [51]–[57].

The breast model for the acoustic simulation is constructed similarly to the model for electromagnetic simulation. The velocities of the normal fatty breast tissue are also assumed random with a variation of ±5% around average values, as shown in Fig. 6(b). An acoustic sensor array with 35 elements deployed uniformly around the breast model is used to record the thermal acoustic signals. The distance between neighboring acoustic sensors is 4 mm. The grid cell size used by the acoustic FDTD is 0.1 × 0.1 mm and the computational region is terminated by PML absorbing boundary conditions [55]–[57]. Note that the size of the FDTD cell for acoustic simulation is much finer than that of the FDTD cell for electromagnetic simulation because the wavelength of an acoustic wave is much smaller than that of a microwave. The SAR distribution data is interpolated to achieve the designed grid resolution for the acoustic breast model.

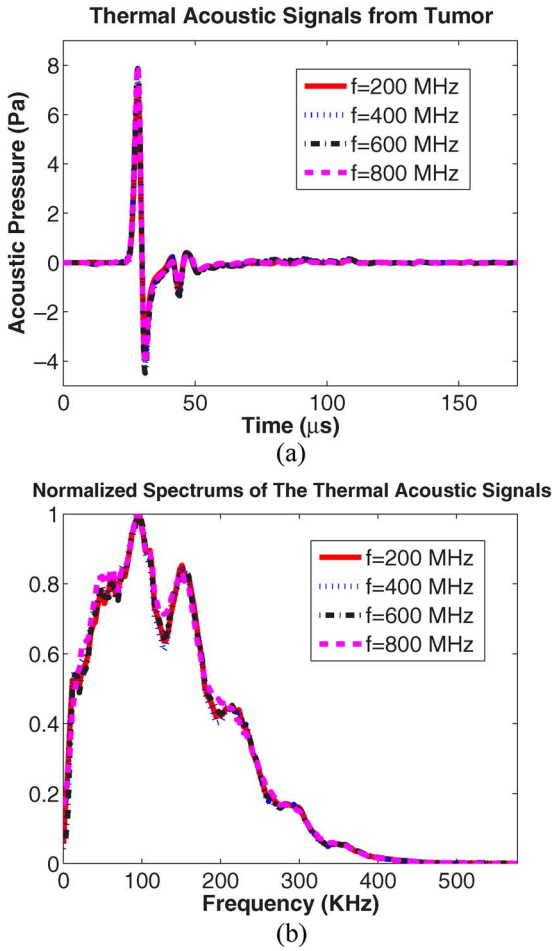

Fig. 8. Thermal acoustic signals at different stimulating frequencies $f = 200$, 400, 600, and 800 MHz. (a) Thermal acoustic responses from tumor only and (b) the normalized spectrums of the signals in (a).

V. NUMERICAL EXAMPLES

At the beginning of this section, the typical microwave-induced thermal acoustic responses from the tumor are plotted in Fig. 8(a) for stimulating frequencies of $f = 200$, 400, 600, and 800 MHz. The signals are simulated based on the aforementioned 2-D breast model. To obtain the signals, we perform the simulation twice at each stimulating frequency, with and

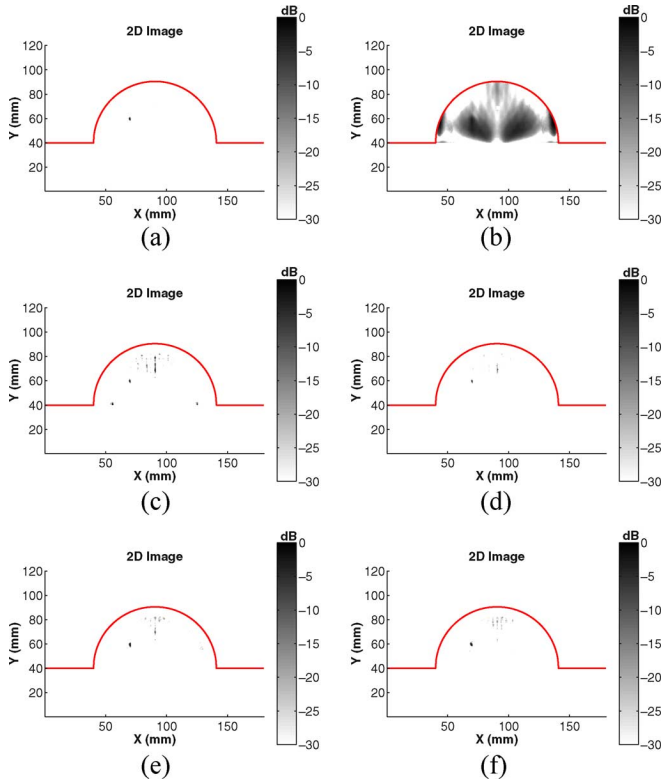

Fig. 9. Imaging results for the case of a single 1 mm-diameter tumor. (a) MART, (b) DAS, (c) SART at stimulating frequency $f = 200$ MHz, (d) SART at stimulating frequency $f = 400$ MHz, (e) SART at stimulating frequency $f = 600$ MHz, and (f) SART at stimulating frequency $f = 800$ MHz.

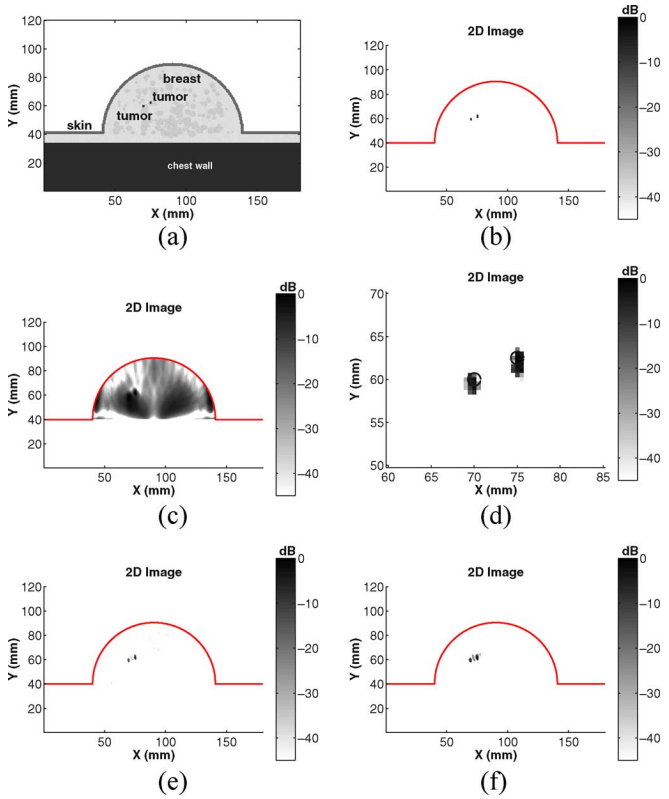

Fig. 10. Imaging results for the two 1.5-mm-diameter tumors case. (a) Breast model, (b) MART, (c) DAS, (d) zoom in of (b), (e) SART at stimulating frequency $f = 300$ MHz, and (f) SART at stimulating frequency $f = 700$ MHz.

without the tumor, and record the acoustic signals in an acoustic sensor. The difference of the two received signals is referred to as the thermal acoustic response only from the tumor at the stimulating frequency. It can be seen that the thermal acoustic responses from the tumor at different stimulating frequencies are similar to one another. The figure also shows that the thermal acoustic signals are wideband bipolar pulses, with a large positive peak and a large negative peak. Fig. 8(b) shows the normalized spectra of the acoustic signals corresponding to the excitations in Fig. 8(a). It is seen that the frequency range of the acoustic signals is about from 1 to 400 KHz. The dominant band (3-dB band) of the signals ranges from 10 to 180 KHz, and the corresponding acoustic wavelength ranges from 150 to 8 mm in the breast tissues.

Several numerical examples are used in this section to demonstrate the effectiveness of MART. The thermal acoustic signals are simulated based on the 2-D breast model with tumor only. For comparison purposes, the DAS method is applied to the same data set also. We also present the imaging results for the single-frequency microwave-induced TAI at different stimulating frequencies. The corresponding image reconstruction method is referred to as the single-frequency adaptive and robust technique (SART), which is similar with MART but without Stage II of MART. In SART, the RCB is used to estimate the thermal acoustic waveform at a certain stimulating frequency just like in Stage I of MART. Then the peak search method used in MART Stage III is applied to the estimated waveform to determine the image intensity.

In the first example, a 1-mm-diameter tumor is embedded in the breast model at the location ($x = 70$ mm, $y = 60$ mm). This is the challenging case of early breast cancer detection because of the small tumor size. Fig. 9(a) and (b) shows the imaging results for MART and DAS, respectively. The tumor is shown clearly in the MART image [Fig. 9(a)], and the size and location of the tumor is accurate. Because of the high sidelobe, poor resolution, and poor interference rejection capability of the DAS method, the tumor is essentially missed by DAS as shown in Fig. 9(b). Fig. 9(c)–(f) shows the imaging results for SART at the stimulating frequencies $f = 200$, 400, 600, and 800 MHz, respectively. The figures show that SART can determine the tumor correctly, but some clutter shows up in the SART images. Note that the clutter shows up at different locations with different stimulating frequencies. By comparing the images for MART and SART, it can be seen that the clutter are effectively suppressed by MART when multiple stimulating frequencies are used.

In the second numerical example, two small 1.5-mm-diameter tumors are set inside the breast model as shown in Fig. 10(a). Their locations are at ($x = 70$ mm, $y = 60$ mm) and ($x = 75$ mm, $y = 62.5$ mm). The distance between the two tumors is 4 mm. The imaging results using MART and DAS are shown in Fig. 10(b) and (c), respectively. The two tumors are seen clearly in the MART image. To show them clearly we zoom in onto the tumor locations in Fig. 10(d), where the two black circles mark the actual sizes and locations of the two tumors. It is shown that MART can be used to determine the locations and sizes of the two tumors accurately. The DAS

image contains much clutter. The two tumors cannot be separated clearly in the DAS image because of the poor resolution of DAS. Fig. 10(e) and (f) shows the imaging results of SART at stimulation frequencies $f = 300$ and 700 MHz, respectively. The tumors can be seen in both of the SART images, but clutter shows up between the two tumors in Fig. 10(e) and (f), and the sizes of the two tumors in Fig. 10(f) are larger than their true sizes.

VI. Conclusion

An investigation of using a multifrequency microwave-induced TAI system for early breast cancer detection has been reported in this paper. The frequency band for this system has been given based on the cutoff frequency of the human breast. A simplified semicircular dielectric waveguide mode was used to calculate the cutoff frequency in this paper. By studying the microwave energy absorption properties of breast tissue and tumor, we have shown that the multifrequency microwave-induced TAI can offer higher SNR, higher imaging contrast, and more effective clutter suppression capability than the traditional single-frequency microwave-induced TAI. A MART has been presented for image formation. This data-adaptive algorithm can achieve better resolution and better interference rejection capability than its data-independent counterparts, such as DAS. The feasibility of this multifrequency microwave-induced TAI system as well as the performance of the proposed image reconstruction algorithm for early breast cancer detection have been demonstrated by using 2-D numerical electromagnetic and acoustic breast models. The absorbed microwave energy and the thermal acoustic field in the breast models have been simulated using the FDTD method. Numerical examples have been used to demonstrate the excellent performance of this multifrequency technique. More advanced models are being developed to further investigate and validate the preferential imaging capability of the technique for early breast cancer detection.

References

[1] E. C. Fear, P. M. Meaney, and M. A. Stuchly, "Microwaves for breast cancer detection," *IEEE Potentials*, vol. 22, no. 1, pp. 12–18, Feb./Mar. 2003.

[2] P. M. Meaney, M. W. Fanning, D. Li, S. P. Poplack, and K. D. Paulsen, "A clinical prototype for active microwave imaging of the breast," *IEEE Trans. Microw. Theory Tech.*, vol. 48, no. 11, pp. 1841–1853, Nov. 2000.

[3] E. J. Bond, X. Li, S. C. Hagness, and B. D. Van Veen, "Microwave imaging via space-time beamforming for early detection of breast cancer," *IEEE Trans. Antennas Propagat.*, vol. 51, no. 8, pp. 1690–1705, Aug. 2003.

[4] B. Guo, Y. Wang, J. Li, P. Stoica, and R. Wu, "Microwave imaging via adaptive beamforming methods for breast cancer detection," *J. Electromagn. Waves Appl.*, vol. 20, no. 1, pp. 53–63, Jan. 2006.

[5] Y. Xie, B. Guo, L. Xu, J. Li, and P. Stoica, "Multi-static adaptive microwave imaging for early breast cancer detection," *IEEE Trans. Biomed. Eng.*, vol. 53, no. 8, pp. 1647–1657, Aug. 2006.

[6] D. Li, P. M. Meaney, and K. D. Paulsen, "Conformal microwave imaging for breast cancer detection," *IEEE Trans. Microw. Theory Tech.*, vol. 51, no. 4, pp. 1179–1186, Apr. 2003.

[7] Q. F. Fang, P. M. Meaney, S. D. Geimer, A. V. Streltsov, and K. D. Paulsen, "Microwave image reconstruction from 3-D fields coupled to 2-D parameter estimation," *IEEE Trans. Med. Imag.*, vol. 23, no. 4, pp. 475–484, Apr. 2004.

[8] Q. H. Liu, Z. Q. Zhang, T. T. Wang, J. A. Bryan, G. A. Ybarra, L. W. Nolte, and W. T. Joines, "Active microwave imaging I—2-D forward and inverse scattering methods," *IEEE Trans. Microw. Theory Tech.*, vol. 50, no. 1, pp. 123–133, Jan. 2002.

[9] Z. Q. Zhang, Q. H. Liu, C. Xiao, E. Ward, G. Ybarra, and W. T. Joines, "Microwave breast imaging: 3-D forward scattering simulation," *IEEE Trans. Biomed. Eng.*, vol. 50, no. 10, pp. 1180–1189, Oct. 2003.

[10] R. K. Mishra, A. Swarup, and J. M. Thomas, "Dielectric properties of normal and malignant human breast tissues at radiowave and microwave frequencies," *Ind. J. Biochem. Biophys.*, vol. 21, pp. 76–79, Feb. 1984.

[11] A. J. Surowiec, S. S. Stuchly, J. R. Barr, and A. Swarup, "Dielectric properties of breast carcinoma and the surrounding tissues," *IEEE Trans. Biomed. Eng.*, vol. 35, no. 4, pp. 257–263, Apr. 1988.

[12] W. T. Joines, Y. Zhang, C. X. Li, and R. L. Jirtel, "The measured electrical properties of normal and malignant human tissues from 50 to 900 MHz," *Med. Phys.*, vol. 21, no. 4, pp. 547–550, Apr. 1994.

[13] M. Xu and L. V. Wang, "Time-domain reconstruction for thermoacoustic tomography in a speherical geometry," *IEEE Trans. Med. Imag.*, vol. 21, no. 7, pp. 814–822, Jul. 2002.

[14] T. Szabo, *Diagnostic Ultrasound Imaging: Inside Out*. Burlington, MA: Elsevier, 2004.

[15] F. W. Kremkau, *Diagnostic Ultrasound: Principles and Instruments*. Philadelphia, PA: Saunders, 1993.

[16] E. Steen and B. Olstad, "Volume rendering of 3-D medical ultrasound data using direct feature mapping," *IEEE Trans. Med. Imag.*, vol. 13, no. 6, pp. 517–525, Jun. 1994.

[17] W. Joines, R. Jirtle, M. Rafal, and D. Schaeffer, "Microwave power absorption diffrences between normal and malignant tissue," *Int. J. Radiat. Oncol. Biol. Phys.*, vol. 6, no. 6, pp. 681–687, 1980.

[18] Y. Xu and L. H. Wang, "Effects of acoustic heterogeneity in breast thermoacoustic tomography," *IEEE Trans. Ultrason. Ferroelect. Freq. Control*, vol. 50, no. 9, pp. 1134–1146, Sep. 2003.

[19] M. Xu, Y. Xu, and L. V. Wang, "Time-domain reconstruction algorithms and numerical simulations for thermoacoustic tomography in various geometries," *IEEE Trans. Biomed. Eng.*, vol. 50, no. 9, pp. 1086–1099, Sep. 2003.

[20] Y. Xu, P. Kuchment, and L. H. Wang, "Limited-view thermoacoustic tomography and reconstruction by truncated conjugate gradient," *Med. Phys.*, vol. 31, pp. 724–733, Apr. 2004.

[21] R. A. Kruger, K. K. Kopecky, A. M. Aisen, D. R. Reinecke, G. A. Kruger, and W. L. Kiser, "Thermoacoustic CT with radio waves: A medical imaging paradigm," *Radiology*, vol. 211, pp. 275–278, Apr. 1999.

[22] R. A. Kruger, K. D. Miller, H. E. Reynolds, W. L. Kiser, D. R. Reinecke, and G. A. Kruger, "Breast cancer in vivo: Contrast enhancement with thermoacoustic CT at 434 MHz—Feasibility study," *Radiology*, vol. 216, pp. 279–283, Jul. 2000.

[23] R. A. Kruger, W. L. Kiser, K. D. Miller, H. E. Reynolds, D. R. Reinecke, and G. A. Kruger, "Thermoacoustic CT," in *Proc. IEEE MTT-S Int. Microwave Symp. Dig.*, Jun. 2000, vol. 2, pp. 11–16.

[24] Y. Xu, D. Feng, and L. H. Wang, "Exact frequency-domain reconstruction for thermoacoustic tomography I: Planar geometry," *IEEE Trans. Med. Imag.*, vol. 21, no. 7, pp. 823–828, Jul. 2002.

[25] Y. Xu, M. Xu, and L. H. Wang, "Exact frequency-domain reconstruction for thermoacoustic tomography II: Cylindrical geometry," *IEEE Trans. Med. Imag.*, vol. 21, no. 7, pp. 829–833, Jul. 2002.

[26] J. Li, P. Stoica, and Z. Wang, "On robust capon beamforming and diagonal loading," *IEEE Trans. Signal Process.*, vol. 51, no. 7, pp. 1702–1715, Jul. 2003.

[27] J. Li and P. Stoica, Eds., *Robust Adaptive Beamforming*. New York: Wiley, 2005.

[28] Y. Xie, B. Guo, J. Li, and P. Stoica, "Novel multistatic adaptive microwave imaging methods for early breast cancer detection," *EURASIP J. Appl. Signal Process.*, vol. 2006, pp. 1–12, 2006.

[29] Y. Xie, B. Guo, J. Li, G. Ku, and L. V. Wang, "Adaptive and robutst techniques (ART) for thermoacoustic tomography," presented at the Proc. 40th Asilomar Conf. Signals, Systems and Computers, Pacific Grove, CA, Nov. 2006.

[30] A. Taflove and S. C. Hagness, *Computational Electrodynamics: The Finite-Difference Time-Domain Method*, 2nd ed. Boston, MA: Artech House, 2000.

[31] D. M. Sullivan, *Electromagnetic Simulation Using the FDTD Method*. New York: IEEE, 2000.

[32] P. Bernardi, M. Cavagnaro, S. Pisa, and E. Piuzzi, "Specific absorption rate and temperature elevation in a subject exposed in the far-field of radio-frequency sources operating in the 10–900-MHz range," *IEEE Trans. Biomed. Eng.*, vol. 50, no. 3, pp. 295–304, Mar. 2003.

[33] P. Bernardi, M. Cavagnaro, S. Pisa, and E. Piuzzi, "SAR distribution and temperature increase in an anatomical model of the human eye exposed to the field radiated by the user antenna in a wireless LAN," *IEEE Trans. Microw. Theory Tech.*, vol. 46, no. 12, pp. 2074–2082, Dec. 1998.

[34] J. G. Maloney and K. E. Cummings, "Adaptation of FDTD techniques to acoustic modeling," in *Proc. 11th Annu. Rev. Progress in Applied Computational Electromagnetics*, Monterey, CA, 1995, vol. 2, pp. 724–731.
[35] X. Yuan, D. Borup, J. Wiskin, M. Berggren, and S. A. Johnson, "Simulation of acoustic wave propagation in dispersive media with relaxation losses by using FDTD method with PML absorbing boundary condition," *IEEE Trans. Ultrason., Ferroelect., Freq. Control*, vol. 46, no. 1, pp. 14–23, Jan. 1999.
[36] C. A. Balanis, *Advanced Engineering Electromagnetics*. New York: Wiley, 1989.
[37] S. Yang, H. Kim, and H. J. Lee, "Circular-harmonic vector analysis of dielectric waveguide with a cross-cut-circle cross section," *Appl. Opt.*, vol. 34, pp. 7705–7713, Nov. 1995.
[38] S. Gabriel, R. W. Lau, and C. Gabriel, "The dielectric properties of biological tissues: III. Parametric models for the dielectric spectrum of tissues," *Phys. Med. Biol.*, vol. 41, pp. 2271–2293, Nov. 1996.
[39] C. Gabriel and S. Gabriel, "Compilation of the dielectric properties of body tissues at rf and microwave frequencies," [Online]. Available: http://www.brooks.af.mil/AFRL/HED/hedr/reports/dielectric/home.html
[40] "Dielectric properties of body tissues," [Online]. Available: http://niremf.ifac.cnr.it/tissprop/
[41] X. Li and S. C. Hagness, "A confocal microwave imaging algorithm for breast cancer detection," *IEEE Microw. Wireless Compon. Lett.*, vol. 11, no. 3, pp. 130–132, Mar. 2001.
[42] P. Stoica and R. L. Moses, *Spectral Analysis of Signals*. Upper Saddle River, NJ: Prentice-Hall, 2005.
[43] C. G. A. Hoelen and F. F. M. de Mul, "Image reconstruction for photoacoustic scanning of tissue structures," *Appl. Opt.*, vol. 39, pp. 5872–5883, Nov. 2000.
[44] S. D. Gedney, "An anisotropic perfectly matched layer-absorbing medium for the truncation of FDTD lattices," *IEEE Trans. Antennas Propagat.*, vol. 44, no. 12, pp. 1630–1639, Dec. 1996.
[45] Z. S. Sacks, D. M. Kingsland, R. Lee, and J. F. Lee, "A perfectly matched anisotropic absorber for use as an absorbing boundary condition," *IEEE Trans. Antennas Propagat.*, vol. 43, no. 12, pp. 1460–1463, Dec. 1995.
[46] M. Xu and L. H. Wang, "Pulsed-microwave-induced thermoacoustic tomography: Filtered backprojection in a circular measurement configuration," *Med. Phys.*, vol. 29, no. 8, pp. 1661–1669, Aug. 2002.
[47] M. F. Hamilton and D. T. Blackstock, *Nonlinear Acoustics*. San Diego, CA: Acadmic, 1997.
[48] F. A. Duck, *Physical Properties of Tissue*. London, U.K.: Academic, 1990.
[49] M. L. Palmeri and K. R. Nightingale, "On the thermal effects associated with radiation force imaging of soft tissue," *IEEE Trans. Ultrason., Ferroelect., Freq. Control*, vol. 51, no. 5, pp. 551–565, May 2004.
[50] M. Converse, E. J. Bond, S. C. Hagness, and B. D. Van Veen, "Ultra-wide-band microwave space-time beamforming for hyperthermia treatment of breast cancer: A computational feasibility study," *IEEE Trans. Microw. Theory Tech.*, vol. 52, no. 8, pp. 1876–1889, Aug. 2004.
[51] C. K. W. Tam and J. C. Webb, "Dispersion-relation-preserving finite-difference schemes for computational acoustics," *J. Comput. Phys.*, vol. 107, no. 8, pp. 262–281, Aug. 1993.
[52] S. V. Tsynkov, "Numerical solution of problems on unbounded domains. A review," *Appl. Numer. Math.*, vol. 27, pp. 465–532, Aug. 1998.
[53] T. Colonius, S. K. Lele, and P. Moin, "Boundary-conditions for direct computation of aerodynamic sound generation," *AIAA J.*, vol. 31, pp. 1574–1582, Sep. 1993.
[54] C. W. Rowley and T. Colonius, "Discretely nonreflecting boundary conditions for linear hyperbolic systems," *J. Comput. Phys.*, vol. 157, pp. 500–538, Jan. 2000.
[55] Q. H. Liu and J. Tao, "The perfectly matched layer for acoustic waves in absorptive media," *J. Acoust. Soc. Amer.*, vol. 102, pp. 2072–2082, October 1997.
[56] X. Yuan, D. Borup, J. W. Wiskin, M. Berggren, R. Eidens, and S. A. Johnson, "Formulation and validation of Berenger's PML absorbing boundary for the FDTD simulation of acoustic scattering," *IEEE Trans. Ultrason., Ferroelect., Freq. Control*, vol. 44, no. 7, pp. 816–822, Jul. 1997.
[57] T. K. Katsibas and C. S. Antonopoulos, "A general form of perfectly matched layers for three-dimensional problems of acoustic scattering in lossless and lossy fluid media," *IEEE Trans. Ultrason., Ferroelect., Freq. Control*, vol. 51, no. 8, pp. 964–972, Aug. 2004.

Bin Guo (S'06–M'07) received the B.E. and M.Sc. degrees in electrical engineering from Xian Jiaotong University, Xian, China, in 1997 and 2000, respectively. He is currently pursuing the Ph.D. degree in electrical engineering in the Department of Electrical and Computer Engineering, University of Florida, Gainesville.

From April 2002 to July 2003, he was an Associate Research Scientist with the Temasek Laboratories, National University of Singapore, Singapore. Since August 2003, he has been a Research Assistant with the Department of Electrical and Computer Engineering, University of Florida. His current research interests include biomedical applications of signal processing, microwave imaging, and computational electromagnetics.

Jian Li (S'88–M'90–SM'97–F'05) received the M.Sc. and Ph.D. degrees in electrical engineering from The Ohio State University, Columbus, in 1987 and 1991, respectively.

From July 1991 to June 1993, she was an Assistant Professor with the Department of Electrical Engineering, University of Kentucky, Lexington. Since August 1993, she has been with the Department of Electrical and Computer Engineering, University of Florida, Gainesville, where she is currently a Professor. Her current research interests include spectral estimation, statistical and array signal processing, and their applications.

Dr. Li is a fellow of Institution of Electrical Engineers (IEE). She received the 1994 National Science Foundation Young Investigator Award and the 1996 Office of Naval Research Young Investigator Award. She has been a member of the Editorial Board of Signal Processing, a publication of the European Association for Signal Processing (EURASIP) since 2005. She is presently a member of two of the IEEE Signal Processing Society technical committees: the Signal Processing Theory and Methods (SPTM) Technical Committee and the Sensor Array and Multichannel (SAM) Technical Committee.

Henry Zmuda (M'75) received the B.E. degree from the Stevens Institute of Technology, Hoboken, NJ, in 1979, and the M.S. and Ph.D. degrees from Cornell University, Ithaca, NY, in 1982 and 1984, respectively, all in electrical engineering.

From 1984 to 1995, he was a member of the faculty at Stevens Institute of Technology. In 1995, he joined the Electrical Engineering Faculty, University of Florida. His research interests are primarily in the area of microwave photonics and applied electromagnetics.

Mark Sheplak received the B.S. degree in 1989, the M.S. degree in 1992, and the Ph.D. degree in 1995 in mechanical engineering from Syracuse University, Syracuse, NY.

He is an Associate Professor in the Department of Aerospace and Mechanical Engineering and an Affiliate Associate Professor of electrical and computer engineering at the University of Florida (UF). Prior to joining UF in 1998, he was a Postdoctoral Associate at the Massachusetts Institute of Technology's Microsystems Technology Laboratories, Cambridge, from 1995 to 1998. During his Ph.D. studies, he was a GSRP Fellow at the NASA-Langley Research Center, Hampton, VA, from 1992 to 1995. His current research focuses on the design, fabrication, and characterization of high-performance, instrumentation-grade, MEMS-based sensors and actuators that enable the measurement, modeling, and control of various physical properties.

USER PARAMETER FREE APPROACHES TO MULTISTATIC ADAPTIVE ULTRASOUND IMAGING

Lin Du† Jian Li† Petre Stoica‡
†Dept. of Electrical and Computer Engineering, University of Florida, Gainesville, FL 32611-6130, USA.
‡Dept. of Information Technology, Uppsala University, SE-75105 Uppsala, Sweden.

ABSTRACT

Delay-and-sum (DAS) beamforming is the standard technique for ultrasound imaging applications. Due to its data independent property, DAS may suffer from poorer resolution and worse interference suppression capability than the adaptive standard Capon beamformer (SCB). However, the performance of SCB is sensitive to the errors in the sample covariance matrix and the signal steering vector. Therefore, robust adaptive beamforming techniques are desirable. In this paper, we consider ultrasound imaging via applying a user parameter free robust adaptive beamformer, which uses a shrinkage-based general linear combination (GLC) algorithm to obtain an enhanced estimate of the array covariance matrix. We present several multistatic adaptive ultrasound imaging (MAUI) approaches based on GLC to achieve high resolution and good interference suppression capability. The performance of the proposed MAUI approaches is demonstrated via an experimental example.

***Index Terms*— Adaptive beamforming, Ultrasound imaging**

I. INTRODUCTION

Delay-and-sum (DAS) beamforming is the standard technique for ultrasound imaging applications. Theoretically this data independent approach has lower resolution and worse interference suppression capability than an adaptive beamformer, e.g., the standard Capon beamformer (SCB) [1]. However, in practice, there is a clear performance degradation for SCB when the covariance matrix is inaccurately estimated due to limited data samples and when the knowledge of the steering vector is imprecise due to look direction errors or imperfect array calibration. Therefore, adaptive beamforming approaches that are robust to the aforementioned problems are desired.

Most of the early approaches to robust adaptive beamforming are ad-hoc techniques, e.g., the traditional diagonal loading algorithm [2], for which there is no clear way to choose the diagonal loading level. The diagonal loading algorithm has been previously applied to ultrasound imaging [3], where the diagonal loading level was set to be proportional to the received power. The robust Capon beamformer (RCB) presented in [4], on the other hand, can precisely calculate the diagonal loading level based on the uncertainty set of the steering vector. RCB was applied to ultrasound imaging in [5] and the results showed that RCB can provide much better imaging quality than DAS. However, we still need to specify the uncertainty set parameter for RCB, which may be hard to do in practice. To achieve user parameter free robust adaptive beamforming, we have recently devised several beamformers in [6] based on the shrinkage method, which can compute the diagonal loading level automatically without specifying any user parameters. Among these beamformers, the general linear combination (GLC) algorithm performs well, especially when the number of snapshots is small.

In this paper, we present several user parameter free approaches based on GLC for multistatic adaptive ultrasound imaging (MAUI), which form images of the backscattered energy for each focal point within the region of interest. All the MAUI approaches are two-stage imaging algorithms and GLC is employed in each stage. A similar idea can be applied to microwave imaging to replace the user parameter dependent RCB in each stage [7]. The complete multistatic data set for a given focal point can be represented by the data cube shown in Fig. 1. In one of the MAUI methods, which we refer to as MAUI-1, GLC is used in Stage I to obtain a set of backscattered signal estimates at each time instant. Based on these estimates, a scalar waveform is recovered via GLC in Stage II, which is then used to compute the backscattered energy. An alternative way of signal processing in Stage I is to compute a set of backscattered waveforms for each transmitter, which is referred to as MAUI-2. In addition, we also consider a combined method MAUI-C, which uses the signal estimates from both MAUI-1 and MAUI-2 in Stage I for the computation of backscattered energy. An experimental example will be presented to illustrate the performance of the MAUI methods.

Notation: The superscript $(\cdot)^*$ denotes the conjugate transpose, $(\cdot)^T$ denotes the transpose, $\lfloor x \rfloor$ denotes rounding to the greatest integer less than x, $E(\cdot)$ is the expectation operator, $\mathrm{tr}(\cdot)$ is the trace operator, and $\|\cdot\|$ denotes the Frobenius norm for a matrix or the Euclidean norm for a vector. Finally $\mathbf{R} \geq 0$ means that $\mathbf{R}$ is positive semi-definite.

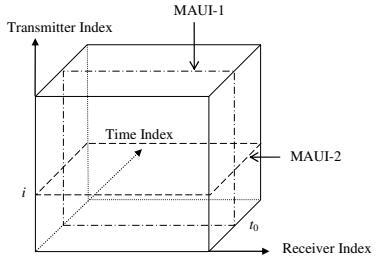

Fig. 1. The multistatic data cube. MAUI-1 processes the data set for a given time instant t_0, while MAUI-2 processes the data set for a given transmitter index i.

II. PROBLEM FORMULATION

Consider an active array of M transducers using the multistatic (also called MIMO (multi-input multi-output) [8]) data

The work was supported in part by the U.S. Army Medical Command under Grant No. W81XWH-06-1-0389, by the National Science Foundation under Grant No. CCF-0634786 and ECCS-0729727 and by the Swedish Research Council (VR).

Authorized licensed use limited to: University of Florida. Downloaded on January 28, 2010 at 17:02 from IEEE Xplore. Restrictions apply.

acquisition scheme. Each transducer takes turns to transmit the same pulse while all of the transducers record the backscattered signals. As a result, the received data set $\{\mathbf{P}_{i,j}(t), \quad i,j = 1,\cdots M; \quad t = 0,\cdots,T-1\}$ comprises the A-scan data for all possible transmitter and receiver pairs of the array, where $\mathbf{P}_{i,j}(t)$ is the data sequence of the backscattered echo at the j^{th} transducer due to transmitting a pulse from the i^{th} transducer, and T is the number of data samples for the A-scan sequence.

To extend GLC to the wide-band ultrasound imaging application, we align the received signals from the data set $\{\mathbf{P}_{i,j}(t)\}$ to each focal point by inserting appropriate time delays. Let $\mathbf{r}_i$ and $\mathbf{r}_j$ denote the locations of the i^{th} transmitter and j^{th} receiver, respectively, and let $\mathbf{r}_f$ denote the location of a focal point in the imaging region of interest. The time delay due to the ultrasonic wave propagation from the i^{th} transmitter to the focal point $\mathbf{r}_f$ and then back to the j^{th} receiver is approximated as

$$\tau_{i,j}(\mathbf{r}_f) = \frac{1}{\Delta t}\left\lfloor \frac{\|\mathbf{r}_i - \mathbf{r}_f\|}{c} + \frac{\|\mathbf{r}_j - \mathbf{r}_f\|}{c} \right\rfloor, \tag{1}$$

where c is the sound propagation speed in the medium under interrogation, and Δt denotes the sampling interval. Then, the time shifted signal for a given focal point of interest $\mathbf{r}_f$ can be represented as

$$\begin{aligned} &y_{i,j}(\mathbf{r}_f, t) = \mathbf{P}_{i,j}(t + \tau_{i,j}(\mathbf{r}_f)), \\ &i,j = 1,\cdots M; \quad t = 0,\cdots,N-1, \end{aligned} \tag{2}$$

where N is determined by the duration of the transmitted pulse and the sampling interval Δt.

The problem of interest here is to form an ultrasound image on a grid of points in the imaging region. The image is formed from the received data set $\{\mathbf{P}_{i,j}(t)\}$, or more precisely, $\{y_{i,j}(\mathbf{r}_f, t)\}$, for each focal point of interest.

III. MAUI

The two-stage MAUI algorithms use a GLC-based robust adaptive beamforming algorithm in each stage. We first review the GLC approach and then we show how to apply GLC to the data set $\{y_{i,j}(\mathbf{r}_f, t)\}$ in Stages I and II of the proposed MAUI approaches.

A. *GLC*

In the GLC approach, we replace the sample covariance matrix in SCB by an enhanced estimate obtained via a shrinkage-based method. The enhanced covariance matrix estimate $\tilde{\mathbf{R}}$ is obtained by linearly combining the sample covariance matrix $\hat{\mathbf{R}}$ and a shrinkage target (we use the identity matrix $\mathbf{I}$ here for lack of a better choice) in an optimal mean-squared error (MSE) sense:

$$\tilde{\mathbf{R}} = \alpha\mathbf{I} + \beta\hat{\mathbf{R}}, \tag{3}$$

where $\hat{\mathbf{R}} = \frac{1}{K}\sum_{k=1}^{K}\mathbf{y}(k)\mathbf{y}^*(k)$, with the $L \times 1$ vector $\mathbf{y}(k)$ denoting the kth snapshot and K representing the total number of snapshots. The shrinkage parameters α and β in (3) are estimated by minimizing the MSE of $\tilde{\mathbf{R}}$ with respect to α and β, where

$$\begin{aligned} &\mathrm{MSE}(\tilde{\mathbf{R}}) = E\{\|\tilde{\mathbf{R}} - \mathbf{R}\|^2\} \\ &= \|\alpha\mathbf{I} - (1-\beta)\mathbf{R}\|^2 + \beta^2 E\{\|\hat{\mathbf{R}} - \mathbf{R}\|^2\} \\ &= \alpha^2 L - 2\alpha(1-\beta)\,\mathrm{tr}(\mathbf{R}) \\ &+(1-\beta)^2\|\mathbf{R}\|^2 + \beta^2 E\{\|\hat{\mathbf{R}} - \mathbf{R}\|^2\}, \\ &\mathbf{R} = E\left[\mathbf{y}(k)\mathbf{y}^*(k)\right]. \end{aligned} \tag{4}$$

The optimal values for β and α can be readily obtained:

$$\beta_0 = \frac{\gamma}{\rho + \gamma}, \tag{5}$$

$$\alpha_0 = \nu(1-\beta_0) = \nu\frac{\rho}{\gamma+\rho}, \tag{6}$$

where $\rho = E\{\|\hat{\mathbf{R}} - \mathbf{R}\|^2\}$, $\nu = \frac{\mathrm{tr}(\mathbf{R})}{L}$, and $\gamma = \|\nu\mathbf{I} - \mathbf{R}\|^2$. Note that $\beta_0 \in [0,1]$ and $\alpha_0 \geq 0$.

To estimate α_0 and β_0 from the given data, we need an estimate of ρ, which can be calculated as (see [9] for details):

$$\hat{\rho} = \frac{1}{K^2}\sum_{k=1}^{K}\|\mathbf{y}(k)\|^4 - \frac{1}{K}\|\hat{\mathbf{R}}\|^2. \tag{7}$$

Using (7) we can get estimates for β_0 and α_0 as

$$\hat{\beta}_0 = \frac{\hat{\gamma}}{\hat{\gamma} + \hat{\rho}}, \tag{8}$$

and

$$\hat{\alpha}_0 = \hat{\nu}(1 - \hat{\beta}_0), \tag{9}$$

where $\hat{\nu} = \frac{\mathrm{tr}(\hat{\mathbf{R}})}{L}$, and $\hat{\gamma} = \|\hat{\nu}\mathbf{I} - \hat{\mathbf{R}}\|^2$. Note that $\hat{\alpha}_0 \geq 0$ and $\hat{\beta}_0 \geq 0$, which guarantees that the enhanced covariance matrix estimate $\tilde{\mathbf{R}} \geq 0$.

Substituting (8)-(9) in (3) yields the enhanced covariance matrix estimate $\tilde{\mathbf{R}}$. Using $\tilde{\mathbf{R}}$ instead of $\hat{\mathbf{R}}$ in the SCB formulation, we obtain the beamformer weight vector for GLC as follows:

$$\hat{\mathbf{w}} = \frac{\tilde{\mathbf{R}}^{-1}\bar{\mathbf{a}}}{\bar{\mathbf{a}}^*\tilde{\mathbf{R}}^{-1}\bar{\mathbf{a}}}, \tag{10}$$

where $\bar{\mathbf{a}}$ denotes the assumed steering vector [10]. Note that GLC is a diagonal loading approach with the diagonal loading level $\hat{\alpha}_0/\hat{\beta}_0$ determined automatically from the observed data snapshots $\{\mathbf{y}(k)\}_{k=1}^{K}$.

B. *Stage I*

To apply the GLC-based robust adaptive beamformer to the data set $\{y_{i,j}(\mathbf{r}_f, t)\}$ in (2), we use two approximate signal models for $y_{i,j}(\mathbf{r}_f, t)$ by making different assumptions. Since we will concentrate on the focal point $\mathbf{r}_f$ in what follows, the dependence on $\mathbf{r}_f$ will be dropped for notational simplicity.

The MAUI-1 algorithm uses the following signal model:

$$\mathbf{y}_i(t) = \mathbf{a}(t)s_i(t) + \mathbf{e}_i(t), \tag{11}$$

where $\mathbf{y}_i(t) = [y_{i,1}(t),\cdots,y_{i,M}(t)]^T$ represents the aligned array data vector of the i^{th} transmitter, $s_i(t)$ denotes the signal of interest (SOI) that is proportional to the ultrasound reflectivity or scattering strength, which is assumed to depend on the transmitter i but not on the receiver j, $\mathbf{e}_i(t)$ denotes the residual term due to noise and interferences, and $\mathbf{a}(t)$ denotes the array steering vector that is assumed to be approximately equal to $\mathbf{1}_{M\times 1}$. Here, we assume that $\mathbf{a}(t)$ may vary with t, but is constant with respect to the transmitter index i.

Authorized licensed use limited to: University of Florida. Downloaded on January 28, 2010 at 17:02 from IEEE Xplore. Restrictions apply.

In Stage I, for a given time t_0, we form a pseudo-covariance matrix by considering the number of transmitters as the number of snapshots:

$$\hat{\mathbf{R}}(t_0) = \frac{1}{M}\mathbf{Y}(t_0)\mathbf{Y}^*(t_0),$$
$$\mathbf{Y}(t_0) = [\mathbf{y}_1(t_0)\cdots\mathbf{y}_M(t_0)]. \quad (12)$$

By using $\hat{\mathbf{R}}(t_0)$ as the sample covariance matrix we obtain an enhanced covariance matrix estimate $\tilde{\mathbf{R}}(t_0)$ as described in Section III.A, and then calculate the weight vector $\hat{\mathbf{w}}(t_0)$ for Stage I of MAUI-1 using (10) with $\bar{\mathbf{a}} = \mathbf{1}_{M\times 1}$ as:

$$\hat{\mathbf{w}}(t_0) = \frac{\tilde{\mathbf{R}}(t_0)^{-1}\bar{\mathbf{a}}}{\bar{\mathbf{a}}^*\tilde{\mathbf{R}}(t_0)^{-1}\bar{\mathbf{a}}}. \quad (13)$$

Once we got the weight vector, we can estimate $s_i(t_0)$ in (11) as:

$$\hat{s}_i(t_0) = \hat{\mathbf{w}}^*(t_0)\mathbf{y}_i(t_0). \quad (14)$$

Define a vector $\hat{\mathbf{s}}(t_0) = [\hat{s}_1(t_0),\cdots,\hat{s}_M(t_0)]^T$ of the estimated signals for all transmitters. Repeating the above process from $t_0 = 0$ to $t_0 = N-1$, we build the matrix $\hat{\mathbf{S}}_1 = [\hat{\mathbf{s}}(0),\cdots,\hat{\mathbf{s}}(N-1)]$.

The MAUI-2 algorithm considers another signal model:

$$\mathbf{y}_i(t) = \mathbf{a}_i s_i(t) + \mathbf{e}_i(t), \quad (15)$$

where $\mathbf{a}_i$ denotes the array steering vector, which is also assumed to be approximately equal to $\mathbf{1}_{M\times 1}$. However, different from MAUI-1, here $\mathbf{a}_i$ is assumed to change with i, but be constant with respect to t.

For a given transmitter i, the covariance matrix in Stage I of MAUI-2 is formulated as:

$$\hat{\mathbf{R}}_i = \frac{1}{N}\mathbf{Y}_i\mathbf{Y}_i^*,$$
$$\mathbf{Y}_i = [\mathbf{y}_i(0)\cdots\mathbf{y}_i(N-1)]. \quad (16)$$

Using $\hat{\mathbf{R}}_i$ as the sample covariance matrix we get an enhanced estimate $\tilde{\mathbf{R}}_i$, and then compute a weight vector $\hat{\mathbf{w}}_i$ using (10). The time sample vector of the corresponding beamformer output can be written as

$$\hat{\mathbf{s}}_i = [\hat{\mathbf{w}}_i^*\mathbf{Y}_i]^T. \quad (17)$$

Repeating the above process for $i = 1,\cdots,M$ yields a set of waveforms $\hat{\mathbf{S}}_2 = [\hat{\mathbf{s}}_1,\cdots,\hat{\mathbf{s}}_M]^T$.

As we mentioned before, the errors in the sample covariance matrix and the steering vector cause performance degradations for any adaptive beamforming algorithms. GLC is designed to improve the covariance matrix estimate. MAUI-1 and MAUI-2 use different sample covariance matrices. Hence the improvements obtained by using GLC may be different. This fact motivates us to combine MAUI-1 and MAUI-2 to achieve a better performance. We refer to this combined method, where $\hat{\mathbf{S}}_1$ of MAUI-1 and $\hat{\mathbf{S}}_2$ of MAUI-2 are used simultaneously, as MAUI-C. We denote the combined signal matrix as $\hat{\mathbf{S}}_C = \begin{bmatrix}\hat{\mathbf{S}}_1^T & \hat{\mathbf{S}}_2^T\end{bmatrix}^T$.

Let the $M \times 1$ vectors $\{\hat{\mathbf{s}}_m(t)\}_{t=0,\cdots,N-1}$ denote the columns of $\hat{\mathbf{S}}_m$ for $m = 1,2$, and let the $2M \times 1$ vectors $\{\hat{\mathbf{s}}_C(t)\}_{t=0,\cdots,N-1}$ denote the columns of $\hat{\mathbf{S}}_C$. Note that both MAUI-1 and MAUI-2 obtain M signal waveform estimates at the end of Stage I, while MAUI-C obtains $2M$ signal waveform estimates. We will apply GLC to these estimates in Stage II to recover a scalar waveform and compute the signal energy at the focal point.

C. *Stage II*

In Stage II, the signal model for both MAUI-1 and MAUI-2 can be represented as:

$$\hat{\mathbf{s}}_m(t) = \mathbf{a}_m s(t) + \mathbf{e}_m(t), \quad t = 0,\cdots,N-1, \quad m = 1,2, \quad (18)$$

where the steering vector $\mathbf{a}_m$ is assumed to be $\mathbf{1}_{M\times 1}$, and $\mathbf{e}_m(t)$ represents the residual term. Similar to Stage I, the knowledge of $\mathbf{a}_m$ may be imprecise and the sample size N may be small. Hence the GLC-based robust adaptive beamformer is used again to estimate $s(t)$. Taking $\hat{\mathbf{R}}_m$ as the sample covariance matrix:

$$\hat{\mathbf{R}}_m = \frac{1}{N}\sum_{t=0}^{N-1}\hat{\mathbf{s}}_m(t)\hat{\mathbf{s}}_m^*(t), \quad m = 1,2, \quad (19)$$

and paralleling the development in Stage I, we obtain the weight vector $\hat{\mathbf{w}}_m$ using (10). Then, the output signal estimate is computed as:

$$\hat{s}(t) = \hat{\mathbf{w}}_m^*\hat{\mathbf{s}}_m(t), \quad m = 1,2. \quad (20)$$

Finally, the signal energy for a particular focal point $\mathbf{r}_f$ is computed as:

$$\mathcal{E}(\mathbf{r}_f) = \sum_{t=0}^{N-1}\hat{s}^2(t). \quad (21)$$

For Stage II of MAUI-C, the signal model can be written as:

$$\hat{\mathbf{s}}_C(t) = \mathbf{a}_C s(t) + \mathbf{e}_C(t), \quad t = 0,\cdots,N-1, \quad (22)$$

where the vector $\hat{\mathbf{s}}_C(t)$ is considered now to be a snapshot from a $2M$-element "array", and the steering vector $\mathbf{a}_C$ is assumed to be $\mathbf{1}_{2M\times 1}$. $\mathbf{e}_C(t)$ denotes the residual term. We obtain the weight vector $\hat{\mathbf{w}}_C$ for MAUI-C via (10) by using the following sample covariance matrix:

$$\hat{\mathbf{R}}_C = \frac{1}{N}\sum_{t=0}^{N-1}\hat{\mathbf{s}}_C(t)\hat{\mathbf{s}}_C^*(t). \quad (23)$$

The beamformer $\hat{\mathbf{w}}_C$ yields an estimate of the signal:

$$\hat{s}(t) = \hat{\mathbf{w}}_C^*\hat{\mathbf{s}}_C(t). \quad (24)$$

Then, the backscattered energy at the focal point $\mathbf{r}_f$ is computed via (21).

IV. EXPERIMENTAL EXAMPLE

In this section, we present some experimental results to demonstrate the performance of the three MAUI algorithms. The complete multistatic data set was obtained by Bioacoustics Research Laboratory of the University of Illinois at Urbana-Champaign. The scene of interest contains several wire targets arranged in a complicated pattern. The data was collected using a 64-element linear array. The transducer center frequency was 2.6 MHz, the sampling rate was 25 MHz, and the sound velocity was assumed to be 1450 m/s. For comparison, the multistatic DAS scheme is also applied to the same data set. The DAS scheme estimates the signal waveform $s(t)$ as

$$\hat{s}(t) = \hat{\mathbf{w}}_{\text{DAS}}^*\mathbf{Y}(t)\hat{\mathbf{w}}_{\text{DAS}}, \quad t = 0,\cdots,N-1, \quad (25)$$

where $\hat{\mathbf{w}}_{\text{DAS}} = \bar{\mathbf{a}}/M$ is the weight vector for DAS. The backscattered energy at $\mathbf{r}_f$ is then estimated via (21).

Authorized licensed use limited to: University of Florida. Downloaded on January 28, 2010 at 17:02 from IEEE Xplore. Restrictions apply.

Fig. 2 shows the ultrasound images for the wire data set under consideration. The images are displayed on a logarithmic scale with a 30 dB dynamic range. In Figs. 2 (a)-(d), we compare the images obtained via DAS and MAUI algorithms using only the central 32 elements of the array ($M = 32$). Since DAS simply sums all signals, the DAS image shown in Fig. 2 (a) has higher sidelobe level and poorer resolution than the MAUI images shown in Figs. 2 (b)-(d). Comparing Fig. 2 (b) and Fig. 2 (c), which correspond to MAUI-1 and MAUI-2 respectively, we note that MAUI-2 image has a lower background clutter level. However, MAUI-2 has poorer resolution: some wire targets are not discernable in the MAUI-2 image. On the other hand, the image obtained via MAUI-C has low sidelobe level similarly to MAUI-2 and high resolution similarly to MAUI-1. Moreover, all targets are clearly shown in the MAUI-C image. For comparison, we also include the DAS image obtained using the entire array ($M = 64$). Note that MAUI algorithms, especially MAUI-C, with 32 transducers can achieve similar imaging quality to DAS with a double sized array.

V. CONCLUSIONS

We have presented three user parameter free approaches to multistatic adaptive ultrasound imaging (MAUI). These two-stage MAUI approaches employ a GLC-based robust adaptive beamformer in each stage to achieve high resolution and good interference suppression capability, and also they are robust to small sample size problems and array steering vector errors. More importantly, GLC is a user parameter free approach as opposed to other existing robust adaptive beamforming algorithms, which makes it easy to use it in practice. The experimental results have demonstrated the effectiveness of the MAUI algorithms for ultrasound imaging. We have shown that the MAUI-C method, which combines MAUI-1 and MAUI-2, provides the best imaging quality.

REFERENCES

[1] J. Capon, "High resolution frequency-wavenumber spectrum analysis," *Proceedings of the IEEE*, vol. 57, pp. 1408–1418, August 1969.

[2] H. Cox, R. Zeskind, and M. Owen, "Robust adaptive beamforming," *Proceedings of IEEE*, vol. ASSP-35, pp. 1365–1375, October 1987.

[3] J. Synnevåg, A. Austeng, and S. Holm, "Adaptive beamforming applied to medical ultrasound imaging," *IEEE Transactions on Ultrasonics, Ferroelectrics, and Frequency Control*, vol. 54, no. 8, pp. 1606–1613, 2007.

[4] J. Li, P. Stoica, and Z. Wang, "On robust Capon beamforming and diagonal loading," *IEEE Transactions on Signal Processing*, vol. 51, pp. 1702–1715, July 2003.

[5] Z. Wang, J. Li, and R. Wu, "Time-delay and time-reversal based robust Capon beamformers for ultrasound imaging," *IEEE Transactions on Medical Imaging*, vol. 24, no. 10, pp. 1308–1322, 2005.

[6] J. Li, L. Du, and P. Stoica, "Fully automatic computation of diagonal loading levels for robust adaptive beamforming," submitted to *IEEE Transactions on Aerospace and Electronic Systems*, 2007.

[7] Y. Xie, B. Guo, J. Li, and P. Stoica, "Novel multistatic adaptive microwave imaging methods for early breast cancer detection," *EURASIP Journal on Applied Signal Processing*, vol. 2006, pp. 1–12, 2006.

[8] J. Li and P. Stoica, "MIMO radar with colocated antennas: Review of some recent work," *IEEE Signal Processing Magazine*, vol. 24, no. 5, pp. 106–114, 2007.

[9] P. Stoica, J. Li, X. Zhu, and J. R. Guerci, "On using a priori knowledge in space-time adaptive processing," to appear in *IEEE Transactions on Signal Processing*, 2007.

[10] P. Stoica and R. L. Moses, *Spectral Analysis of Signals*. Upper Saddle River, NJ: Prentice-Hall, 2005.

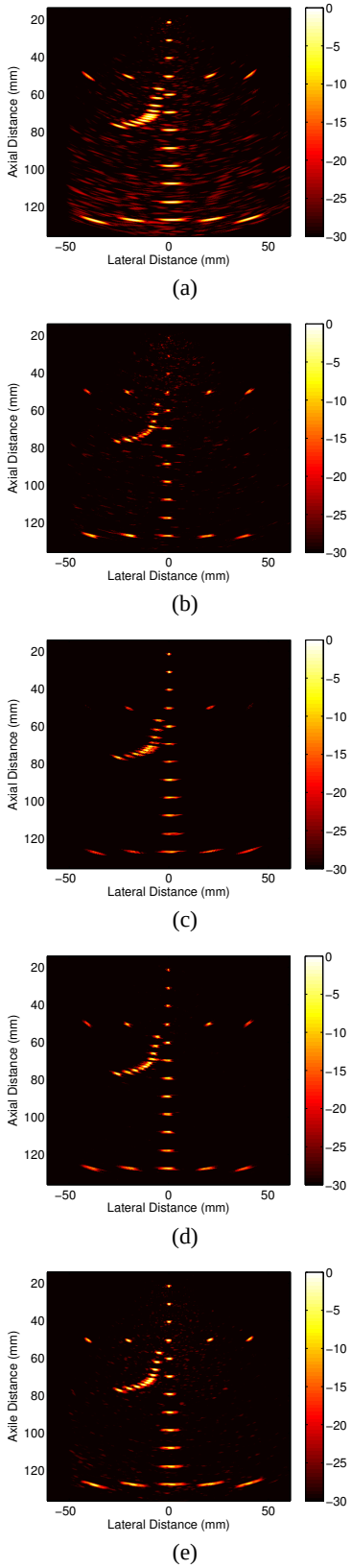

Fig. 2. Ultrasound images obtained via (a) DAS with $M = 32$, (b) MAUI-1 with $M = 32$, (c) MAUI-2 with $M = 32$, (d) MAUI-C with $M = 32$, and (e) DAS with $M = 64$.

Authorized licensed use limited to: University of Florida. Downloaded on January 28, 2010 at 17:02 from IEEE Xplore. Restrictions apply.